

Department of Physics and Astronomy  
University of Heidelberg

Master Thesis in Physics

submitted by

**Rossana Facen**

born in Cagliari, Italy

**2024**

**Study of charm quark thermalization  
in the quark-gluon plasma produced at RHIC**

This Master thesis has been carried out by Rossana Facen at the  
Physikalisches Institut Heidelberg  
under the supervision of  
Prof. Dr. Silvia Masciocchi

## Abstract

Heavy quarks, i.e. charm and bottom quarks, are unique probes to study the properties of the hot and dense QCD medium produced in heavy-ion collisions, the quark-gluon plasma (QGP). Due to their large masses, heavy quarks are produced at the initial stage of the collision almost exclusively via hard partonic scattering processes. As a result, heavy quarks experience the entire collision history: they propagate through the QCD medium and interact with its constituents, potentially leading to their thermalization within the QGP. While various evidences supporting the thermalization of charm quarks at the LHC have been collected in recent years, the thermalization process highly depends on the colliding system and energy. The present study focuses on the possible thermalization of charm quarks at RHIC in Au – Au collisions at a center-of-mass energy of  $\sqrt{s_{\text{NN}}} = 200$  GeV. The local thermalization of charm quarks is examined using a recently developed fluid-dynamic approach. The output of our analysis is fit to the available experimental data of the STAR collaboration. The heavy-quark spatial diffusion coefficient multiplied by the temperature  $D_s T$  is estimated using a Bayesian framework that employs an ensemble of neural networks as emulator and Markov chain Monte Carlo simulations.

# Zusammenfassung

Schweren Quarks, also Charme- und Bottom-Quarks, sind einzigartige Sonden zur Untersuchung der Eigenschaften des heißen und dichten QCD-Mediums, das bei Schwerionenkollisionen entsteht, dem Quark-Gluon-Plasma (QGP). Aufgrund ihrer großen Massen werden schwere Quarks fast ausschließlich durch harte partonische Streuprozesse erzeugt im Anfangsstadium der Kollision. Infolgedessen erleben schwere Quarks die gesamte Kollisionsgeschichte: sie propagieren durch das QCD-Medium und interagieren mit dessen Bestandteilen, was möglicherweise zu ihrer Thermalisierung innerhalb des QGP führt. Während in den letzten Jahren verschiedene Belege für die Thermalisierung von Charm-Quarks am LHC gesammelt wurden, hängt der Thermalisierungsprozess stark vom kollidierenden System und der Energie ab. Die vorliegende Arbeit konzentriert sich auf die mögliche Thermalisierung von Charm-Quarks am RHIC bei Au – Au-Kollisionen bei einer Schwerpunktsenergie von  $\sqrt{s_{NN}} = 200$  GeV. Die lokale Thermalisierung von Charm-Quarks wird mit einem kürzlich entwickelten fluid-dynamischen Ansatz untersucht. Die Ergebnisse unserer Analyse passen zu den verfügbaren experimentellen Daten der STAR-Kollaboration. Der räumliche Diffusionskoeffizient der schweren Quarks multipliziert mit der Temperatur  $D_s T$  wird mit Hilfe eines Bayesschen Systems geschätzt, das ein neuronales Netzwerk-Ensemble-Emulatormodell und Markov-Ketten Monte Carlo Simulationen verwendet.

# Contents

<b>1</b>	<b>Introduction</b>	<b>1</b>
1.1	The Standard Model of Particle Physics . . . . .	1
1.2	Quantum chromodynamics . . . . .	3
1.2.1	Asymptotic freedom . . . . .	5
1.2.2	Color confinement . . . . .	6
1.3	The quark-gluon plasma . . . . .	7
1.3.1	The QCD phase diagram . . . . .	8
1.3.2	Heavy-ion collisions . . . . .	9
1.4	Experimental observables of the QGP . . . . .	11
1.4.1	Anisotropic flow . . . . .	12
<b>2</b>	<b>Heavy-ion-collision modeling</b>	<b>14</b>
2.1	Initial state of heavy-ion collisions . . . . .	14
2.1.1	The Glauber model . . . . .	16
2.1.2	The T <sub>REN</sub> To model . . . . .	17
2.2	Hydrodynamic description of QGP . . . . .	19
2.2.1	Ideal fluid dynamics . . . . .	19
2.2.2	Viscous fluid dynamics . . . . .	21
2.2.3	FluiduM package . . . . .	23
2.2.4	Equation of State . . . . .	25
2.3	Hadronization and freeze-out . . . . .	26
2.3.1	The Cooper-Frye procedure . . . . .	26
2.3.2	Resonance decays . . . . .	29
<b>3</b>	<b>Heavy-quark dynamics</b>	<b>31</b>
3.1	Heavy quarks and transport models . . . . .	31
3.1.1	The Boltzmann equation . . . . .	31
3.1.2	The Fokker-Planck equation . . . . .	33
3.1.3	The spatial diffusion coefficient . . . . .	35
3.2	The hydrodynamic approach to heavy quarks . . . . .	37
3.2.1	Heavy-flavour elliptic flow . . . . .	37
3.2.2	Heavy-quark conserved current . . . . .	38
3.2.3	Relation between hydrodynamics and distribution function . . . . .	39
3.2.4	Heavy-quark transport coefficients . . . . .	41
<b>4</b>	<b>Heavy quarks at RHIC</b>	<b>43</b>
4.1	Motivation . . . . .	43

4.2	Initial condition modeling . . . . .	44
4.2.1	Initial temperature . . . . .	45
4.2.2	Heavy-quark density . . . . .	47
4.2.3	Binary nucleon-nucleon collisions . . . . .	48
4.2.4	Initial fugacity . . . . .	51
4.3	Applicability of the hydrodynamic approach . . . . .	52
4.3.1	Heavy quarks in Fluid $u$ M . . . . .	52
4.3.2	Bjorken Flow . . . . .	53
4.3.3	Charm relaxation time . . . . .	55
4.4	Charmed hadron spectra . . . . .	56
<b>5</b>	<b>Analysis framework</b>	<b>59</b>
5.1	The Bayesian inference . . . . .	59
5.1.1	Priors distribution . . . . .	59
5.1.2	Likelihood function . . . . .	60
5.2	Machine learning techniques . . . . .	61
5.2.1	Neural Networks . . . . .	62
5.2.2	Loss function . . . . .	63
5.2.3	Uncertainty quantification . . . . .	64
5.3	Markov-chain Monte Carlo . . . . .	65
5.4	Analysis implementation . . . . .	66
5.4.1	Parameters set . . . . .	66
5.4.2	Neural networks in the present analysis . . . . .	68
5.4.3	MCMC in the present analysis . . . . .	70
<b>6</b>	<b>Results and discussion</b>	<b>71</b>
6.1	Light hadrons . . . . .	71
6.1.1	Fluid $u$ M results . . . . .	71
6.1.2	Neural network validation . . . . .	72
6.1.3	MCMC procedure . . . . .	73
6.2	Charmed hadrons . . . . .	77
6.3	Global fit . . . . .	80
<b>7</b>	<b>Conclusions and outlook</b>	<b>85</b>
7.1	Outlook . . . . .	86

# 1 Introduction

## Units and conventions

Throughout this thesis, all the calculations will be expressed using the natural units system, which is widely used in particle physics. Here, the speed of light, the Planck's constant divided by  $2\pi$ , and the Boltzmann constant are set as unit-less constants equal to one:  $c = \hbar = k_B = 1$ . Therefore, energy, momentum, and mass quantities will be expressed in eV units, or its multiples.

Greek indexes will refer to four-vector components  $\mu = 0, 1, 2, 3$ , while Latin indexes will be used to indicate spatial coordinates  $i = 1, 2, 3$ . Moreover, Einstein summation convention will be adopted: according to this notation, when an index variable appears twice in a single term, this implies a summation of that term over all the values of the index:  $\sum_{\mu=0}^3 c_{\mu}x^{\mu} \equiv c_{\mu}x^{\mu} = c_0x^0 + c_1x^1 + c_2x^2 + c_3x^3$ .

## 1.1 The Standard Model of Particle Physics

The Standard Model of particle physics (SM) is a gauge theory that classifies all known elementary particles and describes three of the four fundamental interactions in the Universe: the electromagnetic, the weak, and the strong force.

The dynamics of SM's particles, as well as the interactions between them, are described by the Standard Model Lagrangian, which obeys  $U(1) \times SU(2) \times SU(3)$  symmetry.

Each symmetry of the SM is associated with a gauge field that mediates the corresponding force. The electromagnetic interaction, mediated by the photon, is for instance associated with the  $U(1)$  gauge symmetry. Similarly, the weak force is associated with  $SU(2)$  symmetry, and the strong force with  $SU(3)$ .

In the SM, the charges of particles determine the types of interactions they can participate in. If a particle is electrically charged, it can interact via electromagnetic force, while weak isospin and color charge are the charges associated with weak and strong force, respectively.

Within the SM, particles are classified according to their properties and interactions, as schematically depicted in Fig. 1.1.

The SM includes twelve spin-1/2 particles called *fermions*, which obey Fermi-Dirac statistics [1]. These particles are considered as the building blocks of matter, and all of them interact via weak interaction. Fermions are usually classified into six leptons and six quarks. Three of six leptons possess electric charge (electron, muon, and tau particles) and can interact via electromagnetic force. On the other hand, the corresponding three neutrinos are neutrally charged and carry only weak isospin charge.

The six quarks carry color charge, and can therefore interact via the strong interaction. These particles possess non-integer electric charges, which can be  $+2/3$  (up, charm, and top quark), or  $-1/3$  (down, strange, and bottom quark).

Depending on their mass, fermions can also be classified into three different generations: the lightest particles make up the first generation, while the heavier ones belong to the second and third generations. All stable matter in the Universe is made of particles belonging to the first generation; the particles of the second and third generations quickly decay into more stable ones.

In the SM fermions interact with each other by exchanging force-carrier particles, called *bosons*. There are twelve spin-1 gauge bosons, obeying Bose-Einstein statistics [2]. Bosons mediate the three forces of the SM: as mentioned before, the photon mediates the electromagnetic interaction, while three massive bosons ( $W^+$ ,  $W^-$ , and  $Z^0$ ) are responsible for the weak interaction, and eight gluons mediate the strong interaction.

Moreover, the SM offers a good description of the mechanism responsible for the generation of the masses of fermions and of massive gauge bosons. The gauge symmetry of the SM Lagrangian is preserved only if all particles of the SM are massless, in clear disagreement with experimental results. This problem is overcome by introducing a spin-0 neutral boson, known as the *Higgs boson* [3, 4]. The interaction between the Higgs boson and initially massless particles allows the latter to acquire mass, through a mechanism known as *symmetry breaking*. The discovery in 2012 of the Higgs boson at the Large Hadron Collider is regarded as one of the best achievements of the SM.

Even if the SM represents the best-known theory describing particle interactions, it is important to point out that the model is not able to account for several experimental observations, such as the neutrino's masses [5], and the presence of dark matter [6]. For this reason, further experimental and theoretical studies will be needed to shed light on these unsolved questions.



$SU(3)$ . It can be easily proven that the  $\lambda_a$  matrices do not commute: thus, since its generators do not commute,  $SU(3)$  represents a non-Abelian theory. Instead of working directly with Gell-Mann matrices, in particle physics it is usually preferable to use  $T_a$  matrices defined as,

$$T_a = \frac{1}{2}\lambda_a \quad a = 1, 2, \dots, 8. \quad (1.2)$$

Knowing the generators of  $SU(3)$  group, every general matrix  $U \in SU(3)$  can be represented as,

$$U = e^{ig_s\alpha(x)\cdot\mathbf{T}}, \quad (1.3)$$

where  $\alpha(x)$  are spacetime functions that depend on  $U$ , and  $g_s$  is the coupling strength of the strong force. Similarly to QED,  $g_s$  can be expressed in terms of the fine structure constant of the strong interaction,

$$\alpha_s = \frac{g_s^2}{4\pi}. \quad (1.4)$$

Knowing the mathematical representation of  $U$ , it is now possible to study how the quark wavefunction  $\Psi$  behaves under  $SU(3)$  local gauge transformation,

$$\Psi(x) \rightarrow \Psi'(x) = U\Psi(x) = e^{ig_s\alpha(x)\cdot\mathbf{T}} \Psi(x). \quad (1.5)$$

Since  $U$  is a  $3 \times 3$  matrix,  $\Psi$  must include three degrees of freedom, which can be represented by a three-component vector. This new degree of freedom, as mentioned in Sec. 1.1 is termed *color*, and  $SU(3)$  local phase transformation corresponds to a rotation of states in the color space.

Following the same QED formalism, the eight  $SU(3)$  generators can be associated with eight massless bosons mediating the strong force, known as *gluons*. Mathematically, each gluon can be represented by a gauge field  $G_\mu^a$ , where  $a = 1, 2, \dots, 8$ . Moreover, generalizing the concept of electromagnetic field strength tensor, it is possible to introduce a QCD *field strength tensor*  $G_{\mu\nu}^a$  [8], defined as,

$$G_{\mu\nu}^a = \partial_\mu G_\nu^a - \partial_\nu G_\mu^a + g_s f_{abc} G_\mu^b G_\nu^c. \quad (1.6)$$

The last term of this expression arises due to the non-Abelian nature of QCD and must be added to preserve the gauge invariance. Here,  $f_{abc}$  is the structure constant of the  $SU(3)$  group, defined as  $[\lambda_a, \lambda_b] = f_{abc}\lambda_c$ . To preserve the invariance under the local gauge transformation in Eq. 1.5, it is necessary to introduce a *covariant derivative*, obtained

through the *minimal substitution principle* [9],

$$\partial_\mu \rightarrow D_\mu = \partial_\mu - ig_s \frac{\lambda_a}{2} G_\mu^a \quad (1.7)$$

The covariant derivative encodes the interaction between the quark field  $q$  and the gluon field  $G_\mu^a$ , through a coupling strength  $g_s$ .

Knowing the explicit expression of  $D_\mu$ , the full dynamics of the strong force is expressed by the QCD Lagrangian density [8],

$$\mathcal{L}_{\text{QCD}} = -\frac{1}{4} G_{\mu\nu}^a G^{a\mu\nu} + \sum_f \bar{q}_b^f (i\not{D}_{ab} - \delta_{ab} M_f) q_a^f, \quad (1.8)$$

where  $\not{D}_{ab} = \gamma_\mu D_{ab}^\mu$ ,  $M_f$  represents the mass of quark with flavor  $f$ , and  $a$  and  $b$  are the color degrees of freedom.

The first term of the  $\mathcal{L}_{\text{QCD}}$  not only represents the kinematics of gluons but also their self-interaction. Mathematically the gluon self-interaction is encoded in the  $G_\mu^b G_\nu^c \cdot G^{d\mu}$  and  $G_\mu^b G_\nu^c \cdot G^{d\mu} G^{e\nu}$  terms, representing respectively triple and quartic gluon vertices. Thus, gluons both mediate color charge -as the photon mediates electric charge-, and carry color charge themselves. The self-interaction of gluons has fundamental physical implications, such as asymptotic freedom and color confinement.

### 1.2.1 Asymptotic freedom

Asymptotic freedom, discovered independently by Politzer [10] and Wilczek and Gross [11], is a fundamental property of QCD. According to this property, the interactions between quarks become asymptotically weaker as the momentum exchanged in the interaction  $q^2$  increases, or, equivalently, when the distance decreases. In other words, if  $q^2 \rightarrow +\infty$ , then  $\alpha_s \rightarrow 0$ . Asymptotic freedom can be explained considering the vacuum polarization of QCD.

In QED, the fine structure constant  $\alpha_{\text{QED}}$  decreases with the distance. In the presence of an electromagnetic charge, virtual  $e^+ - e^-$  pairs are constantly created and annihilated in the vacuum [12]: thus, the electric field induced by the virtual pairs leads to a screening effect of the original electric charge at large distances.

Vacuum polarization also occurs in the case of QCD, where virtual quark-antiquark pairs and virtual gluons are created in the presence of a color charge particle. However, gluons self-interact, leading to an anti-screening effect at large distances, and overcoming the screening effects of quarks [13]. From a mathematical point of view, the behavior of  $\alpha_s$

as a function of  $q^2$  can be described by the renormalization theory [14],

$$\alpha_s(q^2) = \frac{\alpha_s(\mu^2)}{1 + \frac{33-2N_f}{12\pi}\alpha_s(\mu^2)\ln\left(\frac{q^2}{\mu^2}\right)}, \quad (1.9)$$

where  $\mu^2$  is an arbitrary momentum reference scale and  $N_f$  is the number of quark flavors. Since  $N_f = 6$ , the quantity  $33 - 2N_f$  is always greater than zero and it is thus immediate to verify that the value of  $\alpha_s$  decreases with  $q^2$ .

The value of  $\alpha_s$  has been calculated by many of experiments, such as studies of  $\tau$  lepton decaying into hadrons, measurements of deep inelastic scattering, and studies on jet productions [15]. In Fig. 1.2 the experimental values of  $\alpha_s$  as a function of  $q^2$  are shown. These results fully agree with the predicted QCD asymptotic freedom, representing one of the major successes of quantum chromodynamics.

Since quarks behave as quasi-free particles at high values of  $q^2$  ( $\sim 100$  GeV), perturbative QCD (pQCD) was developed to study physical processes in this regime. When  $\alpha_s \ll 1$ , the equations can be expanded in powers of the coupling constant, and a finite number of the leading terms is sufficient to obtain an approximate solution.

However, perturbative QCD cannot be applied for small  $q^2$  processes, since  $\alpha_s \sim \mathcal{O}(1)$ . Thus, lattice QCD (lQCD) [16] techniques need to be exploited. lQCD has been developed to treat the processes with low momentum transfer: here, the calculations are performed on a discrete lattice of space-time points, where quarks are placed in each discrete site of the lattice, and gluons connect each site. Even if computationally intensive, lQCD calculations represent a fundamental test of the validity of QCD in the non-perturbative regime.

### 1.2.2 Color confinement

Color confinement is the phenomenon according to which color-charged particles cannot be observed as free particles. Thus, quarks exist only in neutral-color objects: they combine in quark-antiquark pairs or in triplets of quarks, forming respectively *mesons* and *baryons* -generally called *hadrons*-.

Quarks interact by exchanging virtual gluons, which self-interact themselves. The interaction between quark and antiquark can be phenomenologically expressed by the effective Cornell potential [18],

$$V(r) = -\frac{4}{3}\frac{\alpha_s}{r} + \kappa \cdot r, \quad (1.10)$$

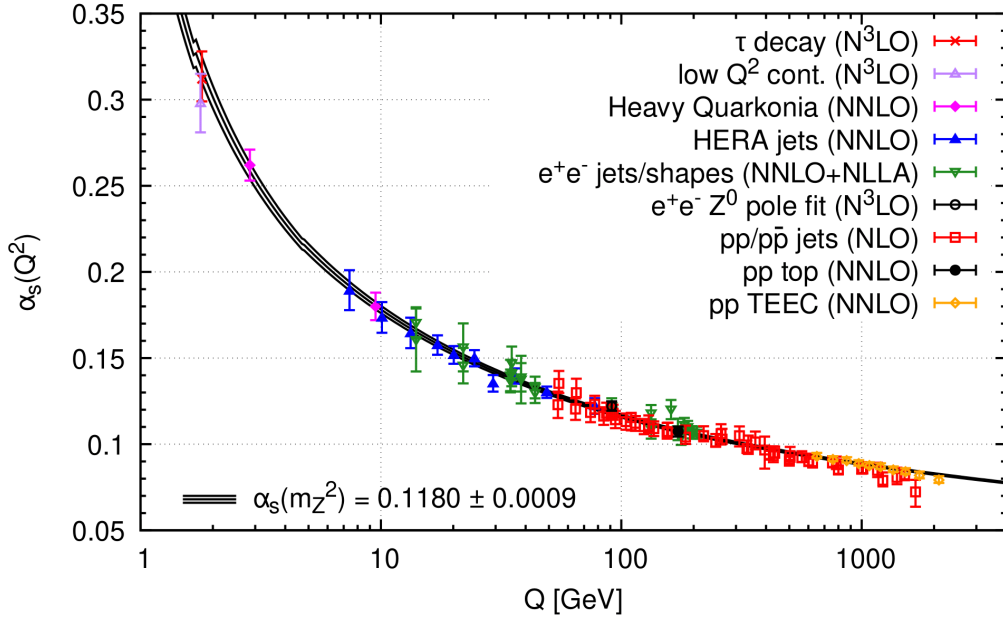


**Figure 1.2:** Measurement of  $\alpha_s$  at different values of the momentum exchanged  $q^2$ .  
Figure taken from [17].

where  $r$  is the distance between the quark and antiquark, and  $\kappa$ , called the *string tension*, is experimentally  $\sim 1$  GeV/fm [9]. Therefore, the quark potential comprises two different contributions: the first term, the Coulomb-like term, dominates at small radii and is repulsive, whereas the attractive strong force contribution  $\kappa \cdot r$  manifests itself at large distances. Since the potential increases with the distance between two quarks, it would require an infinite amount of energy to pull two quarks one away from the other. Therefore, with the increase of the distance  $r$ , at some point it becomes more energetically favorable to create a new quark and antiquark pair, resulting in a color-neutral state again.

### 1.3 The quark-gluon plasma

Given a thermodynamic system composed of a particle species, the *chemical potential* is a physical quantity that represents the change in the free energy of the system due to the change of the particle species number. In the case of QCD, it is useful to define the *baryon chemical potential*  $\mu_B$ , which quantifies the net baryon content of the system. At high-temperature values or high baryon chemical potentials, quarks interact very weakly due to asymptotic freedom. Therefore at extreme energy conditions, color-charged

particles can exist as deconfined, forming a state called *quark-gluon plasma*, QGP. While at first it was expected that the QGP would behave as an electromagnetic plasma, by now it is well established that the QGP is more similar to a strongly interacting fluid [19], and it is thus described using relativistic hydrodynamics. While it is currently believed that the QGP filled the Universe from the first few ms after the Big Bang [20], nowadays the quark-gluon plasma can be created by high-energy heavy-ion collisions at the Large Hadron Collider (LHC) at CERN and at the Relativistic Heavy Ion Collider (RHIC) at BNL.

Studying the QGP is therefore crucial not only for our understanding of the early stage of the Universe but also for assessing the behavior of QCD matter under extreme conditions.

#### 1.3.1 The QCD phase diagram

Depending on the system's temperature and energy density, color-charged particles can be found either confined into hadrons or deconfined in the QGP. Due to the existence of these two different phases, it is possible to build a QCD phase diagram, where the different phases depend on the value of the temperature of the medium  $T$  and on the baryon chemical potential  $\mu_B$ . A possible QCD phase diagram is given in Fig. 1.3, where it is shown that ordinary nuclear matter occurs at low-temperature values  $T \lesssim 100$  MeV, and for  $\mu_B < 1$  GeV.

According to lQCD calculations, the transition between hadrons and the QGP is a smooth crossover for vanishing values of  $\mu_B$  [21, 22]. In a crossover, the thermodynamic properties as pressure and energy density change continuously during the transition. For  $\mu_B = 0$ , lQCD calculations predict that the transition occurs at a pseudo-critical temperature  $T_c \sim 155$  MeV [23]. The LHC center of mass energy exceeds the baryon mass by a factor of  $10^3$ : for this reason, it is expected that at LHC collisions  $\mu_B \sim 0$ . The experimental results are in excellent agreement with this expectation [24]. Since it is also generally believed that the QGP created immediately after the Big Bang was characterized by  $\mu_B = 0$ , the region at vanishing baryon chemical potential represents a fundamental tool to study the early Universe.

The prediction of the phase diagram behavior for non-negligible values of  $\mu_B$  is, on the other hand, more involved, and it is currently not clear if a smooth transition between the two phases occurs for every value of  $\mu_B$ , or if the crossover changes to a first-order phase transition at a critical point [25]. Collisions at future heavy-ion collision facilities like Fair and NICA, which take place far away from  $\mu_B = 0$ , will be able to help shed light on this unsolved issue.

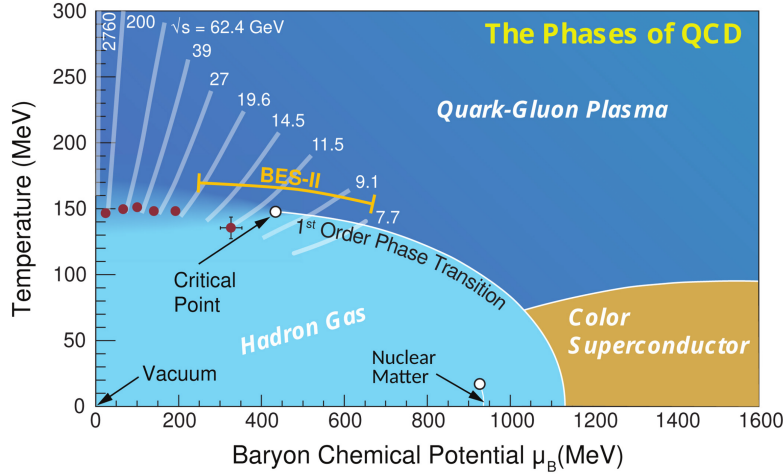


**Figure 1.3:** The QCD phase diagram as a function of the baryon density and of the medium temperature. Figure taken from [27].

Finally, for  $\mu_B \gg 1$  GeV and temperatures of  $T \lesssim 100$  MeV, QCD matter is predicted to enter a color superconductive phase [26]. The understanding and modeling of this region of the QCD phase diagram is not of less importance than the others, since it is believed that these physical conditions correspond to the ones present in the cores of neutron stars [26].

### 1.3.2 Heavy-ion collisions

Heavy-ion collisions (HIC) are collisions between beams of ions characterized by a high atomic number (Pb, Au, Xe). In the case of LHC and RHIC highest energies, where the energy at the center of mass is of the order of  $\mathcal{O}(\text{TeV})$  and of  $\mathcal{O}(10^2 \text{ GeV})$  respectively, these collisions are ultra-relativistic. If not stated otherwise, the following description will focus on HIC occurring in such energy systems.

In the HIC coordinate system, the  $z$ -axis usually represents the longitudinal direction, parallel to the initial beam. Moreover, due to the relativistic speed of the collision, when studying the behavior of particles created in HIC, it is necessary to define a longitudinal proper time  $\tau = \sqrt{t^2 - z^2}$ , which represents a Lorentz boost-invariant quantity. A schematic of heavy-ion collision evolution in the  $[z, t]$  plane is given in Fig. 1.4.

Since the QGP phase exists only for  $\tau \sim 10 \text{ fm} = 10^{-23} \text{ s}$ , all the properties of the plasma can be inferred only from indirect observations. It is thus of fundamental importance to understand the dynamics of heavy-ion collisions, which can be schematically described as follows:

- **Initial state.** The collision of two nuclei occurs. Due to the high relativistic energy, the ions are Lorentz contracted in the longitudinal direction, and, at first approximation, the collision happens at a single instant of time  $t = 0$ , and in a single longitudinal position  $z = 0$ . Due to the high energy of the beams, inelastic scattering is the dominant interaction between particles.
- **Pre-equilibrium phase.** For  $0 < \tau < 1$  fm, a non-thermalized state with strongly interacting fields is formed. During this state, partons interact mainly through hard scattering, leading to the production of high momenta particles and of heavy quarks, i.e. charm and bottom quarks. However, the precise dynamic of this state is still to be understood.
- **QGP phase.** After the pre-equilibrium phase, the system approaches local thermal equilibrium: partons start interacting via soft scattering and the QGP is formed. Due to thermal equilibrium, this state, which exists for  $1 < \tau < 10$  fm [28], can be described by relativistic hydrodynamics equations. This significantly simplifies simulating the collective dynamics of the system.
- **Hadronization.** The QGP expands due to pressure gradients, and it cools down. Eventually, the system reaches the pseudo-critical temperature  $T_c$ : here, a smooth phase transition occurs and partons get confined into hadrons. Inelastic collisions still happen among hadrons, so that chemical and kinetic equilibrium are maintained.
- **Chemical freeze-out.** As the system further expands, the rate of inelastic collisions among hadrons decreases: when the system reaches the chemical freeze-out temperature  $T_{\text{ch}}$ , the rate becomes too small to maintain chemical equilibrium. After this point, the chemical composition of the hadron gas is fixed and does not change anymore, except for the presence of resonance decays.
- **Kinetic freeze-out.** As the density drops even further, the elastic collision rate decreases, so that kinetic equilibrium cannot be maintained. When the system reaches the kinetic freeze-out temperature,  $T_{\text{kin}}$ , particles do not exchange momentum anymore, and they freely stream toward the detectors.

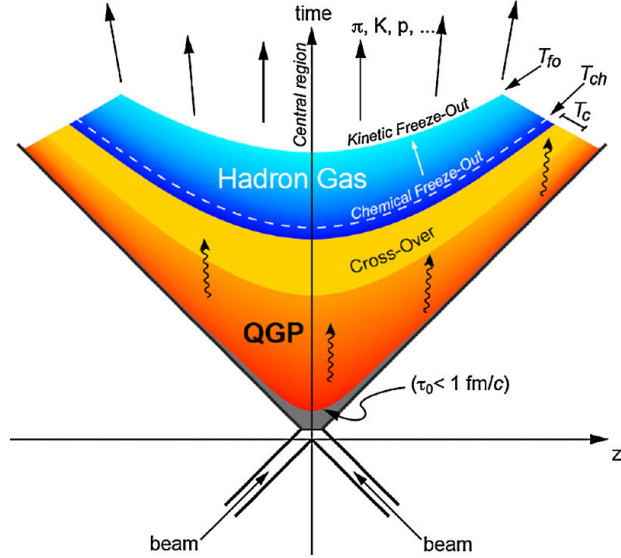


**Figure 1.4:** Space-time diagram of a heavy-ion collision of two nuclei colliding at time  $t=0$  and longitudinal position  $z=0$ . Figure taken from [24].

## 1.4 Experimental observables of the QGP

Many experimental results show that the QGP can be effectively described as a strong interacting fluid: this translates into saying that the QGP exhibits collective behaviors, and cannot be considered as the simple superposition of individual particles.

As underlined in the previous section, the QGP is not directly observable: the only possible measurements involve hadrons or their decay products, which carry precious information from the early hot stage. On one hand, low-momentum ( $p_T \lesssim 3 \text{ GeV}$ ) light partons, known as *soft probes*, are strongly coupled to the medium, and their mean-free path is very small with respect to the size of the system. Light hadrons are produced in the late stage of the fireball and carry information about the collective behavior of the QGP: soft probes are thus best suited to study the hydrodynamics of the plasma. On the other hand, heavy quarks and high-momentum partons, called *hard probes*, are produced at the beginning of the collision via hard scattering and do not necessarily reach full thermalization with the rest of the medium. Therefore, these particles carry information about all the evolution stages of the fireball, making them essential probes to infer the properties of the QGP.

In order to characterize the particles produced from the QGP at the freeze-out, it is useful to define some kinematic quantities, such as the transverse momentum and the

rapidity, respectively defined as,

$$p_T = \sqrt{p_x^2 + p_y^2}, \quad (1.11)$$

$$y = \frac{1}{2} \ln \left( \frac{E + p_z}{E - p_z} \right), \quad (1.12)$$

where  $E$  represents the particle energy, and  $\vec{p} = (p_x, p_y, p_z)$  its momentum.

Having defined the transverse momentum and the rapidity, it is now possible to introduce one of the most important experimental observables used to infer the properties of the particles produced at the freeze-out, namely the differential transverse momentum yield,

$$E \frac{d^3 N}{dp^3} = \frac{1}{2\pi} \frac{d^2 N}{p_T dp_T dy}. \quad (1.13)$$

The  $p_T$  spectrum, which is a Lorentz invariant quantity, will be used in the present work as the main observable to compare the developed model with the experimental data.

Moreover, by studying the  $p_T$  invariant spectrum, information on the collective transverse expansion of the QGP, the so-called *radial flow*, can be inferred. The partons in the QGP experience an isotropic boost due to the radial flow: this effect will thus translate into an increase of the average  $p_T$  of the produced hadrons. Since the radial flow causes the hadrons to acquire a common radial velocity, the push at larger values of transverse momentum is more pronounced for heavier particles [29].

### 1.4.1 Anisotropic flow

As it will be discussed in Sec. 2.1, ions do not always collide head-on. In the case of semi-central collisions, the overlap region of the two colliding ions in the  $[xy]$  plane is not azimuthally symmetric, but approximately *almond-shaped*, as shown in Fig. 1.5. Thus, it is possible to define a *reaction plane* as the symmetry plane of the overlap region, where the beam direction and the vector connecting the center of the two ions lie.

When the system thermalizes, the initial spatial anisotropy of the overlap zone translates into an initial energy density anisotropy. Therefore, pressure gradients between the fireball and the surrounding vacuum will be larger in the reaction plane, leading after some time to a larger fluid velocity in the same direction. This means that after hadronization more particles will fly in the reaction plane direction. In other words, an anisotropy in the angular distribution of the produced hadrons will be observed. A Fourier decomposition

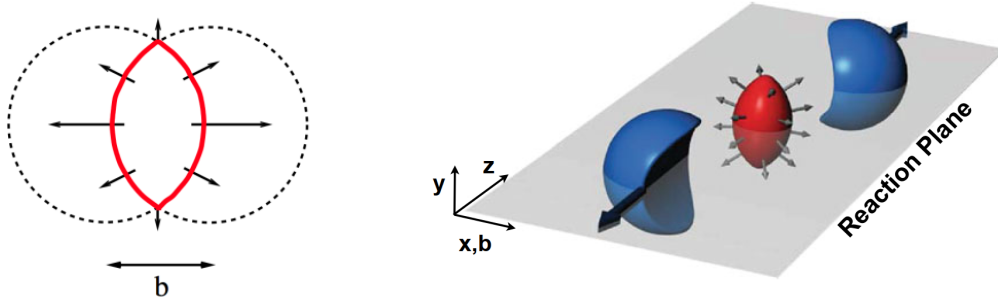


**Figure 1.5:** Semi-central heavy-ion collision, with impact parameter  $b$ , and overlap region marked in red, in the  $[xy]$  plane (left panel) and in 3D (right panel). Arrows illustrate the elliptic flow which results from the initial pressure gradients. Figures taken from [30] and [31].

of the azimuthal dependence of the particle spectrum can quantify this anisotropy,

$$\frac{dN}{d\phi} = \frac{N}{2\pi} \left[ 1 + 2 \sum_m v_m \cos(m(\phi - \psi_m)) \right], \quad (1.14)$$

where  $\phi$  represents the azimuthal angle of the produced particle in the transverse plane to the beam,  $\psi_m$  is the reaction plane angle, and  $v_n$  are generally called *flow coefficients*. The second flow coefficient  $v_2$ , known as the *elliptic flow*, reflects the azimuthal anisotropy of particle distribution caused by the almond-like initial geometry. The elliptic flow  $v_2$  represents the largest contribution to the particle distribution anisotropy in non-central collisions, whereas the higher-order coefficients are mostly related to initial state fluctuations. If QGP was an ideal gas of non-interacting partons, the initial overlap anisotropy would not translate into pressure gradients, and the fireball would expand isotropically in all directions. Measurements at RHIC and at LHC showed a positive azimuthal anisotropy of the final particle spectra, quantified by elliptic flow measurements [32]. This experimental result represents one of the most compelling evidences that the QGP is indeed created in heavy-ion collisions, and can be treated as a strong interacting fluid.

Moreover, due to the presence of the radial flow, a characteristic mass ordering at low  $p_T$  is observed when studying the elliptic flow. As underlined in the previous section, radial flow leads to a depletion in the momentum spectrum by pushing the hadrons towards larger momenta, and since the radial flow depends on the particle mass, this depletion is more pronounced for heavier particles. As a result, for a given value of  $p_T$ , heavier particles have smaller  $v_2$  values compared to lighter ones [33].

## 2 Heavy-ion-collision modeling

### 2.1 Initial state of heavy-ion collisions

Colliding ions are extended objects that are Lorentz contracted in the beam direction: the number of particles produced by each heavy-ion collision depends therefore on the geometry of the collision itself. Most of the time not all the nucleons participate in the collision: the interacting nucleons are usually referred to as *participants*, while nucleons almost unaffected by the collision are called *spectators*, as shown in Fig. 2.1.

Every heavy-ion collision is characterized by an impact parameter  $b$ , defined as the distance between the center of the two colliding nuclei. The value of  $b$  cannot be measured experimentally: thus, HIC are classified according to their *centrality class*. The basic assumption underlying centrality classes is that the impact parameter  $b$  is monotonically related to the number of produced particles, the so-called *multiplicity*. Thus, events with a small impact parameter (*central* collisions) will produce a large amount of charged particles, in contrast to large- $b$  collisions (*peripheral* collisions), characterized by a large number of spectators.

To quantify the centrality classes of an ensemble of events, it is first possible to measure the multiplicity of charged particles  $dN_{\text{ch}}$  for each event. Ordering the events according to their multiplicity, a distribution of  $dN_{\text{evt}}/dN_{\text{ch}}$  as a function of  $N_{\text{ch}}$  can then be built. From here, centrality classes are defined by binning the distribution on a fraction of its total integral [35]: in other words, the centrality class 0 – 5% corresponds to the 5% of collisions with the largest multiplicity, the 5 – 10% class to the second 5% with largest multiplicity, and so on. Alternatively, centrality classes can be determined using the distribution of the hadronic cross-section  $d\sigma/dN_{\text{ch}}$ , as shown in Fig. 2.2. However, since the cross-section is not directly measurable, for practical implementations it is easier to use measurable observables directly correlated with it.

Moreover, by modeling the geometry of each HIC event (for instance with a Glauber model), it is possible to associate the impact parameter, or the number of participants  $N_{\text{part}}$ , to each centrality class.

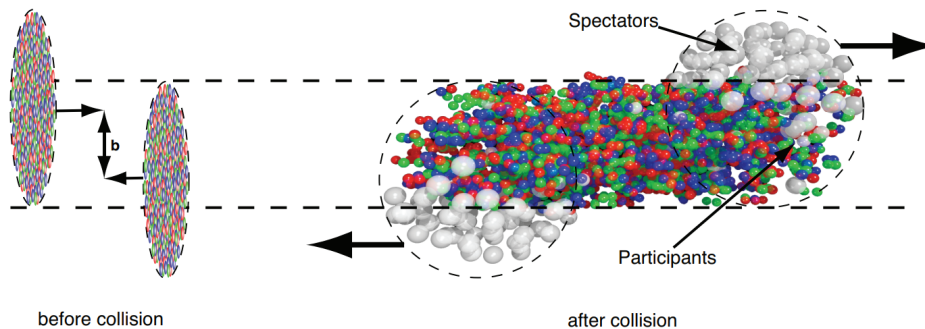


**Figure 2.1:** Left: Two heavy ions before the collision, characterized by an impact parameter  $b$ . Right: The spectators continue their path unaffected, while in the participant zone particle production takes place. Figure from [34].

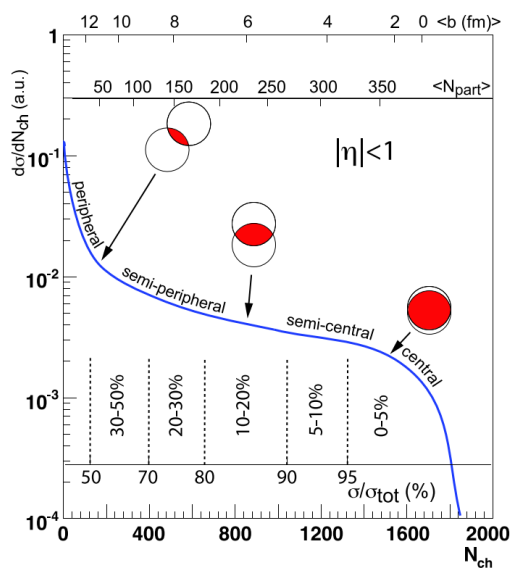


**Figure 2.2:** Example of the distribution  $d\sigma/dN_{ch}$  as a function of  $N_{ch}$ . The plotted distribution and values represent only an example and do not correspond to an actual measurement. Figure from [35].

### 2.1.1 The Glauber model

The Glauber model (GM) is a semiclassical model [36] developed to address the problem of high energy scattering with composite particles. The GM is based on the optical eikonal approximation, which assumes that projectile nucleons travel along straight lines and undergo multiple independent sub-collisions with nucleons in the target. This approximation is justified since at very high energy, the longitudinal momentum of the nucleon exceeds the transverse component by several orders of magnitude. Thus, nucleons will be essentially undeflected as the nuclei pass through each other, and the nucleon trajectory can be described as a sum of all the phase shifts received at the scattering centers inside the target.

The GM neglects that the nucleons are quantum mechanical objects, but allows for the implementation of all the geometric aspects of the multiple scattering process. The hypothesis of independent linear trajectories of the nucleons allows to develop simple analytic expressions for the nucleus-nucleus interaction cross-section in terms of nucleon-nucleon inelastic cross-section  $\sigma_{\text{NN}}^{\text{in}}$ .

Nowadays, the *Glauber Monte Carlo* (GMC) approach is widely used in heavy-ion collision. The GMC models the nucleus as made of uncorrelated nucleons, sampling the position of each nucleon as randomly generated according to the nuclear density function. The nuclear charge density, which represents the input for the Glauber model, is usually parameterized by a Woods-Saxon distribution [37],

$$\rho(r) = \frac{\rho_0}{1 + e^{(r-R)/a_0}}, \quad (2.1)$$

where  $\rho_0$  represents the nucleon density in the center of the nucleus,  $a_0$  is the *skin depth*, and  $R$  referred to as *nuclear radius*, is the distance from the nucleus center after which the density is halved.

After defining their nuclear density, two nuclei can then be arranged with impact parameter  $b$  and projected onto the  $[xy]$  plane. The value of  $b$  is usually sampled from a given probability distribution  $P(b)db$ , whose explicit form depends on the specific GM simulation. Knowing  $\sigma_{\text{NN}}^{\text{in}}$ , the interaction probability between the two nuclei can then be calculated.

Despite its relative simplicity, the Glauber model has qualitatively fit many experimental results [35] and inspired many similar models.

### 2.1.2 The TREnTo model

TREnTo is an initial condition model [38] for high-energy nucleus-nucleus collisions, which generates initial entropy profiles without assuming specific physical mechanisms for entropy production, pre-equilibrium dynamics, or thermalization.

Within this model, the position of each nucleon inside a given nucleus is sampled from the Wood-Saxon distribution given in 2.1. Since in the GM the nucleons are the relevant degrees of freedom of the collision, a *nucleon density*  $\rho_{\text{nucleon}}(x, y, z)$  must also be defined, which physically represents the probability per unit of volume to find a given nucleon inside a given nucleus in the position  $(x, y, z)$ .

Due to the Lorentz contraction, in its first version TREnTo describes nuclei as 2-dimensional objects, which collide at the center of the reference frame. Supposing the beam travels along the  $z$ -axis, the probability per unit of transverse area of finding the nucleon located in  $(x, y)$ , the so-called *thickness function*, is given by integrating the nucleon density with respect to  $z$  [38]. In TREnTo the thickness function is described as a Gaussian distribution with width  $w$ ,

$$T_{\text{nucleon}}(x, y) = \int dz \rho_{\text{nucleon}}(x, y, z) = \frac{1}{2\pi w^2} \exp\left(-\frac{x^2 + y^2}{2w^2}\right). \quad (2.2)$$

However, to account for the experimentally observed proton-proton multiplicity fluctuations [39], a *fluctuated thickness function* is often used instead,

$$T_{\text{nucleon}}(x, y) = m \int dz \rho_{\text{nucleon}}(x, y, z), \quad (2.3)$$

where the factor  $m$  represents an independent random weight sampled from a gamma distribution with unit mean,

$$P_k(m) = \frac{k^k}{\Gamma(k)} m^{k-1} e^{-km}. \quad (2.4)$$

The value of  $k$ , called the *shape parameter*, can be tuned according to the experimental data: small values of  $k$  ( $0 < k < 1$ ) correspond to large multiplicity fluctuations, while large values of  $k$  translate into a suppression of fluctuations.

Let us now consider two nucleons  $a$  and  $b$ , which belong to the two different colliding nuclei  $A$  and  $B$  respectively. The probability of collision between these two nucleons can

be calculated as [40],

$$P_{\text{coll}} = 1 - \exp \left[ -\sigma_{gg} \int dx dy \int dz \rho_a \int dz \rho_b \right], \quad (2.5)$$

where  $\sigma_{gg}$  represents an effective parton-parton cross-section, while the integral in the exponential represents the overlap integral of the two nucleons' thickness functions.

First, in TRENTo the probability of collision of  $a$  and  $b$  is calculated to determine if the two nucleons collide: if so,  $a$  and  $b$  are labeled as ‘‘participants’’. To compute the total number of participant nucleons, the same procedure is repeated for each nucleon-nucleon pair. Knowing the number of participants  $N_{\text{part}}$  of the nucleus  $A$ , its fluctuated thickness function will be given by summing the participants' contribution,

$$T_A(x, y) = \sum_{i=1}^{N_{\text{part}}} m_i \int dz \rho_{\text{nucleon}}(x - x_i, y - y_i, z - z_i). \quad (2.6)$$

One of the main assumptions of TRENTo is that there exists a scalar function  $f(T_A, T_B)$  that connects the thickness functions of the two colliding nuclei with the entropy deposition. Moreover, the function  $f$  is proportional to the entropy created at mid-rapidity at the initial time  $\tau = \tau_0$ ,

$$f \propto dS/dy|_{\tau=\tau_0}. \quad (2.7)$$

There are several possibilities on how to build  $f$  as a function of  $T_A$  and  $T_B$ . Taking into account recent experimental constraints [38, 41], TRENTo identifies  $f$  with the *reduced thickness function*, defined as,

$$f \equiv T_R(p; T_A, T_B) = \left( \frac{T_A^p + T_B^p}{2} \right)^{1/p}. \quad (2.8)$$

Different values of  $p$  correspond to different physical mechanisms for entropy production. For  $p = 1$ , the reduced thickness corresponds to the arithmetic average of  $T_A$  and  $T_B$ , and each nucleon deposits the same amount of entropy. On the other hand for  $p = 0$ ,  $T_R = \sqrt{T_A T_B}$ , and a single symmetric amount of entropy is deposited at the mid-point of the collision.

After fixing  $p$  and calculating the reduced thickness function  $T_R$ , it is thus possible to infer the value of  $dS/dy$  from 2.7, up to a normalization constant. Moreover, it is worth noting that to a good approximation [42], the average charged-particle multiplicity  $\langle N_{\text{ch}} \rangle$

is proportional to the total initial entropy,

$$\langle N_{\text{ch}} \rangle \propto \int dx dy T_R(x, y). \quad (2.9)$$

In this work, the entropy profile  $dS/dy$  will be used as the initial condition, from where it is possible to evolve the system through hydrodynamics equations.

## 2.2 Hydrodynamic description of QGP

Fluid dynamics describes the collective behavior of microscopic degrees of freedom of a system making use of its macroscopic quantities, such as transport properties and equations of state.

The QGP behaves as a strong-interacting fluid, and can thus be modeled by relativistic fluid-dynamic equations. While first principle calculations of the macroscopic fluid properties of the QGP are still challenging, phenomenological and theoretical studies are motivated by an increasing amount of experimental results.

The equations of motion of a relativistic fluid are usually obtained by imposing the conservation of some physical quantities, which, in the case of heavy-ion collisions, are the energy, the momentum, and the number of charges of the system. The conservation of energy and momentum is summarized by the energy-momentum tensor  $T^{\mu\nu}$ , which describes the density and flux of energy and momentum in  $(t, x, y, z)$  space. On the other hand, the conservation of the charges' number can be imposed by introducing a current  $N^\mu$  for each conserved charge. The explicit formulation of these quantities depends on the characteristics of the fluid studied and will be addressed in the following two sections.

### 2.2.1 Ideal fluid dynamics

A fluid can be defined as ideal if it is characterized by three properties: it is incompressible, it moves in a laminar regime, and it does not show any internal resistance to flow, or, in other words, it has zero viscosity. Even if no such fluid exists in practice, ideal fluid dynamics provides a simplified model description of real fluid dynamics.

For an ideal fluid, the energy-momentum tensor  $T^{\mu\nu}$  can be expressed as a function of the fluid energy density  $\epsilon(x)$ , and of its pressure  $P(x)$ . In the system rest frame, where

the fluid is at rest, it can be shown [43] that  $T^{\mu\nu}$  is given by,

$$T^{\mu\nu} = \begin{pmatrix} \epsilon(x) & 0 & 0 & 0 \\ 0 & P(x) & 0 & 0 \\ 0 & 0 & P(x) & 0 \\ 0 & 0 & 0 & P(x) \end{pmatrix}. \quad (2.10)$$

Supposing for simplicity that the system is characterized by only one conserved charge  $Q$  with density  $n$ , the current associated with  $Q$  in the fluid rest frame can be expressed as,

$$N^\mu = (n, 0, 0, 0). \quad (2.11)$$

To obtain the energy-momentum tensor and the conserved current in a general frame, it is first necessary to introduce the fluid 4-velocity  $u^\mu(x)$ , which is defined as the rate of change of the four-position  $x^\mu = (t, \vec{x})$  with respect to the proper time  $\tau$ ,

$$u^\mu(x) = \frac{dx^\mu}{d\tau} = \left( \frac{dt}{d\tau}, \frac{d\vec{x}}{d\tau} \right) = \gamma \cdot (1, \vec{v}), \quad (2.12)$$

where  $\gamma = \frac{1}{\sqrt{1-v^2}}$  is the Lorentz factor,  $\tau$  the proper time, and  $\vec{v}$  the fluid velocity. Of course in the reference frame where the fluid is at rest,  $u^\mu = (1, 0, 0, 0)$ .

One of the most important characteristics of the 4-velocity is the unitarity of its norm,

$$u^2 = g_{\mu\nu}u^\mu(x)u^\nu(x) = \gamma^2(-1 + v^2) = \frac{1}{1-v^2}(-1 + v^2) = -1, \quad (2.13)$$

where  $g_{\mu\nu} = \text{diag}(-1, +1, +1, +1)$  is the metric in Minkowski space. Since its norm is fixed,  $u^\mu$  depends only on 3 independent components.

Starting from Eq. 2.10 and 2.11, it is possible to apply a Lorentz boost to  $T^{\mu\nu}$  and to  $N^\mu$  in the local rest frame with respect to the 4-velocity field  $u^\mu(x)$ , leading to [43],

$$T^{\mu\nu} = \epsilon u^\mu u^\nu + P (g^{\mu\nu} + u^\mu u^\nu) = \epsilon u^\mu u^\nu + P \Delta^{\mu\nu}, \quad (2.14)$$

$$N^\mu = n u^\mu, \quad (2.15)$$

where  $\Delta^{\mu\nu}$  is the projector tensor orthogonal to the fluid velocity,  $\Delta^{\mu\nu} \equiv g^{\mu\nu} + u^\mu u^\nu$ .

Knowing the explicit form of  $T^{\mu\nu}$  and of  $N^\mu$  it is now possible to ask for energy-

momentum and charge conservation,

$$\partial_\mu T^{\mu\nu} = 0, \quad (2.16)$$

$$\partial_\mu N^\mu = 0, \quad (2.17)$$

which lead to the following equations of motion,

$$u^\mu \partial_\mu \epsilon + (\epsilon + P) \nabla_\mu u^\mu = 0, \quad (2.18)$$

$$(\epsilon + P) u^\mu \nabla_\mu u^\nu + (g^{\mu\nu} + u^\nu u^\mu) \partial_\mu P = 0, \quad (2.19)$$

$$\partial_\mu (u^\mu n) = 0 \quad (2.20)$$

This system represents 5 equations in 6 variables:  $P$ ,  $\epsilon$ ,  $u^\mu$ , and  $n$ . For this reason, additionally an Equation of State (EoS)  $P(T)$  has to be introduced to form a closed system of equations. The Equation of State is a thermodynamic relation between state variables, usually expressed by the pressure as a function of temperature.

Ideal fluid dynamics cannot explain the observed momentum anisotropies that develop in the QGP lifetime, introduced in Sec. 1.4.1. Thus, in order to correctly describe the QGP, it is necessary to introduce dissipative corrections, which take into account non-zero viscosity contributions.

### 2.2.2 Viscous fluid dynamics

In fluid dynamics, viscosity is a physical quantity that measures the internal frictional resistance of a fluid to deformation or flow. In general, viscosity depends on the fluid state, such as its temperature, pressure, and rate of deformation. Zero viscosity can be observed only at very low temperatures in superfluids; otherwise, the second law of thermodynamics requires all real fluids to have positive viscosity.

In general, it is possible to distinguish between two different types of viscosity: the shear viscosity  $\eta$  and the bulk viscosity  $\zeta$ . The shear viscosity is a measure of the fluid resistance to flow under the action of a force parallel to the fluid cross-section, usually referred to as *shear stress*. The shear viscosity quantifies the internal friction between adjacent layers of fluid as they move relative to each other. On the other hand, bulk viscosity represents the fluid resistance to changes in volume, describing its response to compression or expansion.

The viscosities  $\eta$  and  $\zeta$  are usually called *transport coefficients* since they describe the microscopic momentum exchange and therefore the dissipation of energy. Usually, strongly

interacting quantum field theories compute the value of the diffusion coefficients divided by the entropy density  $s$  [44]. Thus, for the sake of consistency, the dimensionless quantities  $\eta/s$  and  $\zeta/s$  will also be used throughout this thesis to characterize shear and bulk viscosity contributions.

To account for the presence of both types of viscosity, the ideal  $T^{\mu\nu}$  in Eq. 2.14 has to be modified as follows,

$$T^{\mu\nu} = T_{\text{ideal}}^{\mu\nu} + \Pi^{\mu\nu} = \epsilon u^\mu u^\nu + (P + \pi_{\text{bulk}})\Delta^{\mu\nu} + \pi^{\mu\nu}, \quad (2.21)$$

where  $\pi^{\mu\nu}$  is a symmetric tensor having as entries the shear-stress components and orthogonal to the fluid velocity ( $\pi^{\mu\nu}u_{\mu\nu} = 0$ ), while  $\pi_{\text{bulk}}$  is the bulk viscous pressure, measuring the deviation of the isotropic pressure.

The presence of dissipative effects in a fluid can cause a non-uniform concentration of the charges, leading to the emergence of the *diffusion current*, defined as the flow of charges caused by variation in their concentration. The diffusion current is described by the 4-vector  $\nu^\mu$ , and, in analogy to the case of bulk and shear viscosity, it is related to a transport coefficient, the *charge-diffusion coefficient*  $\kappa_n$ .

Taking into account the effect of the diffusion, the conserved charge current in the dissipative case can be expressed as,

$$N^\mu = N_{\text{ideal}}^\mu + \nu^\mu = nu^\mu + \nu^\mu. \quad (2.22)$$

Analogously to the ideal case, the equations of motion can be derived from the conservation laws in Eq. 2.16 and in 2.17, leading to,

$$u^\mu \partial_\mu \epsilon + (\epsilon + P + \pi_{\text{bulk}})\nabla_\mu u^\mu + \pi^{\mu\nu}\nabla_\mu u_\nu = 0, \quad (2.23)$$

$$(\epsilon + P + \pi_{\text{bulk}})u^\mu \nabla_\mu u^\nu + \Delta^{\mu\nu}\partial_\mu(P + \pi_{\text{bulk}}) + \Delta_\nu^\mu \nabla_\rho \pi^{\rho\nu} = 0, \quad (2.24)$$

$$\partial_\mu(nu^\mu + \nu^\mu) = 0. \quad (2.25)$$

In this form, this system of equations is not closed and needs additional information on  $\pi^{\mu\nu}$ ,  $\pi_{\text{bulk}}$  and  $\nu^\mu$ . The *first-order hydrodynamics* bases its equations on imposing the validity of the second thermodynamic principle,  $\nabla_\mu(su^\mu) \geq 0$ , where  $s$  is the entropy density [43, 45]. This formulation leads to an expression of the dissipative currents in terms of first-order derivatives with respect to the fluid velocity, the temperature, and the

ratio between chemical potential corresponding to the conserved charge and temperature,

$$\pi^{\mu\nu} = -2\eta \left( \frac{1}{2} \Delta^{\mu\alpha} \Delta^{\nu\beta} + \frac{1}{2} \Delta^{\mu\beta} \Delta^{\nu\alpha} - \frac{1}{3} \Delta^{\mu\nu} \Delta^{\alpha\beta} \right) \nabla_\alpha u_\beta = -2\eta \sigma^{\mu\nu}, \quad (2.26)$$

$$\pi_{\text{bulk}} = -\zeta \nabla_\mu u^\mu, \quad (2.27)$$

$$\nu^\mu = \kappa_n \Delta_\nu^\mu \nabla^\nu \left( \frac{\mu}{T} \right). \quad (2.28)$$

These equations represent the relativistic generalization of the Navier-Stokes theory [43]. Even if it is the most straightforward procedure, this formulation violates the causality principle and it is linearly unstable [46].

A viable candidate for a relativistic formulation of dissipative fluid dynamics, which does not show causality problems, is the so-called *second-order hydrodynamics* developed by Müller, Israel and Stewart [47, 48]. The main idea behind this theory is to provide dynamical equations for the shear-stress tensor  $\pi^{\mu\nu}$ , for the bulk viscous pressure  $\pi_{\text{bulk}}$  and for the diffusion current  $\nu^\mu$  which evolve according to an equation of motion,

$$\dot{\pi}^{\mu\nu} = -\frac{1}{\tau_{\text{shear}}} [\pi^{\mu\nu} - 2\eta \sigma^{\mu\nu}], \quad (2.29)$$

$$\dot{\pi}_{\text{bulk}} = -\frac{1}{\tau_{\text{bulk}}} [\pi_{\text{bulk}} + \zeta \nabla_\mu u^\mu], \quad (2.30)$$

$$\dot{\nu}^\mu = -\frac{1}{\tau_n} \left[ \nu^\mu - \kappa_n \Delta_\nu^\mu \nabla^\nu \left( \frac{\mu}{T} \right) \right]. \quad (2.31)$$

Using this approach, the equations of motion depend on additional second-order transport coefficients, the *relaxation times*  $\tau_{\text{shear}}$ ,  $\tau_{\text{bulk}}$ , and  $\tau_n$  which represent the relaxation of  $\pi^{\mu\nu}$ ,  $\pi_{\text{bulk}}$ , and  $\nu^\mu$  respectively towards their Navier-Stokes values. Relaxation times are of fundamental importance in ensuring that causality is preserved.

The Müller-Israel-Stewart equations of motions form a closed system of first-order, quasi-linear partial differential equations for the energy density  $\epsilon$ , the independent components of fluid velocity, for the shear-stress tensor components, and for bulk viscous pressure. However, these equations cannot be solved analytically: therefore, in order to describe the QGP dynamics, numerical methods need to be developed.

### 2.2.3 FluiduM package

To describe the dynamics of heavy-ion collisions, it is of fundamental importance to choose a suitable coordinate system. As a matter of fact, to discuss the experimentally observed symmetries of HIC, the Cartesian coordinates  $(t, x, y, z)$  are not well suited.

A natural choice for the center of the system is at the center of the collision ( $x = y = z = 0$ ), at the initial laboratory time  $t = 0$ . The time  $t$  and the longitudinal coordinate  $z$  can be expressed as a function of the proper time, also called *Bjorken time*  $\tau$ , and of the pseudorapidity  $\eta$  respectively defined as,

$$\begin{cases} \tau = \sqrt{t^2 - z^2} \\ \eta = \operatorname{arctanh}(z/t). \end{cases} \quad (2.32)$$

When the particle energy is much larger than its mass, the pseudorapidity  $\eta$  coincides with the rapidity defined in Eq. 1.12. For this reason, throughout this thesis, we will use these two terms interchangeably.

On the other hand, in the transverse plane, it is convenient to use cylindrical coordinates such that the radial coordinate  $r$  and the azimuthal angle  $\phi$  are written as,

$$\begin{cases} r = \sqrt{x^2 + y^2} \\ \phi = \operatorname{arctan}(y/x). \end{cases} \quad (2.33)$$

The equations in 2.32 and in 2.33 allow the transformation from the Cartesian coordinate system to a new system of coordinates  $(\tau, \eta, r, \phi)$ . The latter is particularly suited to discuss two important symmetry transformations: the approximate azimuthal rotation symmetry  $\phi \rightarrow \phi + \Delta\phi$  and the approximate longitudinal rapidity boost symmetry  $\eta \rightarrow \eta + \Delta\eta$ . Using this coordinate system, every space-time point can be described in terms of  $\tau$ ,  $\eta$ ,  $r$ , and  $\phi$ .

In this thesis we will employ the recently developed package *FluiduM* [49], which evolves the fluid fields numerically according to their equations of motions, starting from the provided initial conditions. One of the most important assumptions of *FluiduM* is the possibility of describing the system in terms of a vector, called *Nambu spinor*  $\Phi(\tau, r, \phi, \eta)$  characterized by  $N$  independent components, such as the temperature of the fluid  $T$ , its 4-velocity  $u^\mu$ , the shear stress tensor, the bulk viscous pressure and any other field necessary for the local description. Moreover, it is assumed that the evolution of the system is determined by a set of hyperbolic, quasi-linear partial differential equations, written as,

$$\mathbf{A}\partial_\tau\Phi + \mathbf{B}\partial_r\Phi + \mathbf{C}\partial_\phi\Phi + \mathbf{D}\partial_\eta\Phi - \mathbf{S} = 0, \quad (2.34)$$

where  $\mathbf{A}$ ,  $\mathbf{B}$ ,  $\mathbf{C}$ , and  $\mathbf{D}$  are  $N \times N$  coefficient matrices, while  $\mathbf{S}$ , called the *source term*, is an  $N$ -component vector. Both the coefficient matrices and the source term depend on

$\Phi$ ,  $r$ , and  $\tau$ , and the explicit dependence on the last two terms originates from the choice of coordinates.

A further assumption made in FluiduM is that  $\Phi$  can be written as the summation of a background field spinor  $\Phi_0(\tau, r)$  symmetric under azimuthal rotations and boosts in the  $z$  direction, and a symmetry-breaking spinor  $\Phi_1(\tau, r, \phi, \eta)$  accounting for deviations from the background,

$$\Phi(\tau, r, \phi, \eta) = \Phi_0(\tau, r) + \epsilon \Phi_1(\tau, r, \phi, \eta), \quad (2.35)$$

where  $\epsilon$  is a formal expansion parameter and can be set equal to 1.

After decomposing  $\Phi$  into two contributions, it is now possible to insert Eq. 2.35 into 2.34. Taking into account only terms of zeroth-order terms in  $\epsilon$ , the evolution equation for the background spinor reads as,

$$\mathbf{A}_0(\Phi_0, \tau, r) \partial_\tau \Phi_0(\tau, r) + \mathbf{B}_0(\Phi_0, \tau, r) \partial_r \Phi_0(\tau, r) - \mathbf{S}_0(\Phi_0, \tau, r) = 0, \quad (2.36)$$

where  $\mathbf{A}_0$  and  $\mathbf{B}_0$  correspond to the projections of  $\mathbf{A}$  and  $\mathbf{B}$  to the reduced parameter space of independent components, evaluated on the background configuration  $\Phi_0$  [49]. Therefore, the equations of motion for  $\Phi_0$  are now partial differential equations in  $1 + 1$  dimensions. Due to the symmetry constraints,  $\Phi_0$  depends on less independent components:  $\Phi_0 = \Phi_0(T, u^r, \pi_\phi^\phi, \pi_\eta^\eta, \pi_{\text{bulk}})$ . Even if Eq. 2.36 are still non-linear partial differential equations, solving them is easier than solving the set in 2.34 in  $3 + 1$  dimensions: for this reason, this analysis will be limited to the study of zeroth-order terms in  $\epsilon$ , exploiting the approximate symmetry in  $\phi$  and  $\eta$  coordinates.

It was shown in [50] that the dissipative equations introduced in Eq. 2.23 and 2.24 are actually hyperbolic equations and can be cast into the form of Eq. 2.36: therefore, this represents the set of equations evolved within FluiduM. It is important to notice that this formalism can also be used when the set of equations is extended to further fields, as long as such extensions lead to quasi-linear, hyperbolic equations.

#### 2.2.4 Equation of State

As already introduced in Sec. 2.2.1, the Equation of State (EoS) is an equation relating thermodynamic variables, usually expressed by the pressure or the energy density as a function of temperature. The EoS is usually obtained from the system partition

function  $Z$ ,

$$P = \frac{T}{V} \left( \frac{\partial \ln Z}{\partial V} \right)_T. \quad (2.37)$$

In the case of the QGP, assuming that the net baryon chemical potential is approximately zero, the EoS can be computed by using IQCD techniques [51].

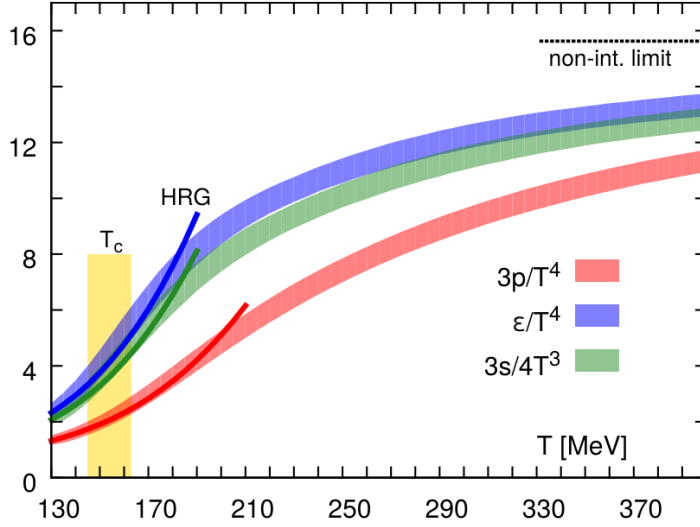
However, it is necessary to take into account that at lower temperatures, quarks and gluons recombine into hadrons: therefore, in this stage of the fireball evolution, the Equation of State becomes that of hadron resonance gas (HRG) [52]. Here, the single partition function  $Z_i$  for each hadron can be calculated using the grand canonical ensemble (GCE) formalism [53], where energy, momentum and charge number are not conserved locally. The hadron resonance gas EoS turns out to be very successful in describing particle abundances produced in heavy-ion collisions [54], as well as in estimating QCD transport coefficients [55].

Fig. 2.3 shows the behavior of the pressure, energy density, and entropy density as a function of temperature predicted by IQCD (bands) and by the HRG model (lines). The yellow vertical band represents the temperature at which IQCD predicts that the crossover occurs, at  $T_c = 154 \pm 9$  MeV. At low temperatures, the two models coincide, and HRG can be used as the Equation of State of the system. For higher temperature values, however, when quarks and gluons are the relevant degrees of freedom, the HRG approximation is no longer valid, and it is necessary to employ IQCD to infer the EoS of the system.

## 2.3 Hadronization and freeze-out

### 2.3.1 The Cooper-Frye procedure

If in the plasma the system is described using fluid fields degrees of freedom, after freeze-out the system must be described via particle distributions. This conversion is made possible via the Cooper-Frye procedure [56]. One of the main assumptions of the Cooper-Frye procedure is that the hadronization occurs fast enough to allow for the definition of a four-dimensional freeze-out hyper-surface  $\Sigma_\mu$ , which is assumed to be a surface of constant temperature, equal to the freeze-out temperature [56]. Moreover, the total momentum distribution is given by the summation of free independent particle distributions, which are still close to thermal equilibrium. Under these assumptions, the spectrum of hadron



**Figure 2.3:** Pressure, energy density, and entropy density as a function of the temperature, predicted by 1QCD (bands) and by the HRG (lines). The yellow vertical band represents the temperature at which the crossover occurs, at  $T_c = 154 \pm 9$  MeV. Figure taken from [51].

species  $a$  on the freeze-out hypersurface  $\Sigma_\mu$  can be expressed by,

$$E_{\mathbf{p}} \frac{dN_a}{d^3\mathbf{p}} = \frac{\nu_a}{(2\pi)^3} \int_{\Sigma} f_a p^\mu d\Sigma_\mu, \quad (2.38)$$

where  $f_a = f_a(p^\mu, T(x), u^\mu(x), \pi^{\mu\nu}(x), \pi_{\text{bulk}}(x))$  is the particle distribution function, and  $\nu_a$  the degeneracy factor of spin or polarization states.

On the freeze-out surface,  $f_a$  is given by an equilibrium contribution  $f_{a,\text{eq}}$ , which in the case of dissipative fluid dynamics must be corrected by additional corrections due to shear and bulk viscosity,

$$f_a = f_{a,\text{eq}} + \delta f_a^{\text{bulk}} + \delta f_a^{\text{shear}}. \quad (2.39)$$

Depending on the particle species, the equilibrium distribution function will be given either by a Bose-Einstein or by a Fermi-Dirac distribution,

$$f_{a,\text{eq}} = \frac{1}{e^{-\frac{p_\nu u^\nu + \mu_a}{T}} \pm 1}. \quad (2.40)$$

On the other hand, for  $\delta f_a^{\text{bulk}}$  and  $\delta f_a^{\text{shear}}$ , it is possible to use the common parametrization [57, 58],

$$\delta f_a^{\text{bulk}} = f_{a,\text{eq}}(1 \pm f_{a,\text{eq}}) \left[ \frac{\bar{E}_{\mathbf{p}}}{T} \left( \frac{1}{3} - c_s^2 \right) - \frac{m^2}{3T\bar{E}_{\mathbf{p}}} \right] \frac{\pi_{\text{bulk}}}{\zeta/\tau_{\text{bulk}}}, \quad (2.41)$$

$$\delta f_a^{\text{shear}} = f_{a,\text{eq}}(1 \pm f_{a,\text{eq}}) \frac{\pi_{\rho\nu} p^\rho p^\nu}{2(\epsilon + p)T^2}, \quad (2.42)$$

where  $c_s(T)$  is the speed of sound of the medium at the freeze-out,  $m$  is the mass of the primary resonance and  $\bar{E}_{\mathbf{p}}$  is the energy in the reference frame moving with velocity  $u^\mu$ . In the Cooper-Frye procedure, it is also necessary to calculate the freeze-out surface  $\Sigma_\mu$ , which in general depends on all four coordinates  $(\tau, r, \phi, \eta)$ . However, due to the symmetries of the background fields,  $\Sigma_\mu$  can be expressed as dependent on a single parameter in the  $\tau - r$  plane [59],

$$\tau = \tau(\alpha), \quad r = r(\alpha), \quad (2.43)$$

where without loss of generality  $\alpha \in [0, 1]$ . Starting from Eq. 2.32 and 2.33, it is possible to express the Cartesian coordinates as a function of  $\alpha$ ,

$$\begin{cases} t = \tau(\alpha) \cosh(\eta) \\ x = r(\alpha) \cos(\phi) \\ y = r(\alpha) \sin(\phi) \\ z = \tau(\alpha) \sinh(\eta). \end{cases} \quad (2.44)$$

From this expression, the infinitesimal element of hypersurface can be calculated as,

$$d\Sigma_\mu = (-dt, dx, dy, dz) = \tau(\alpha)r(\alpha) \left( \frac{\partial r}{\partial \alpha} \cosh \eta, \frac{\partial \tau}{\partial \alpha} \cos \phi, \frac{\partial \tau}{\partial \alpha} \sin \phi, \frac{\partial r}{\partial \alpha} \sinh \eta \right) d\alpha d\phi d\eta. \quad (2.45)$$

Similarly to what is done for the fields' evolution in Fluid $u$ M, the hadron spectrum after freeze-out can also be split into a background contribution, which is invariant under azimuthal and boost symmetries, and a non-symmetric part. For the background case, the freeze-out surface will be a 1D curve in the  $\tau - r$  plane, which can be parametrized as [60],

$$d\Sigma_\mu = \tau(\alpha)r(\alpha) \left( \frac{\partial r}{\partial \alpha}, -\frac{\partial \tau}{\partial \alpha}, 0, 0 \right) d\alpha d\phi d\eta. \quad (2.46)$$

Based on the same symmetry considerations, the background fluid 4-velocity is also given by the first two components only and can be written in terms of a *radial fluid rapidity*  $\bar{\chi}$ :

$$u^\mu = (\cosh(\bar{\chi}), \sinh(\bar{\chi}), 0, 0). \quad (2.47)$$

The particle momentum  $p_\mu$  at the freeze-out on the other hand will be expressed as a function of the momentum azimuthal angle  $\phi_P$  and of the momentum rapidity  $\eta_P$ ,

$$p_\mu = (-E, p_x, p_y, p_z) = (m_T \cosh \eta_P, p_T \cos \phi_P, p_T \sin \phi_P, m_T \sinh \eta_P), \quad (2.48)$$

where  $m_T$  represents the transverse mass  $m_T = \sqrt{m^2 + p_T^2}$ , and  $p_T = \sqrt{p_x^2 + p_y^2}$  the transverse momentum.

The explicit expression of  $d\Sigma_\mu$ , of  $u_\mu$ , and of  $p_\mu$  are of fundamental importance to evaluate the particles' freeze-out spectra, as shown in the next section.

### 2.3.2 Resonance decays

After the hadronization, unstable particles can decay into lighter products before being detected. As a matter of fact, from about 300 species of hadronic resonances produced in HIC, only a few long-lived hadrons, such as pions, kaons, and protons, reach the particle detectors and are directly observed. A particle decay is a probabilistic process, and the resultant particle spectrum from a decay cascade will fluctuate event by event. However, for a large number of initial resonances, it is possible to compute the spectrum of the final particle  $b$  by summing the spectra of each primary particle  $a$  which decays in  $b$ :

$$E_{\mathbf{p}} \frac{dN_b}{d^3\mathbf{p}} = \sum_a \int \frac{d^3\mathbf{q}}{(2\pi)^3 2E_{\mathbf{q}}} D_b^a(\mathbf{p}, \mathbf{q}) E_{\mathbf{q}} \frac{dN_a}{d^3\mathbf{q}}, \quad (2.49)$$

where  $D_b^a(\mathbf{p}, \mathbf{q})$ , is the *linear decay map*, the probability of particle  $a$  with momentum  $\mathbf{q}$  to decay to the particle  $b$  with momentum  $\mathbf{p}$ . In general  $D_b^a(\mathbf{p}, \mathbf{q})$  is usually calculated via Monte-Carlo generators [61, 62] or semi-analytic treatments [63]. Even if these calculations can be performed explicitly, due to large cascades of decays they are usually computationally expensive. For this reason, in this work, the publicly available code FastReso [60], which precomputes the decay maps, will be used to treat resonance decays. As shown in the previous section, the freeze-out surface can be expressed as a function of  $\alpha$ ,  $\phi$  and  $\eta$ . Exploiting the explicit formulation of the freeze-out surface, of the fluid 4-velocity and of the 4-momentum in 2.46 2.47 and 2.48 respectively, it can be shown

that the integral over the freeze-out surface reduces to,

$$\begin{aligned}
 E_{\mathbf{p}} \frac{dN_b}{d^3\mathbf{p}} &= \frac{dN_b}{2\pi p_T dp_T d\eta} = \frac{\nu_b}{(2\pi)^3} \int_0^1 d\alpha \tau(\alpha) r(\alpha) \\
 &\times \left\{ \frac{\partial r}{\partial \alpha} \left[ K_1^{\text{eq}} + \frac{\pi_\eta^\eta}{2(\epsilon+p)T^2} K_1^{\text{shear}} + \frac{\pi_\phi^\phi}{2(\epsilon+p)T^2} K_3^{\text{shear}} - \frac{\pi_{\text{bulk}}}{\zeta/\tau_{\text{bulk}}} K_1^{\text{bulk}} \right] \right. \\
 &\left. - \frac{\partial \tau}{\partial \alpha} \left[ K_2^{\text{eq}} + \frac{\pi_\eta^\eta}{2(\epsilon+p)T^2} K_2^{\text{shear}} + \frac{\pi_\phi^\phi}{2(\epsilon+p)T^2} K_4^{\text{shear}} - \frac{\pi_{\text{bulk}}}{\zeta/\tau_{\text{bulk}}} K_2^{\text{bulk}} \right] \right\}, \tag{2.50}
 \end{aligned}$$

where  $K_i^{\text{eq}}(p_T, u_r)$ ,  $K_i^{\text{shear}}(p_T, u_r)$ , and  $K_i^{\text{bulk}}(p_T, u_r)$  are rapidity and azimuthal angle integrated *decay kernels*. For an explicit expression of the integrated decay kernels, see [60].

## 3 Heavy-quark dynamics

The quark-gluon plasma created in heavy-ion collisions consists essentially of up, down, and strange quarks -the so-called *light quarks* -, of their respective antiquarks and of gluons. Even if these partons represent the majority of particles in the QGP, a minority of charm and bottom quarks exist in the medium as well. If on one hand light quarks have a mass of the order of MeV, on the other hand, the mass of the charm and bottom is 1.5 and 4.2 GeV respectively: as will be pointed out below, such mass values make heavy quarks (HQ) excellent probes of the interaction strength in the QGP, as well as of its transport properties.

First of all the heavy-quark mass is well above the typical temperature of the QGP,  $m_{\text{HQ}} \gg T$ : thus, HQ thermal production within the quark-gluon plasma is strongly suppressed [64], and charm and bottom quarks get predominantly produced via hard scattering at the very early stages of the collision. Moreover, due to their scarce abundance in the medium, the heavy-quark annihilation rate can be considered negligible within the QGP lifetime [65]. Therefore, the number of HQs is fixed by the initial production, and the particles undergo all the evolution stages of the QGP, from the pre-equilibrium phase to the hadronization. As it will be pointed out in Sec. 3.2.2, the conservation of the HQ number can be mathematically expressed by introducing a current  $N^\mu$  that is conserved throughout the evolution of the QGP.

The mass of heavy quarks exceeds the QCD scale  $\Lambda_{\text{QCD}}$  as well: therefore, the initial heavy-quark production can be described using perturbative QCD schemes, which unveil the non-thermal production of HQs, as discussed in Sec. 3.2.1.

### 3.1 Heavy quarks and transport models

#### 3.1.1 The Boltzmann equation

In a system constituted of many classical particles, the distribution function  $f(\mathbf{x}, \mathbf{p}, t)$  represents the probability of finding a particle in the infinitesimal volume  $d^3x$  centered

in  $\mathbf{x}$  space coordinate, and in the volume  $d^3p$  centered in  $\mathbf{p}$  momentum space, at a given time  $t$ . In thermal equilibrium, the distribution function is represented by the Fermi-Dirac or by the Bose-Einstein distribution, depending on the statistical nature of the system. However, in the presence of a perturbation such as external forces or multiple collisions, the distribution function can deviate from its thermal equilibrium expression. Low-momentum heavy quarks (3–4 GeV) mainly interact via elastic scatterings, and the typical momentum exchange in the interactions of HQs with the medium is small compared to their mass. Therefore, heavy quarks undergo Brownian motion in the medium characterized by many small-momentum kicks. The evolution in phase space of the heavy-quark distribution function  $f_Q(\mathbf{x}, \mathbf{p}, t)$  accounting for this collision effect, can be expressed by exploiting the Boltzmann equation [66, 67],

$$\left( \frac{\partial}{\partial t} + \mathbf{v} \frac{\partial}{\partial \mathbf{x}} + \mathbf{F} \frac{\partial}{\partial \mathbf{p}} \right) f_Q(\mathbf{x}, \mathbf{p}, t) = \left( \frac{\partial f_Q}{\partial t} \right)_{\text{collision}}, \quad (3.1)$$

where  $\mathbf{F}$  represents external forces acting on the heavy quarks, such as the interaction with large concentrations of color charge. Neglecting all interactions with other heavy quarks and with background color fields, it is possible to set  $\mathbf{F} = 0$ . Moreover, assuming that the plasma is uniform, the distribution function is  $x$ -independent, thus Eq. 3.1 reduces to,

$$\frac{\partial f_Q(\mathbf{p}, t)}{\partial t} = \left( \frac{\partial f_Q}{\partial t} \right)_{\text{collision}} = C[f_Q], \quad (3.2)$$

where  $C[f_Q]$  represents the collision integral, which accounts for sudden momentum exchanges due to scattering processes. Considering the scattering between a light parton  $i$  with initial and final momentum respectively  $\mathbf{p}_i$  and  $\mathbf{p}'_i$ , and a heavy quark  $Q$  with final and initial momentum  $\mathbf{p}_Q$  and  $\mathbf{p}'_Q$ , neglecting quantum effects, the collision integral can be expressed as,

$$C[f_Q] = \int d\mathbf{p}'_Q d\mathbf{p}_i d\mathbf{p}'_i [w(\mathbf{p}'_Q, \mathbf{p}'_i | \mathbf{p}_Q, \mathbf{p}_i) f_Q(\mathbf{p}'_Q) f_i(\mathbf{p}'_i) - w(\mathbf{p}_Q, \mathbf{p}_i | \mathbf{p}'_Q, \mathbf{p}'_i) f_Q(\mathbf{p}_Q) f_i(\mathbf{p}_i)], \quad (3.3)$$

where  $w$  represents the scattering rate. The first term of the integral accounts for processes in which the heavy quark gains momentum, while the second one for momentum losses.

Assuming that the scattering processes are symmetric under time-reversal transforma-

tions,  $w(\mathbf{p}'_Q, \mathbf{p}'_i | \mathbf{p}_Q, \mathbf{p}_i) = w(\mathbf{p}_Q, \mathbf{p}_i | \mathbf{p}'_Q, \mathbf{p}'_i)$ , the collision integral simplifies to,

$$C[f_Q] = \int d\mathbf{p}'_Q d\mathbf{p}_i d\mathbf{p}'_i w(\mathbf{p}'_Q, \mathbf{p}'_i | \mathbf{p}_Q, \mathbf{p}_i) [f_Q(\mathbf{p}'_Q) f_i(\mathbf{p}'_i) - f_Q(\mathbf{p}_Q) f_i(\mathbf{p}_i)]. \quad (3.4)$$

The stationary solutions for heavy quarks are found when their distribution function is constant in time, or in other words when its time derivative is equal to zero. From Eq. 3.2, this condition translates into asking that the collision integral cancels out, thus,

$$f_Q(\mathbf{p}'_Q) f_i(\mathbf{p}'_i) = f_Q(\mathbf{p}_Q) f_i(\mathbf{p}_i). \quad (3.5)$$

This relation between final and initial momentum distributions entails that both  $f_Q$  and  $f_i$  must be expressed in terms of exponential,

$$f_Q(\mathbf{p}_Q) = \exp\left(-\frac{E_{p_Q}}{T}\right) \quad f_i(\mathbf{p}_i) = \exp\left(-\frac{E_{p_i}}{T}\right). \quad (3.6)$$

Thus, the Boltzmann transport equation implies that the heavy-quarks distribution function relaxes to a thermal distribution at temperature  $T$ , which is the same temperature as the surrounding medium.

### 3.1.2 The Fokker-Planck equation

The Fokker-Planck equation is an approximation of the Boltzmann equation in the case of multiple soft scatterings. An elastic collision involves a momentum exchange  $\mathbf{k}$  between the two colliding particles. It is possible to work under the assumption that the HQ gains in momentum,  $\mathbf{k} = \mathbf{p}'_Q - \mathbf{p}_Q$ , while the light parton loses the same amount of momentum, thus  $\mathbf{k} = \mathbf{p}_i - \mathbf{p}'_i$ . Expressing the collision integral as a function of the momentum exchange  $\mathbf{k}$ , the collision integral in Eq. 3.4 can be re-written in the simplified form,

$$C[f_Q] = \int d\mathbf{k} w(\mathbf{p} + \mathbf{k} | \mathbf{p}) [f_Q(\mathbf{p} + \mathbf{k}) - f_Q(\mathbf{p})], \quad (3.7)$$

where for simplicity of notation  $\mathbf{p}_Q \equiv \mathbf{p}$ , and  $w$  encodes also the dependence on the distribution of light partons. In the approximation of small momentum exchange, it is possible to Taylor-expand the product  $w(\mathbf{p} + \mathbf{k} | \mathbf{p}) f_Q(\mathbf{p} + \mathbf{k})$ ,

$$w(\mathbf{p} + \mathbf{k} | \mathbf{p}) f_Q(\mathbf{p} + \mathbf{k}) \sim w(\mathbf{p} | \mathbf{p}) f_Q(\mathbf{p}) + k_i \frac{\partial}{\partial p_i} (w f_Q) + \frac{1}{2} k_i k_j \frac{\partial^2}{\partial p_i \partial p_j} (w f_Q). \quad (3.8)$$

Thus, using this approximation to calculate the collision integral, and substituting it into Eq. 3.2, the final expression of the Fokker-Planck equation reads,

$$\frac{\partial f_Q(t, \mathbf{p})}{\partial t} = \frac{\partial}{\partial p^i} \left[ A^i(\mathbf{p}) f_Q(t, \mathbf{p}) + \frac{\partial}{\partial p^j} B^{ij} f_Q(t, \mathbf{p}) \right], \quad (3.9)$$

where the two tensors  $A^i$  and  $B^{ij}$ , referred to as *kernels*, describe the interaction between heavy quarks and the medium, and are defined as,

$$A^i(\mathbf{p}) = \int d\mathbf{k} k^i w(\mathbf{p} + \mathbf{k}|\mathbf{p}), \quad (3.10)$$

$$B^{ij}(\mathbf{p}) = \frac{1}{2} \int d\mathbf{k} k^i k^j w(\mathbf{p} + \mathbf{k}|\mathbf{p}). \quad (3.11)$$

Assuming an isotropic medium, the kernels can be further simplified [67],

$$A^i(\mathbf{p}) = A(p) p^i, \quad (3.12)$$

$$B^{ij}(\mathbf{p}) = (\delta^{ij} - \hat{p}^i \hat{p}^j) B_0(p) + \hat{p}^i \hat{p}^j B_1(p), \quad (3.13)$$

where  $\hat{p}^i \equiv \frac{p^i}{|p|}$  represents a unit vector in  $p^i$  direction. The coefficient  $A(p)$  is called the *friction coefficient* whereas  $B_0(p)$  and  $B_1(p)$  represent the *momentum diffusion coefficients* along the directions perpendicular and parallel to the heavy-quark velocity, respectively.

As done in the case of the Boltzmann equation, it is now possible to look for stationary solutions, which translates into assuming that heavy quarks relax to a thermal distribution. To satisfy this condition, the right-hand side of Eq. 3.9 must vanish, thus,

$$A^i(\mathbf{p}) f_Q(t, \mathbf{p}) = - \frac{\partial}{\partial p^j} [B^{ij} f_Q(t, \mathbf{p})]. \quad (3.14)$$

Since the heavy quarks are assumed to be in thermal equilibrium, their distribution function is expressed as the exponential distribution in Eq. 3.6. Therefore, plugging  $f_Q(\mathbf{p}_Q)$  in 3.14 and exploiting the tensor structure of the transport coefficients,

$$A(p) p^i = \frac{B_1(p)}{TE_p} p^i - \frac{\partial}{\partial p^j} [\delta^{ij} B_0(p) + \hat{p}^i \hat{p}^j (B_1(p) - B_0(p))]. \quad (3.15)$$

This equation entails a unique relation between the three transport coefficients, the so-called *Einstein fluctuation-dissipation* (EFD) relation [68],

$$A = \frac{B_1}{TE} - \frac{1}{p^2} \left[ 2(B_1 - B_0) + p \frac{\partial B_1}{\partial p} \right]. \quad (3.16)$$

It is important to underline that both Boltzmann and Fokker-Planck equations were presented here using classical mechanics. A more accurate estimate for the transport coefficients can be provided by implementing quantum corrections -as Pauli blocking- in the Boltzmann equation and in the subsequent Fokker-Planck equation [69].

### 3.1.3 The spatial diffusion coefficient

To better understand the physical meaning of the transport coefficients, it is possible to start neglecting their momentum dependence, and consider them as two constant quantities,

$$A(p) \equiv \gamma, \quad (3.17)$$

$$B_0(p) = B_1(p) \equiv D. \quad (3.18)$$

In this simplified scenario, the Fokker-Planck equation in 3.9 will depend only on the constant  $\gamma$  and  $D$ , reducing to,

$$\frac{\partial f_Q(t, \mathbf{p})}{\partial t} = \gamma \frac{\partial}{\partial p^i} [p^i f_Q(t, \mathbf{p})] + D \delta^{ij} \frac{\partial^2 f_Q(t, \mathbf{p})}{\partial p^i \partial p^j}. \quad (3.19)$$

Setting as an initial condition that the heavy-quark distribution function is given by a delta function centered on the initial momentum  $\mathbf{p}_0$ ,  $f_Q(t, \mathbf{p}) = \delta(\mathbf{p} - \mathbf{p}_0)$ , it can be shown [67] that the solution of 3.19 is given in terms of an exponential,

$$f_Q(t, \mathbf{p}) \propto \exp \left( -\frac{\gamma}{2D} \frac{(p - p_0 e^{-\gamma t})^2}{1 - e^{-2\gamma t}} \right), \quad (3.20)$$

which, in the limit of infinite time  $t \rightarrow \infty$ , reduces to,

$$f_Q(t, \mathbf{p}) \propto \exp \left( -\frac{\gamma}{2D} p^2 \right) = \exp \left( -\frac{\gamma M}{D} \frac{p^2}{2M} \right), \quad (3.21)$$

where  $M$  is the mass of the heavy quark. Thus, for asymptotic values of  $t$ ,  $f_Q(t, \mathbf{p})$  does not depend on the initial momentum and relaxes to a thermal distribution.

Moreover, comparing Eq. 3.21 with the Boltzmann expression in Eq. 3.6, and knowing that  $E_{pQ} = \frac{p^2}{2M}$ , a relation between  $\gamma$  and  $D$  can be found,

$$D = \gamma MT, \quad (3.22)$$

which represents the non-relativistic Einstein fluctuation-dissipation relation [68].

From Eq. 3.21, it is also possible to calculate the first moment of the equilibrium distribution,

$$\langle \mathbf{p}(t) \rangle = \mathbf{p}_0 e^{-\gamma t}, \quad (3.23)$$

meaning that with the increase of time,  $\gamma$  leads the average momentum of the heavy quark to vanish: for this reason, as stated before,  $A(p) \equiv \gamma$  is referred to as the *friction coefficient*. Similarly, it is possible to calculate the second moment of the momentum distribution,

$$\langle \mathbf{p}^2(t) \rangle - \langle \mathbf{p}(t) \rangle^2 = \frac{3D}{\gamma} (1 - e^{-2\gamma t}). \quad (3.24)$$

Therefore, the diffusion coefficient is responsible for the momentum broadening of the distribution.

Under certain reasonable assumptions about the diffusion process [70], the diffusion in momentum space leads to diffusion in position, which can be expressed as,

$$\langle x^2 \rangle - \langle x \rangle^2 = \frac{6D}{M^2 \gamma^2} t \equiv 6D_s t. \quad (3.25)$$

The coefficient  $D_s$ , usually referred to as the *spatial diffusion coefficient*, is identified as the asymptotic mean squared displacement of an ensemble of heavy quarks initially placed at the origin of the fireball. In particular, the diffusion coefficient characterizes the long-wavelength properties of the transport of the heavy quark quantum number through QCD matter, and, as long as the dynamics is non-relativistic, can also be expressed through the zeroth-momentum value of the drag coefficient,

$$D_s = \frac{T}{A(p=0)M}. \quad (3.26)$$

Being able to summarize the heavy-quark coupling with the medium, the spatial diffusion coefficient is of particular interest in phenomenological studies.

## 3.2 The hydrodynamic approach to heavy quarks

### 3.2.1 Heavy-flavour elliptic flow

A particle species is defined to be in *chemical equilibrium* when its multiplicity can be described by a distribution function dependent on a local chemical potential  $\mu(x)$ . Perturbative calculations [71] demonstrate that in the hard scattering heavy quarks are not produced in chemical equilibrium. Moreover, since their number density is much smaller with respect to the one of the light quarks, they presumably remain out of chemical equilibrium for the entire evolution of the fireball. As a matter of fact, it was shown in [65] that, to reach chemical equilibrium with the fireball, heavy quarks would need to interact with the medium for about 60 fm: this time is well above the 10 fm average lifetime of the QGP [28].

On the other hand, a particle species is said to be in *kinetic equilibrium* when a Boltzmann-like distribution can describe its distribution function in the classical case, thus dependent on a local temperature  $T(x)$ . Since heavy quarks are produced via hard scattering, their initial distribution function is expected to be far from local kinetic equilibrium [71].

Notice that, if not explicitly stated otherwise, the terms *thermal* and *kinetic* equilibrium will be used as synonyms in this thesis.

As stated in Sec. 1.4.1, one of the most striking evidence that QGP behaves as a strong interacting fluid comes from the observation of the elliptic flow  $v_2$ . In particular, the measurement of  $v_2$  in heavy-flavor hadrons at low  $p_T$  can help quantify if and to which extent heavy quarks participate in the collective motion of the medium. Precise measurements of heavy-flavor  $v_n$  coefficients can serve as a tool to constrain the values of transport coefficients as  $D_s$ . Studies on the heavy-hadron elliptic flow were performed in the past decade at the LHC [72] at TeV energies. The plot presented in Fig. 3.1 shows that  $D$  mesons and  $J/\psi$  exhibit a non-negligible elliptic flow, which, for the case of  $D$  mesons, is even comparable with the  $v_2$  of pions. This result translates into saying that the charm quarks composing the charmed hadrons participate in the collective behavior of the medium and thus presumably reach kinetic equilibrium within the QGP.

Heavy-quark propagation within quark-gluon plasma is traditionally described using a Brownian approach [73]. However, the presence of the elliptic flow represents a strong hint that charm quarks can be considered as a part of the medium itself: thus, a new fluid-dynamic approach to study their dynamics in the QGP, introduced for the first time in [69], will be summarized in the next sections.

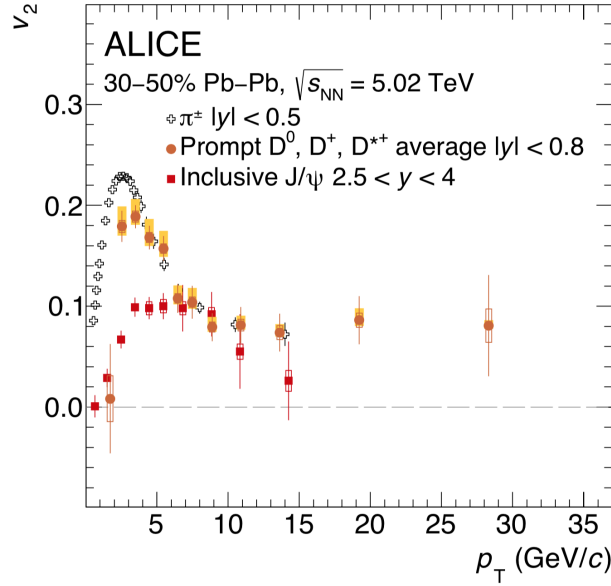


**Figure 3.1:** Elliptic flow of  $D$  mesons and  $J/\psi$  as a function of  $p_T$ , measured at the LHC by ALICE. For comparison, the elliptic flow of pions is shown as well. Figure taken from [72].

### 3.2.2 Heavy-quark conserved current

As already introduced in the present chapter, the number of charm and bottom quarks is conserved throughout the evolution of the QGP. Even if the conservation of the sum of heavy quark and antiquark pairs  $Q\bar{Q}$  does not represent an exact symmetry of QCD, it is possible to associate to it a conserved current,

$$N_+^\mu \equiv \frac{N_Q^\mu + N_{\bar{Q}}^\mu}{2}. \quad (3.27)$$

In general, quarks can interact both via strong and electroweak interaction. However, due to the longer time scale, electroweak processes can be considered negligible within the QGP lifetime. The only relevant interaction within the fireball is thus strong interaction, which conserves the quark's flavor. For this reason, the net number of HQ gets conserved as well in the QGP,

$$N_-^\mu \equiv N_Q^\mu - N_{\bar{Q}}^\mu. \quad (3.28)$$

Thus,  $N_+^\mu$  is conserved *effectively*, whereas  $N_-^\mu$ , which is associated with a QCD symmetry, is conserved *exactly*. Since the initial hard scattering produces the same number of

quarks and antiquarks, it is at first approximation possible to neglect any local imbalance between quark and antiquark developing during the QGP evolution: for this reason, in this analysis  $N_-^\mu = 0$ .

Following the work in [74], it is possible to express a general particle conserved current in terms of the fluid 4-velocity of the system. In the case of the heavy-quark current  $N_Q^\mu$ , this relation reads as,

$$N_Q^\mu = n_Q u^\mu + \nu_Q^\mu, \quad (3.29)$$

where  $u^\mu$  represents the fluid 4-velocity,  $n_Q$  is the heavy-quark density, and  $\nu_Q^\mu$  is the diffusion current, which is orthogonal to the fluid velocity:  $u_\mu \nu_Q^\mu = 0$ . It is important to notice that Eq. 3.29, as well as all the relations shown in this discussion also hold for the case of heavy antiquarks. Asking for the conservation of the number of HQ during the evolution of the QGP thus translates into asking that the 4-derivative of the conserved current vanishes,

$$\partial_\mu N_Q^\mu = \partial_\mu (n_Q u^\mu + \nu_Q^\mu) = 0. \quad (3.30)$$

### 3.2.3 Relation between hydrodynamics and distribution function

As introduced before, heavy quarks are not produced in chemical equilibrium. Therefore, an additional chemical potential  $\mu_Q^{\text{ave}}(x) = \mu_Q(x) + \mu_{\bar{Q}}(x)$ , associated with the HQ average number, must be included in the distribution function to account for the deviation of the HQ from full chemical equilibrium. Since  $\mu_Q^{\text{ave}}(x)$  is the same for quarks and antiquarks,  $\mu_Q = \frac{\mu_Q^{\text{ave}}(x)}{2}$ . Thus, at local kinetic equilibrium, the distribution function of heavy quarks  $f_k^Q$  can be expressed as a Boltzmann distribution with chemical potential  $\mu_Q(x)$ ,

$$f_k^Q = \exp\left(\frac{-E + \mu_Q(x)}{T(x)}\right) = \gamma_Q \cdot \exp\left(-\frac{E}{T(x)}\right), \quad (3.31)$$

where the *fugacity factor*  $\gamma_Q = e^{\mu_Q(x)/T(x)}$  is introduced. It is important to underline that this expression for  $f_k^Q$  is valid when the baryon chemical potential of the system is negligible  $\mu_B(x) \sim 0$ , as it is at LHC energies. Otherwise, an additional term  $\mu_B(x)$  should be added to  $\mu_Q(x)$  in the exponential.

In kinetic theory, the energy-momentum tensor  $T^{\mu\nu}$  and the conserved particle current can be expressed as moments of the single-particle distribution function. In the specific case of this analysis, the particle-conserved current corresponds to the heavy-quark current  $N_Q^\mu$ , and the distribution function represents the heavy-quark distribution function

$f_k^Q$ . Being  $k^\mu$  the heavy-quark 4-momentum, it is possible to write [74],

$$T^{\mu\nu} = \langle k^\mu k^\nu \rangle, \quad (3.32)$$

$$N_Q^\mu = \langle k^\mu \rangle, \quad (3.33)$$

where the angle brackets operator is defined as,

$$\langle \dots \rangle \equiv \int dK(\dots) f_k^Q. \quad (3.34)$$

Here,  $\int dK \equiv \int \nu \frac{d^3k}{(2\pi)^3 k^0}$  represents the Lorentz-invariant momentum-space volume, with  $\nu$  the degeneracy factor accounting for internal degrees of freedom.

It is now possible to decompose  $T^{\mu\nu}$  and  $N_Q^\mu$  as a function of the fluid 4-velocity  $u^\mu$ . To do so, the 4-velocity can be defined within the Landau frame [43] where  $u^\mu$  is the time-like eigenvector of the energy-momentum tensor, with eigenvalue the energy density of the system  $\epsilon$ ,

$$T^{\mu\nu} u_\mu = \epsilon u^\nu. \quad (3.35)$$

After defining  $u^\mu$  in this specific reference frame, the momentum of the particle  $k^\mu$  can be split into two contributions, one parallel and one orthogonal to  $u^\mu$ ,

$$k^\mu = E_{\mathbf{k}} u^\mu + k^{\langle\mu\rangle}, \quad (3.36)$$

where by definition  $E_{\mathbf{k}} \equiv u_\mu k^\mu$  and we use the notation  $A^{\langle\mu\rangle} \equiv \Delta_\nu^\mu A^\nu$ , with  $\Delta_\nu^\mu = g_\nu^\mu - u^\mu u_\nu$  the projection operator onto the 3-space orthogonal to  $u^\mu$ .

Thus, plugging this momentum decomposition into Eq. 3.32 and into 3.33 the energy-momentum tensor and the HQ conserved current can be expressed as,

$$T^{\mu\nu} = \langle E_{\mathbf{k}}^2 \rangle u^\mu u^\nu - \frac{1}{3} \langle \Delta^{\mu\nu} k_\mu k_\nu \rangle \Delta^{\mu\nu} + \langle k^{\langle\mu} k^{\nu\rangle} \rangle, \quad (3.37)$$

$$N_Q^\mu = \langle E_{\mathbf{k}} \rangle u^\mu + \langle k^{\langle\mu\rangle} \rangle. \quad (3.38)$$

Comparing these equations with the general expression of  $T^{\mu\nu}$  and of  $N^\mu$  in 2.21 and in 2.22 respectively, several relations between the heavy-quark density  $n_Q$ , the HQ diffusion current  $\nu_Q^\mu$ , the medium energy density  $\epsilon$ , the shear-stress tensor  $\pi^{\mu\nu}$ , and the sum of thermodynamic and viscous pressure  $P + \pi_{\text{bulk}}$ , with the distribution function can be

inferred,

$$n_Q \equiv \langle E_{\mathbf{k}} \rangle, \quad \nu_Q^\mu \equiv \langle k^{\langle \mu} \rangle, \quad \epsilon \equiv \langle E_{\mathbf{k}}^2 \rangle, \quad \pi^{\mu\nu} \equiv \langle k^{\langle \mu} k^{\nu \rangle} \rangle, \quad P + \pi_{\text{bulk}} \equiv -\frac{1}{3} \langle \Delta^{\mu\nu} k_\mu k_\nu \rangle, \quad (3.39)$$

where we employ the notation  $A^{\langle \mu\nu \rangle} \equiv \Delta_{\alpha\beta}^{\mu\nu} A^{\alpha\beta}$  and  $\Delta_{\alpha\beta}^{\mu\nu} \equiv \frac{1}{2} \left[ \Delta_\alpha^\mu \Delta_\beta^\nu + \Delta_\alpha^\nu \Delta_\beta^\mu - \frac{2}{3} \Delta^{\mu\nu} \Delta_{\alpha\beta} \right]$  is a projector onto that part of a rank-2 tensor, which is symmetric, orthogonal to  $u^\mu$ , and traceless. Thus, the equations in 3.39 encode the relation between fluid-dynamics quantities and the heavy-quark distribution function.

### 3.2.4 Heavy-quark transport coefficients

Since the total number of heavy quark-antiquark pairs is conserved, it is possible to define a density related to them  $n_+ \equiv \frac{n_Q + n_{\bar{Q}}}{2}$  as well as a diffusion current  $\nu_+ \equiv \frac{\nu_Q + \nu_{\bar{Q}}}{2}$ . Taking as a reference the Israel-Stewart theory introduced in Sec. 2.2.2, the equation of motion for the diffusion current of heavy quark-antiquark pairs can be written using the same mathematical expression of Eq. 2.31,

$$\tau_n \Delta_\rho^\mu u^\sigma \partial_\sigma \nu_+^\rho + \nu_+^\mu = \kappa_n \Delta^{\mu\nu} \nabla_\nu \left( \frac{\mu_Q}{T} \right), \quad (3.40)$$

This is a relaxation-type equation in which terms of higher order in the gradients are neglected, and it is tuned by the heavy-quark diffusion coefficient  $\kappa_n$  and the heavy-quark relaxation time  $\tau_n$ , which represents the time scale needed by the HQ to relax to at least kinetic equilibrium. When  $\tau \gg \tau_n$ , the diffusion current  $\nu_+^\mu$  relaxes to its Navier-Stokes limit  $\nu_+^\mu = \kappa_n \nabla^\mu (\mu_Q/T)$  as in Eq. 2.28.

In order to understand the role of the heavy-quark transport coefficients, it is possible to start from the Fokker-Planck equation for the HQ distribution function  $f_k^Q$ , and integrate subsequent moments of it. For simplicity, we consider the Fokker-Planck equation for a homogeneous fluid at rest,

$$k^\mu \partial_\mu f_k^Q = k^0 \frac{\partial}{\partial k^i} \left\{ A^i f_k^Q + \frac{\partial}{\partial k^j} \left[ B^{ij} f_k^Q \right] \right\}. \quad (3.41)$$

Knowing the relation between the fluid dynamic quantities and  $f_k^Q$  in 3.39, it is possible to verify that the zeroth moment of Eq. 3.41 reduces to the continuity equation, which in the fluid rest frame can be expressed as,

$$\partial_t n_+ + \partial_i \nu_+^i = 0. \quad (3.42)$$

On the other hand, the first moment of the Fokker-Planck equation reduces to,

$$\partial_t \int dK k^0 k^l f_k^Q + \partial_i \int dK k^l k^i f_k^Q = \int dK k^l k^0 \frac{\partial}{\partial k^i} \left\{ A^i f_k^Q + \frac{\partial}{\partial k^j} [B^{ij} f_k^Q] \right\}. \quad (3.43)$$

It can be shown that Eq. 3.43 leads to an equation of motion for  $\nu_+^\mu$  in the fluid rest frame. The full calculation is reported in [69], where the method of irreducible moments [74] is exploited. Moreover in the calculation, the moments with a rank higher than 2 are neglected, considering as only relevant quantities the heavy-quark bulk pressure, diffusion current, and shear-stress tensor. The equation of motion for the diffusion current obtained from this method reads,

$$\frac{TI_{31}}{DP_0} \partial_t \nu_+^\mu + \nu_+^\mu = \frac{T^2 n_+}{D} \partial_\mu \left( \frac{\mu_Q}{T} \right), \quad (3.44)$$

where  $I_{31} = \frac{1}{3} \langle k^0 k^2 \rangle$ ,  $P_0$  represents the heavy-quark contribution to the pressure [69] and  $T$  the temperature of the system.

Comparing Eq. 3.40 with 3.44 it is possible to identify the relaxation time and diffusion coefficient as,

$$\tau_n = \frac{TI_{31}}{DP_0}, \quad (3.45)$$

$$\kappa_n = \frac{T^2 n_+}{D} \equiv D_s n_+. \quad (3.46)$$

Thus, the heavy-quark transport coefficient  $\tau_n$  and  $\kappa_n$  are both directly proportional to the spatial diffusion coefficient  $D_s$ : this is a fundamental result and will be exploited later on in the analysis.

# 4 Heavy quarks at RHIC

## 4.1 Motivation

The non-negligible value of the elliptic flow measured at the LHC strongly supports that, at TeV energies, charm quarks can be considered part of the QGP medium, and therefore described via a hydrodynamic model. Recent studies showed that this approach accurately describes the charmed-hadron yields and the  $p_T$ -differential spectra measured in Pb – Pb collisions at  $\sqrt{s_{NN}} = 5.02$  TeV [75].

However, one wonders if the hydrodynamic description of heavy quarks still holds for lower-energy systems, which produce a lower-temperature QGP state. Being colder, the fireball requires less time to reach the freeze-out temperature, meaning that heavy quarks have less time to interact with the medium, and to possibly reach thermalization. Moreover, due to the smaller number of binary nucleon-nucleon collisions and the smaller value of heavy-quark production cross-section, the number of HQ pairs in the QGP decreases significantly.

Several measurements on heavy-flavor elliptic flow have been performed at RHIC [76, 77], in Au – Au collisions at  $\sqrt{s_{NN}} = 200$  GeV. In Fig. 4.1, the trend of the elliptic flow as a function of  $p_T$  for  $D^0$  meson and for several light hadrons is reported. Here, a clear mass ordering for  $p_T < 2$  GeV including  $D^0$  mesons is observed. For  $p_T > 2$  GeV, the  $D^0$  meson  $v_2$  follows that of other light mesons indicating a significant charm quark flow. Since  $D^0$  meson contains a charm and an anti-up quark, one may argue that this result is due to the presence of the light quark which took part in the collective motion of the QGP and thus gained flow. However, the non-zero elliptic flow of  $D^0$  still raises the question about the possible heavy-quark thermalization at RHIC.

Studies at RHIC [77] demonstrated that  $J/\psi$  elliptic flow is consistent with zero within statistical errors (Figure 4.2). However, it is necessary to consider that  $J/\psi$  meson can be either produced from direct pQCD processes (the so-called *primordial*  $J/\psi$ ) or from  $c\bar{c}$  recombination. In the first mechanism process,  $J/\psi$  meson experiences the whole evolution of a heavy-ion collision in a colorless stage: it does not participate in the

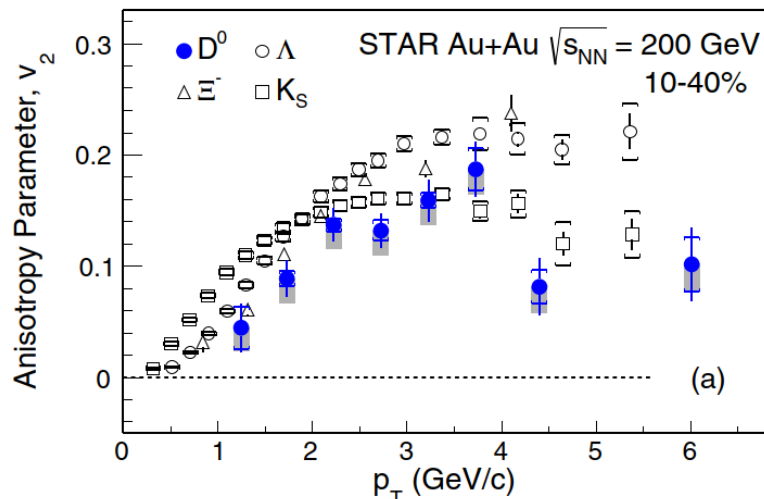


**Figure 4.1:** Elliptic flow of  $D^0$  meson as a function of  $p_T$ , measured at RHIC, STAR. For comparison, the elliptic flow of other light-flavor hadrons is shown as well. Figure taken from [76].

collective motion of the QGP, thus gaining limited azimuthal anisotropy. On the other hand, the  $J/\psi$  produced from the recombination of thermalized charm quarks inherits the flow of charm quarks, exhibiting considerable  $v_2$ . Since the number of  $J/\psi$  mesons produced at RHIC top energies is very small [78], this result can be explained assuming that the measured  $J/\psi$  are mostly coming from direct pQCD processes. Moreover, due to the limited precision of the experimental results, it is difficult to draw any strong conclusion and exclude that charm quarks are thermalized in the medium.

Heavy-flavor dynamics at RHIC still leaves many open questions, serving as a starting point for the present work and motivating us to a phenomenological study of heavy-quark thermalization at lower collision energies. This work focuses mainly on the dynamics of charm quarks: thus, if not stated otherwise, in the next sections the terms *charm quark* and *heavy quark* will be used interchangeably.

## 4.2 Initial condition modeling

The HQ hydrodynamic approach was already successfully applied at LHC energies [75]: it is now possible to try to extend the same formalism at RHIC collision energies. To do so, it is essential to first model the initial state of the QGP using T<sub>R</sub>ENTo model. T<sub>R</sub>ENTo takes as input several parameters, whose values are not estimated in the present analysis,

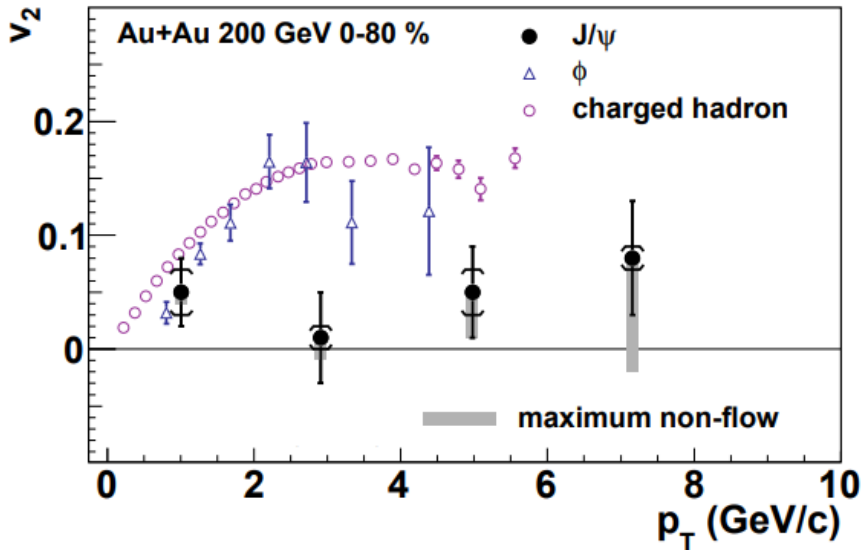


**Figure 4.2:** Elliptic flow of  $J/\psi$  meson as a function of  $p_T$ , measured at RHIC, STAR, compared to charged hadrons  $v_2$ . Figure taken from [77].

but rather taken from the literature [79]. In particular, the reduced thickness parameter is set to  $p = 0$ , the nucleon width to  $w = 0.5$  fm, and the fluctuation parameter to  $k = 1$ . Moreover, in `TRENTo` it is possible to tune the number of constituents  $m$  inside the nucleons. Thus, the nucleon is considered as divided into  $m$  Gaussians, each of width  $v$ . In this analysis, the number of constituents and their width are  $m = 4$  and  $v = 0.4$  fm respectively.

The Au ions are sampled using a Woods–Saxon distribution, with nuclear radius  $R = 6.38$  fm, and skin depth  $a_0 = 0.535$  fm. For Woods-Saxon nuclei, `TRENTo` sets a minimum nucleon-nucleon distance, which in the current analysis is  $d = 0.75$  fm.

The inelastic nucleon-nucleon cross-section  $\sigma_{\text{inel}}^{\text{NN}}$  at  $\sqrt{s_{\text{NN}}} = 200$  GeV is taken from the PHENIX collaboration [80],  $\sigma_{\text{inel}}^{\text{NN}} = 4.23$  fm<sup>2</sup>.

In Table 4.1 an overview of the `TRENTo` parameters used to generate  $10^6$  collision events is reported.

### 4.2.1 Initial temperature

As introduced in 2.1.2, `TRENTo` output  $T_R(x, y)$  can be considered as an entropy density profile up to a normalization constant. Moreover, the integral of  $T_R(x, y)$  is approximately proportional to the multiplicity of each collision: since the centrality class is also

Parameter	Value
Reduced thickness parameter $p$	0
Nucleon width $w$	0.5 fm
Fluctuation parameter $k$	1
Constituents number $m$	4
Constituents width $v$	0.4 fm
Nucleon minimum distance $d$	0.75 fm
Nucleon-nucleon cross-section $\sigma_{\text{inel}}^{\text{NN}}$	4.23 fm <sup>2</sup>

**Table 4.1:** TRENTo parameters used as input of the current analysis.

monotonically related to the multiplicity, the value of  $\int T_R(x, y) dx dy$  is first used to divide the events into centrality classes. Afterward, all the profiles belonging to a given centrality class are centered on their center of mass and then averaged to  $\langle T_R(x, y) \rangle$ . This averaging procedure is possible because FluiduM is not an event-by-event simulation, but rather evolves the mean fields of the system.

For a large number of events, the average entropy densities are azimuthally symmetric: thus, a coordinate transformation is performed  $\langle T_R(x, y) \rangle \rightarrow \langle T_R(r, \phi) \rangle$  and the polar coordinate  $\phi$  is integrated out. Via this procedure, the averaged transverse density profile is thus computed  $\langle T_R(r) \rangle$ .

The  $\langle T_R(r) \rangle$  profile and the entropy density profile  $s(r)$  are equal up to a normalization constant Norm. Defining  $\tau_0$  as the starting time at which the fluid dynamic description becomes valid, it is possible to write,

$$s(r) = \frac{\text{Norm}}{\tau_0} \langle T_R(r) \rangle. \quad (4.1)$$

To account for the longitudinal expansion at early times, it is necessary to divide the normalization constant by  $\tau_0$ . The value of Norm is inferred from the pion multiplicity measured by the PHENIX collaboration [81]. Fig. 4.3 shows the trend of  $\langle T_R(r) \rangle$  as a function of the radius  $r$  for five different centrality classes. Since  $\langle T_R(r) \rangle$  and  $s(r)$  are directly proportional, the plot can be physically interpreted in terms of entropy deposition. The entropy deposit results maximum at the center of the fireball and smoothly decreases to zero with  $r$ . Moreover, as intuitively expected, more central collisions entail a larger entropy deposition.

With the initial entropy profile  $s(r)$ , it is now possible to initialize the temperature of the QGP. The pressure of a system and its temperature are related via an Equation of State  $P(T)$ , which in the present analysis is taken from [49]. Moreover, the pressure

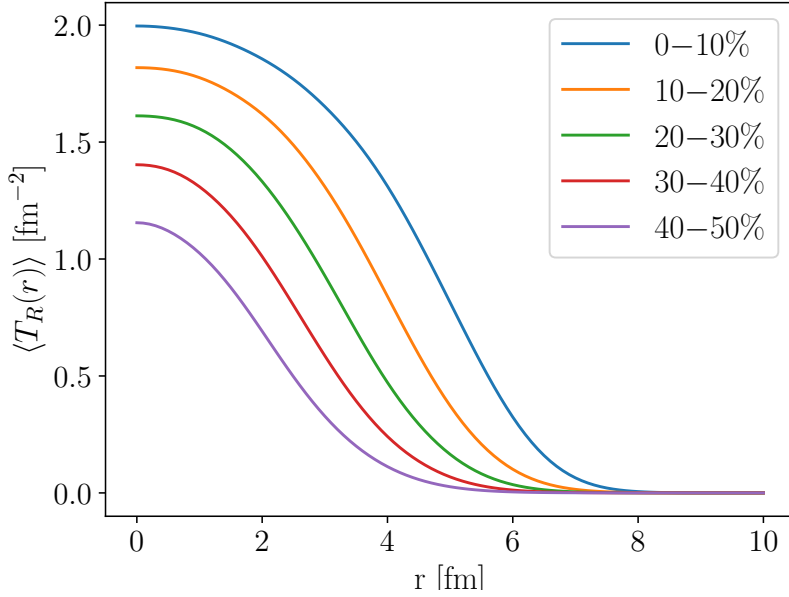


**Figure 4.3:** Averaged transverse density profiles  $\langle T_R(r) \rangle$  as a function of  $r$  for five different centrality classes in Au – Au collisions at  $\sqrt{s_{NN}} = 200$  GeV.

and the entropy density of a system are related by the thermodynamic relation  $P = \frac{ds}{dT}$ . Therefore, by inverting the EoS and using the aforementioned thermodynamic equation, one can obtain the temperature profile by knowing  $s(r)$ . A decreasing exponential tail with an asymptotic value of 10 MeV is attached to the obtained temperature profile at  $r = 8$  fm, in order to describe the temperature behavior at large radii. In Fig. 4.4 the initial temperature profile  $T(\tau_0, r)$  as a function of  $r$  is shown for the 0 – 10% centrality class. The initial temperature at the center of the fireball is  $T(\tau_0, 0) = 430$  MeV: this value is well below the initial LHC temperature of  $\sim 600$  MeV extracted using the same procedure [75]. This result is consistent with the expectations that lower energy systems produce a colder QGP state.

### 4.2.2 Heavy-quark density

Heavy quarks are produced almost exclusively during the initial hard scattering of nucleons, and their number is conserved throughout the entire evolution of the QGP. Following the work in [69], the density of heavy quarks-antiquarks pairs per unit of rapidity pro-

duced in the hard partonic scattering process at the initial time  $\tau_0$  can be expressed as,

$$n_{\text{hard}}^{Q\bar{Q}}(\tau_0, r, y = 0) = \frac{1}{\tau_0} \left. \frac{d^3 N^{Q\bar{Q}}}{dr dy} \right|_{y=0}, \quad (4.2)$$

where  $\frac{d^3 N^{Q\bar{Q}}}{dy dr}$  is the  $Q\bar{Q}$  rapidity distribution in nucleus-nucleus collisions and can be fixed from pQCD cross-section,

$$\frac{d^3 N^{Q\bar{Q}}}{dy dr} = n_{\text{coll}}(r) \sigma_{\text{inel}}^{\text{NN}} \frac{d\sigma^{Q\bar{Q}}}{dy}. \quad (4.3)$$

As already mentioned in Sec. 4.2 the value of the nucleon-nucleon inelastic cross-section is set to  $\sigma_{\text{inel}}^{\text{NN}} = 4.23 \text{ fm}^2$ . On the other hand,  $\frac{d\sigma^{Q\bar{Q}}}{dy}$  is the  $Q\bar{Q}$  cross-section, whose value is taken from analytical calculations at fixed perturbative order (FONLL) [82]. Focusing on charm quarks,  $\frac{d\sigma^{Q\bar{Q}}}{dy} = 0.0597 \text{ mb}$ . Finally,  $n_{\text{coll}}(r)$ , represents the density of binary nucleon-nucleon collisions. Plugging Eq. 4.3 into 4.2, the initial  $Q\bar{Q}$  density can be expressed as,

$$n_{\text{hard}}^{Q\bar{Q}}(\tau_0, r, y = 0) = \frac{1}{\tau_0} n_{\text{coll}}(r) \frac{1}{\sigma_{\text{inel}}^{\text{NN}}} \frac{d\sigma^{Q\bar{Q}}}{dy}. \quad (4.4)$$

In order to compute the value of  $n_{\text{hard}}^{Q\bar{Q}}$  we discuss in the next section how to estimate the nucleon-nucleon collision density  $n_{\text{coll}}(r)$ .

### 4.2.3 Binary nucleon-nucleon collisions

As underlined in Sec. 2.1.2,  $T_a(x, y)$  represents the probability per unit area of finding a nucleon of the nucleus  $A$  located in  $(x, y)$ . Thus, the product  $T_a(x, y) \cdot T_b(x - b_x, y - b_y) dx dy$  gives the joint probability per unit of area to find a nucleon of the nucleus  $A$  and a nucleon of the nucleus  $B$  located in the same differential transverse area  $dx dy$ .

In order to study the probability of collision between two nucleons, it is useful to introduce the *nuclear overlap function*, defined as [35],

$$T_{ab}(\vec{b}) = \int T_a(x, y) \cdot T_b(x - b_x, y - b_y) dx dy. \quad (4.5)$$

Where  $(b_x, b_y)$  represents the Cartesian components of the impact parameter.

Thus,  $T_{ab}(\vec{b})$  can be interpreted as an effective overlap area for which a specific nucleon in  $A$  can interact with a given nucleon in  $B$ . Knowing the probability of being located in the same unit of area, the probability of interaction between the two nucleons is then

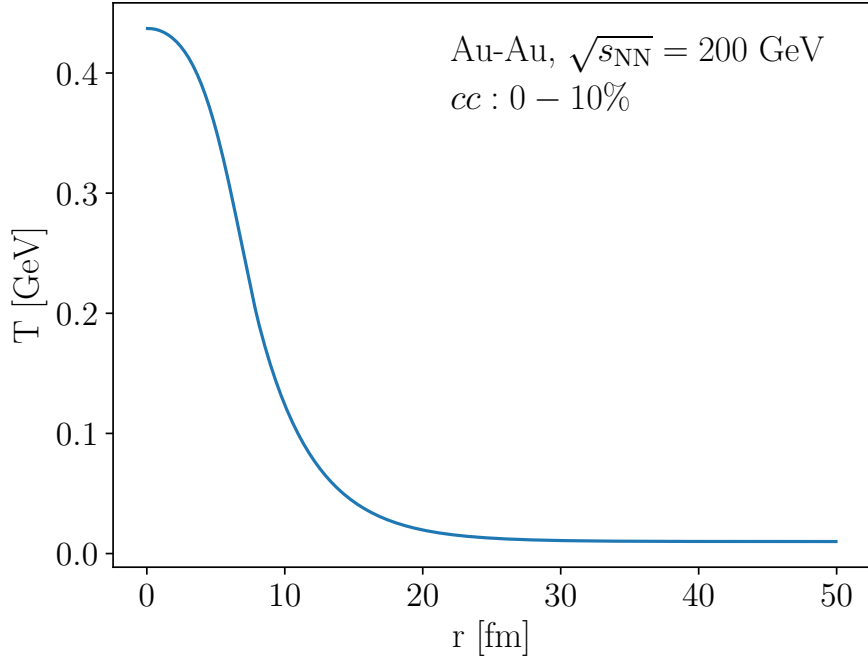


**Figure 4.4:** Initial temperature profile as a function of  $r$  for 0 – 10% centrality class.

given by,

$$P(\vec{b}) = T_{ab}(\vec{b}) \cdot \sigma_{\text{inel}}^{\text{NN}}. \quad (4.6)$$

Elastic processes lead to very little energy loss and are therefore neglected in this calculation.

Once the probability of a single nucleon-nucleon interaction is calculated, the probability of having  $n$  interactions between nucleus  $A$  (with  $n_A$  nucleons) and  $B$  (with  $n_B$  nucleons) is expressed using the binomial distribution,

$$P_n(\vec{b}) = \binom{n_A \cdot n_B}{n} \left[ T_{ab}(\vec{b}) \sigma_{\text{inel}}^{\text{NN}} \right]^n \left[ 1 - T_{ab}(\vec{b}) \sigma_{\text{inel}}^{\text{NN}} \right]^{n_A n_B - n}, \quad (4.7)$$

where the first term represents the number of combinations for  $n$  collisions out of  $n_A \cdot n_B$  possible nucleon-nucleon interactions, the second term is the probability for having exactly  $n$  collisions, and the last term is the probability of having  $n_A \cdot n_B - n$  missed collisions. Moreover, if the nuclei are not polarized, the vector impact parameter  $\vec{b}$  can be replaced by a scalar distance  $b$ : all the following quantities will be therefore expressed as dependent only on the modulus of the impact parameter.

The average number of binary collisions when  $A$  and  $B$  collide with impact parameter  $b$

can be obtained using the binomial distribution's properties. In particular, the average number  $\mu$  of the binomial distribution is  $\mu = \sum_n n \cdot P_n$ . Therefore, the total number of nucleon-nucleon binary collisions is given by,

$$\langle N_{\text{coll}}(b) \rangle = \sum_{n=1}^{n_A n_B} n P_n(b) = n_A \cdot n_B \cdot T_{ab}(b) \sigma_{\text{inel}}^{\text{NN}}. \quad (4.8)$$

The average number of binary collisions can also be expressed by integrating the density of binary collisions in  $[x, y]$  plane:

$$\langle N_{\text{coll}}(b) \rangle = \int n_{\text{coll}}(x, y, b) dx dy. \quad (4.9)$$

Since the nuclear overlap function is also given by an integral in  $x$  and  $y$  in 4.5, it is now possible to equate the arguments of the two integrals:

$$n_{\text{coll}}(x, y, b) = n_A \cdot n_B \cdot T_a(x, y) \cdot T_b(x - b_x, y - b_y) \sigma_{\text{inel}}^{\text{NN}}. \quad (4.10)$$

Similarly to the entropy density profile, the density of binary collision is then averaged for different centrality classes, and a coordinate transformation is performed to obtain  $n_{\text{coll}}(r, b)$ . Knowing the density of binary nucleon-nucleon collision,  $n_{\text{hard}}^{Q\bar{Q}}(\tau_0, r, y = 0)$  can then be obtained from Eq. 4.4. Figure 4.5 depicts the density of  $Q\bar{Q}$  as a function of the radius for 0 – 10% centrality class. Here it is shown that the heavy quark production is maximum at the center of the fireball (where more nucleon-nucleon collisions are expected to occur) and smoothly decreases with  $r$ . Moreover, for  $r > 7$  fm the number of produced HQ becomes negligible.

From the knowledge of  $n_{\text{hard}}^{Q\bar{Q}}(\tau_0, r, y = 0)$  the number of charm pairs produced per each event per unity of rapidity at RHIC is inferred,

$$\frac{dN^{Q\bar{Q}}}{dy} = 2\pi\tau_0 \int n_{\text{hard}}^{Q\bar{Q}}(\tau_0, r, y = 0) \cdot r dr \sim 1.5, \quad (4.11)$$

resulting compatible with the value computed by statistical models [78], which predict  $\frac{dN^{Q\bar{Q}}}{dy} = 1.6$  charm pairs produced in most central collisions. This result is an order of magnitude less than the number of charm quarks produced at the LHC, where  $\frac{dN^{Q\bar{Q}}}{dy} \sim 30$  [69].

By integrating the density of binary collisions, we obtain that  $\langle N_{\text{coll}} \rangle \sim 950$ . Amongst other parameters, the TRENTo model gives as output the average number of binary

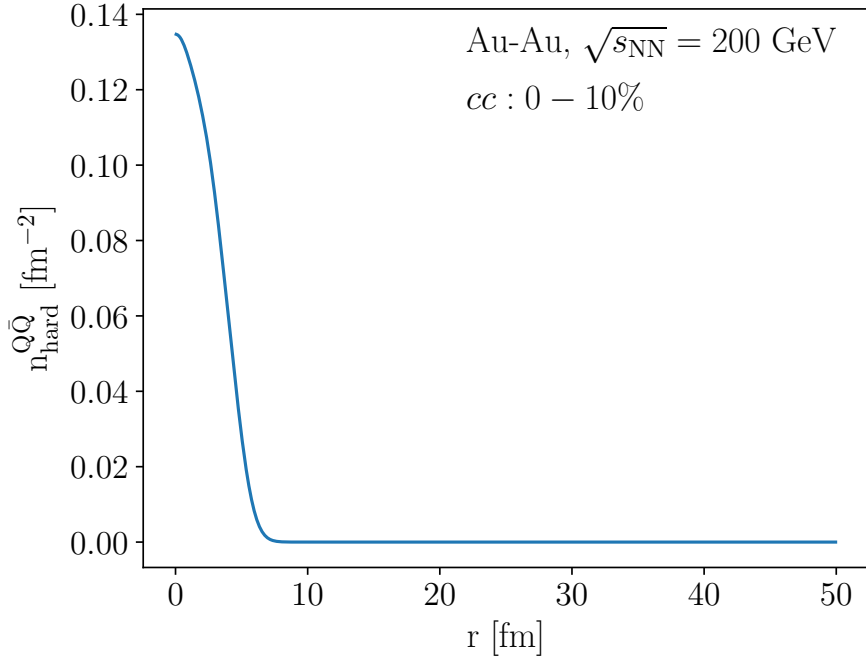


**Figure 4.5:** Initial density profile as a function of  $r$  for 0 – 10% centrality class.

nucleon-nucleon collisions  $\langle N_{\text{coll}} \rangle$  per event. The average number  $\langle N_{\text{coll}} \rangle$  calculated by T<sub>R</sub>ENTo is compatible with the integrated density of binary collisions, supporting the validity of our calculations.

#### 4.2.4 Initial fugacity

The fugacity factor  $\gamma_Q = e^{\mu_Q(x)/T(x)}$  introduced in Sec. 3.2.2 is a fundamental quantity in heavy-quark dynamics, since it provides an indication of how far from chemical equilibrium HQs are.

The density of heavy quarks created by hard collisions is related to the density of heavy quarks in thermal equilibrium via the Landau matching conditions.

$$n_{\text{hard}}^{Q\bar{Q}}(\tau_0, r, y = 0) \equiv n_{\text{equilibrium}}(T, \alpha), \quad (4.12)$$

where  $\alpha \equiv \frac{\mu_Q(x)}{T(x)} = \ln \gamma_Q$ . Following [75], it is possible to express the thermal equilibrium charm-quark density using the hadron-resonance gas equation for charm quarks (HRGc),

$$n_{\text{equilibrium}}(T, \alpha) = \frac{T}{2\pi^2} \sum_{i \in \text{HRGc}} q_1 M_i^2 e^{q\alpha} K_2(M_i/T), \quad (4.13)$$

where  $M_i$  represents the mass of charmed hadrons and  $q_i$  the charm charge. The HRGc equation is the EoS for charm quarks at temperatures close to the pseudo-critical temperature  $T_c$ , obtained using a grand canonical ensemble. For the temperature reached in most central collisions, the HRGc estimates larger multiplicities (of about a factor of five) than the ones obtained from the density of the free charm quarks. Nevertheless, in the absence of EoS models at QGP temperatures, the HRGc relation is assumed to also be valid at higher  $T$ .

In order to calculate the density in the case of full chemical equilibrium of the heavy quarks, it is sufficient to set  $\alpha = 0$  in Eq. 4.13, or in other words  $\gamma_Q = 1$ . Thus, the fugacity at the initial time  $\tau_0$  is estimated as,

$$\gamma_Q = \frac{n_{\text{hard}}^{Q\bar{Q}}(\tau_0)}{n_{\text{chemical equil.}}^{Q\bar{Q}}(\tau_0)} \approx 0.018. \quad (4.14)$$

Since  $\gamma_Q < 1$ , at RHIC the charm quarks are initially underpopulated with respect to their chemical-equilibrium abundance, similarly to what is observed at the LHC [69]. Once the initial fugacity and initial temperature are fixed, the heavy-quark density can be evolved using Eq. 4.13.

## 4.3 Applicability of the hydrodynamic approach

### 4.3.1 Heavy quarks in FluiduM

The FluiduM framework introduced in Sec. 2.2.3 evolves five independent fields related to the properties of the QGP medium. The initialization of the temperature was already addressed in 4.2.1; except for the temperature, FluiduM sets all the remaining background fields to zero:  $u^r = \pi_\phi^\phi = \pi_\eta^\eta = \pi_{\text{bulk}} = 0$ , respecting relativistic causality [50].

In order to model the heavy-quark dynamics in the QGP, it is necessary to extend the framework to heavy-quark fields. One of the base assumptions to do this is to assume that HQs do not significantly influence the energy density, the pressure, the velocity, and the shear stress of the medium: therefore the background fields are determined by the thermodynamics of light quarks and of gluons. To fully describe HQ dynamics in 1+1 dimensions it is sufficient to consider two independent fields: the logarithm of the fugacity  $\alpha$  and the radial component of the diffusion current  $\nu^r$ . The equations for  $\alpha$  and  $\nu^r$ , Eq. 3.30 and 3.40 respectively, can again be reduced to hyperbolic equations.

Therefore, a heavy-quark Nambu spinor is built:  $\Phi_{\text{HQ}} = \Phi_{\text{HQ}}(\alpha, \nu^r)$ , and the equation of motion of heavy quarks and background reads,

$$A_{\text{HQ}}\partial_\tau\Phi_{\text{HQ}} + B_{\text{HQ}}\partial_r\Phi_{\text{HQ}} + C_{\text{HQ}}\partial_\tau\Phi_{\text{bg}} + D_{\text{HQ}}\partial_r\Phi_{\text{HQ}} = S_{\text{HQ}}, \quad (4.15)$$

where  $A_{\text{HQ}}$ ,  $B_{\text{HQ}}$ ,  $C_{\text{HQ}}$  and  $D_{\text{HQ}}$  are  $2 \times 2$  matrices whose elements are non-linear functions of the background  $\Phi_{\text{bg}}$  and heavy-quark  $\Phi_{\text{HQ}}$  fields. The fugacity field is initialized as described in 4.2.4, whereas, in the absence of an initial state model, the radial diffusion current  $\nu^r$  is initially set to zero.

At the freeze-out, heavy-quark  $p_{\text{T}}$  spectra are obtained by employing a Cooper-Frye prescription. Following Eq. 2.38 the freeze-out spectra are calculated by integrating the particle distribution function  $f = f_{\text{eq}} + \delta f$ , where  $\delta f$  is the term accounting for the out-of-equilibrium corrections. In the case of heavy-quark dynamics,  $\delta f = \delta f^{\text{shear}} + \delta f^{\text{bulk}} + \delta f^{\text{diffusion}}$ . However, none of the current models provide an estimation of the out-of-equilibrium corrections for HQ, which are thus neglected in the present analysis.

The multiplicity of heavy quarks is given by integrating the zeroth component of the HQ current  $N_Q^\mu$ , which depends on the diffusion current as in Eq. 3.29: thus, the value of  $\delta f^{\text{diffusion}}$  at freeze-out is of fundamental importance to correctly calculate the number of HQ. The heavy-quark spatial diffusion coefficient  $D_s$  tunes the diffusion current: therefore, a large value of  $D_s$  translates into large corrections  $\delta f^{\text{diffusion}}$ . Setting  $\delta f^{\text{diffusion}} = 0$  hence entails a non-physical dependence of HQ multiplicity on the value of  $D_s$ : since  $D_s$  is a fundamental parameter for the description of heavy-quark dynamics in the QGP, this issue needs to be addressed in the near future.

With the described framework, it is now possible to study heavy-quark dynamics in the QGP. However, before going into the details of the model results, it is important to verify if the use of a hydrodynamic approach for HQ at RHIC energies is justified.

### 4.3.2 Bjorken Flow

The Bjorken flow, as described in [83], characterizes the motion of a system that is invariant under longitudinal Lorentz boosts and exhibits azimuthal symmetry. This flow entails a purely longitudinal expansion along the transverse axis  $z$ , and, thus, the transverse components of the fluid velocity are equal to zero,

$$u^\mu = \left( u^t, 0, 0, \frac{z}{t} \right). \quad (4.16)$$

Even if this model represents a simplification, it can be considered a good approximation for the QGP expansion until the transverse distances become comparable to the nuclear radii. As a matter of fact, the transverse flow takes some time to develop after the collision. Natural variables for describing Bjorken flow are the rapidity  $y$  and the longitudinal proper time  $\tau$ . As already mentioned in Sec. 2.2, a fluid is characterized by a local energy density  $\epsilon(x)$ , a pressure  $p(x)$ , a temperature  $T(x)$ , and a four-velocity  $u_\mu(x)$ , and its equation of motion is found imposing the conservation of the energy-momentum  $\partial_\mu T^{\mu\nu} = 0$ . Considering an ideal fluid, the energy-momentum tensor is expressed as in Eq. 2.14. In the case of Bjorken flow, all the local variables depend on  $\tau$  and  $y$  only, and the initial condition at  $\tau = \tau_0$  imposes that,

$$\epsilon(\tau_0, y) = \epsilon_0, \quad p(\tau_0, y) = p_0, \quad T(\tau_0, y) = T_0, \quad u_\mu(\tau_0, y) = \frac{1}{\tau_0} (t, 0, 0, z). \quad (4.17)$$

These conditions are longitudinally boost invariant, and this symmetry is conserved through the evolution of a system: thus, if there is no dependence of thermodynamics variables on the rapidity, there will be no such dependence at later times either.

With this simplification, the conservation of the energy-momentum tensor reduces to,

$$\frac{d\epsilon}{d\tau} = -\frac{\epsilon + p}{\tau}. \quad (4.18)$$

In an ideal gas, the energy density and the pressure are related via a linear equation  $\epsilon = 3p$ . Plugging this expression in Eq. 4.18 entails,

$$\frac{d\epsilon}{d\tau} = -\frac{4/3\epsilon}{\tau} \rightarrow \frac{\epsilon}{\epsilon_0} = \left(\frac{\tau}{\tau_0}\right)^{4/3}. \quad (4.19)$$

It is now possible to use the EoS of an ideal gas:  $\epsilon \propto T^4$ . Thus, the temperature evolution in Bjorken flow can be expressed as,

$$T(\tau) = T_0 \left(\frac{\tau_0}{\tau}\right)^{1/3}. \quad (4.20)$$

Moreover, for a fluid undergoing Bjorken expansion, it can be shown [83] that the expansion rate is given by,

$$\theta = \partial_\mu u^\mu = \frac{1}{\tau}. \quad (4.21)$$

The expansion time scale on the other hand is defined as the inverse of the expansion rate, and thus in this simplified scenario coincides with  $\tau$ ,

$$\tau_{\text{exp}} \equiv \frac{1}{\theta} = \tau. \quad (4.22)$$

Equations 4.20 and 4.22 will be employed to study the relation between the HQ relaxation time and the expansion time of the fireball in the next section.

### 4.3.3 Charm relaxation time

The heavy-quark relaxation time  $\tau_n$  represents the time scale needed by the HQs to relax to kinetic equilibrium. Thus, for the charm quarks to be described by fluid-dynamic equations it is necessary that  $\tau_n \ll \tau_{\text{exp}}$ . In Fig. 4.6 the comparison between  $\tau_n$  and  $\tau_{\text{exp}}$  as functions of the longitudinal proper time is reported. In the simplified picture of Bjorken flow the expansion time is equal to the longitudinal proper time: thus the expansion time is represented as the bisector of the  $\tau_n - \tau$  plane. The initial temperature is set to 430 MeV as found in Sec. 4.2.1, and the initial time to  $\tau_0 = 0.4$  fm following [75]. As for the case of LHC studies [75],  $D_s T$  ranges are taken from lQCD calculations [84, 85], and from fits to experimental measurements of the ALICE collaboration [86]. In the case of [85], a dependence of  $D_s T$  on the temperature is shown. However, as a first approximation, we assume here that  $D_s T$  remains constant throughout the evolution of the fireball, and we take the value of  $D_s T$  at  $T = T_c \sim 155$  MeV. In the future, it will be possible to consider a linear dependence of  $D_s T$  with the temperature, in order to mimic the trend observed by lQCD calculations. Moreover, it is important to remark that at RHIC top energies, the pseudo-critical temperature is comparable to the one of LHC [27]: therefore the values of  $D_s T_c$  used for LHC studies, can be applied in the present analysis as well.

Recalling Eq. 3.45, the relaxation time is directly proportional to the HQ spatial diffusion coefficient  $D_s$ : thus exploring different regions of  $D_s T$  translates into exploring different values of  $\tau_n$ . In the case of the most recent lQCD calculations (yellow band),  $\tau_n$  results well below the expansion time of the fireball: even if Bjorken flow does not accurately describe the full evolution of the plasma, this result strongly supports the applicability of the hydrodynamic approach to charm quark at RHIC top energies.

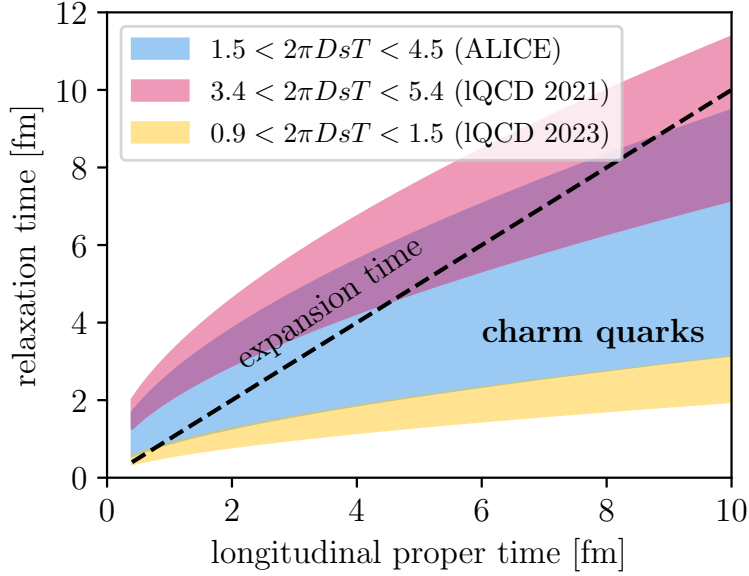


**Figure 4.6:** Relaxation time and expansion time of charm quarks as a function of the longitudinal proper time, in the case of Bjorken flow.

## 4.4 Charmed hadron spectra

It is now possible to study the transverse momentum spectra of charmed hadrons and compare them to the available experimental data measured by STAR collaboration in Au – Au collisions at  $\sqrt{s_{\text{NN}}} = 200$  GeV. In the current work, we will focus on  $D^0$ ,  $D_s^+$  mesons in the centrality class 0 – 10% and on  $J/\psi$  in the centrality class 0 – 20% [87, 88, 89].

At RHIC top energies the baryon chemical potential at freezeout is  $\mu_B \sim 20$  MeV [90]. Thus, the distribution function of heavy quarks  $f_k^Q$  at local kinetic equilibrium should also take into account the  $\mu_B(x)$  contribution in its exponential. To do so,  $\mu_B(x)$  needs in principle to be considered as an additional independent field of FluidM, and evolved via fluid-dynamic equations. However, knowing the initial fugacity and the initial temperature of the fireball from Sec. 4.2, it is possible to compute the value of the initial heavy-quark chemical potential,  $\mu_Q \sim \mathcal{O}(10^3 \text{ MeV})$  at the center of the fireball. We calculated that a similar result also holds at the freezeout: since the heavy-quark chemical potential is two orders of magnitudes larger than the baryon chemical potential, in the present analysis we will neglect the contribution of  $\mu_B(x)$ . If in the future we extend our study to lower energy systems, where  $\mu_B \sim \mathcal{O}(10^2 \text{ MeV})$  [90], an implementation of the

baryon chemical potential in FluiduM will need to be addressed.

At RHIC, the total number of charmed hadrons per unit of rapidity is expected to be smaller than unity even for the most central collisions. For this reason, following the work of [91] and [92], the exact conservation of charm quark number should be imposed, or, in other words, a canonical ensemble (CE) formalism should be used to describe charm hadron multiplicities. This problem is addressed by introducing a *canonical suppression factor*, which is the same for all individual open charm states. Being  $N_{oc}$  the number of charmed hadrons calculated by the grand canonical formalism, and  $N_c^{\text{tot}}$  the total number of charm quarks, the corrected number of open charm hadrons  $N_{oc}^{\text{ce}}$  can be expressed as [91],

$$N_{oc}^{\text{ce}} = \sum_{\alpha=1,2} N_{oc,\alpha} \frac{I_\alpha(N_c^{\text{tot}})}{I_0(N_c^{\text{tot}})}, \quad (4.23)$$

where  $I_0$  and  $I_\alpha$  are modified Bessel functions. For hadrons with two or three charm quarks, there are generally additional correction terms that are, however, small compared to Eq. 4.23, and can be at first approximation neglected. Notice that, since the number of produced open charm hadrons is well above the unit, at LHC energies it is not necessary to take into account the presence of this correction factor.

In order to study the  $p_T$  spectra of charmed hadrons several fluid parameters need to be fixed. The values of diffusion coefficients  $\eta/s = 0.1$  and  $\zeta/s = 0.05$  are taken from [59]. In this analysis, a simplified model of the freeze-out is considered, and kinetic and chemical freeze-outs are assumed to occur at the same temperature: for this reason, a single temperature parameter  $T_{fo} = 156.5$  MeV [91] is set. In the future, it would be appropriate to incorporate a partial chemical equilibrium phase, in order to describe better the later stages of the evolution, as done in [79].

The momentum spectra are produced for the non-diffusive case  $D_s T = 0$ , and for the upper limit predicted by lQCD at the pseudo-critical temperature  $T_c$  [85],  $D_s T = 0.24$ . The value of  $D_s$  should not in principle influence the particle multiplicity. However, the predicted yield differs for different values of  $D_s$  because of the missing dissipative corrections at freeze-out, as introduced in Sec. 4.3.1. Figure 4.7 shows the model results compared to the experimental data for  $D^0$  and  $D_s^+$  mesons. The model band well describes the experimental  $p_T$  spectra in the low momentum region ( $p_T < 4$  GeV), where the fluid-dynamic approach is expected to be valid.

A similar approach can also be applied for  $J/\psi$  mesons. In this case, since the charm content is double, the model band is expected to be broader, leading to a less precise description of the  $J/\psi$  experimental spectrum. Nevertheless, the experimental data are

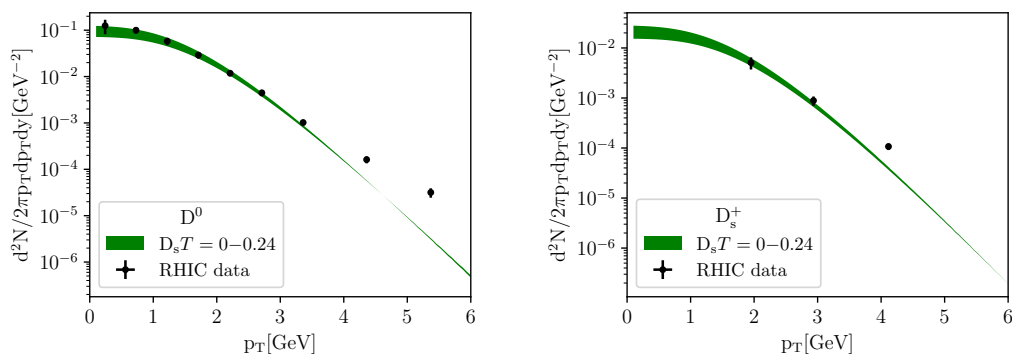


**Figure 4.7:** Comparison between model and experimental  $p_T$  spectra for  $D^0$  meson (left panel) and for  $D_s^+$  meson (right panel) for 0 – 10% centrality class.

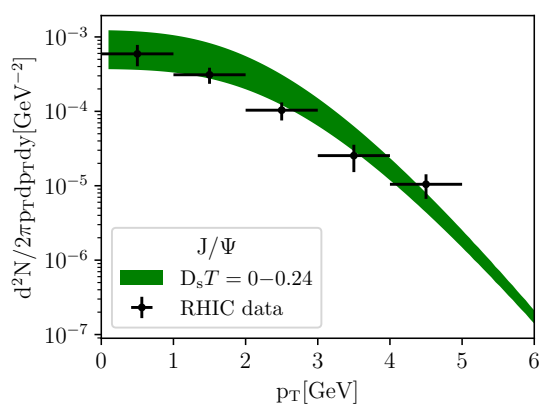


**Figure 4.8:** Comparison between model and experimental  $p_T$  spectra for  $J/\psi$  meson for 0 – 20% centrality class.

well described by the current model up to 5 GeV, depicted in Fig. 4.8.

All the model results shown here and in [75] were obtained using values of  $D_s T$ , of the transport coefficients  $\eta/s$  and  $\zeta/s$  and of the freeze-out temperature fixed from the literature. However, in the current work, a phenomenological approach to estimate both heavy-quark and transport coefficients is presented, based on Bayesian inference and mainly inspired by [79].

# 5 Analysis framework

## 5.1 The Bayesian inference

Bayes' theorem, or the theorem of the compound probability is a mathematical tool widely used in statistics to compute conditional probabilities. Given a set of  $n$  parameters  $\mathbf{x} = (x_1, x_2, \dots, x_n)$  and an experimental data vector  $\mathbf{Y}$ , the probability of the set  $\mathbf{x}$  with respect to the data  $\mathbf{Y}$  can be calculated as,

$$P(\mathbf{x}|\mathbf{Y}) = \frac{P(\mathbf{Y}|\mathbf{x})P(\mathbf{x})}{P(\mathbf{Y})}, \quad (5.1)$$

where  $P(\mathbf{Y}|\mathbf{x})$  represents the likelihood, and quantifies how likely it is to observe the data  $\mathbf{Y}$  given a specific set of the parameters  $\mathbf{x}$ . On the other hand,  $P(\mathbf{x})$  and  $P(\mathbf{Y})$  known respectively as the *prior* and *marginal* probability, are the probabilities of observing  $\mathbf{x}$  and  $\mathbf{Y}$  without any given conditions. Since the marginal probability does not depend on the parameters  $\mathbf{x}$ , in this work it will be considered as a normalization constant.

The Bayesian approach is applicable to many areas of physics: it is widely used, for example, to discriminate between different hypotheses  $\mathbf{x}$  by measuring  $\mathbf{Y}$  experimental data. For the current analysis, the hypotheses  $\mathbf{x}$  is represented by the fluid-dynamics parameters used as input for the simulation, whereas the data  $\mathbf{Y}$  are the experimental and the model  $p_T$  spectra. In the following sections, the explicit form of the prior distribution  $P(\mathbf{x})$  and of the likelihood function  $P(\mathbf{Y}|\mathbf{x})$  will be addressed.

### 5.1.1 Priors distribution

The prior probability expresses the initial confidence about the likeliness of each parameter and may vary from individual to individual. It is possible to eliminate this subjectivity associated with the priors through an iterative process or by increasing the number of measurements  $\mathbf{Y}$ . Nevertheless, a good physical result should not depend on the choice of the prior, and by replacing a value with another one equally reasonable, the variations in the result should be small enough.

Since in the current analysis, there are no physical reasons to favor one parameter set over another, given  $m$  parameter sets it is appropriate to consider a uniform prior distribution,

$$P(\mathbf{x}) = \begin{cases} 1 & \text{if } x_i^{\min} < x_i < x_i^{\max} \quad \forall i \in [1, m] \\ 0 & \text{otherwise,} \end{cases} \quad (5.2)$$

where the parameter ranges  $[x_i^{\min}, x_i^{\max}]$  are given as input of the analysis. Since it is assumed that there is no possibility of observing parameters outside their given range, it is important that  $[x_i^{\min}, x_i^{\max}]$  includes all the plausible values.

### 5.1.2 Likelihood function

As introduced in Sec. 5.1, the likelihood  $P(\mathbf{Y}|\mathbf{x})$  represents the conditional probability of observing the experimental data  $\mathbf{Y}$  given a parameter set  $\mathbf{x}$ : for this reason  $P(\mathbf{Y}|\mathbf{x})$  quantifies the quality of the fit to data, accounting for all sources of uncertainty.

To study how the likelihood can be constructed, let us consider the vector of data experimentally measured  $\mathbf{y}_e$ , and the vector of data  $\mathbf{y}_e^{\text{true}}$  labeled as *true*, which correspond to the underlying physical values not influenced by the measurement. The two vectors can be related as [93],

$$\mathbf{y}_e = \mathbf{y}_e^{\text{true}} + \epsilon_e, \quad (5.3)$$

where the error  $\epsilon_e$ , which accounts for all sources of experimental uncertainty, is a  $n$ -dimension normal distribution (also called *multivariate normal distribution*) centered in zero and with covariance matrix  $\Sigma_e$ .

A similar relation also holds for the case of model output  $\mathbf{y}_m$  with input parameters  $\mathbf{x}$ , and the *ideal* model output  $\mathbf{y}_m^{\text{ideal}}(\mathbf{x})$ , which represents the hypothetical calculations of a perfect physical model with unlimited precision,

$$\mathbf{y}_m(\mathbf{x}) = \mathbf{y}_m^{\text{ideal}}(\mathbf{x}) + \epsilon_m. \quad (5.4)$$

Once again the model uncertainty is a multivariate normal distribution with covariance matrix  $\Sigma_m$ . It is now possible to assume that there exist some values of the parameters  $\mathbf{x}_{\text{best}}$  at which the ideal model calculation is equal to the true experimental data,

$$\mathbf{y}_e^{\text{true}} = \mathbf{y}_m^{\text{ideal}}(\mathbf{x}_{\text{best}}) \rightarrow \mathbf{y}_e = \mathbf{y}_m(\mathbf{x}_{\text{best}}) + \epsilon, \quad (5.5)$$

where  $\epsilon$  has covariance matrix  $\Sigma = \Sigma_m + \Sigma_e$ , and takes into account all sources of uncertainty.

This relation between the model and experimental data implies that the likelihood can be expressed as a multivariate normal distribution in  $n$  dimensions [93],

$$P(\mathbf{Y}|\mathbf{x}) = \frac{1}{\sqrt{(2\pi)^n \det \Sigma}} \exp \left\{ -\frac{1}{2} [\mathbf{y}_m(\mathbf{x}) - \mathbf{y}_e]^T \Sigma^{-1} [\mathbf{y}_m(\mathbf{x}) - \mathbf{y}_e] \right\}. \quad (5.6)$$

Knowing the prior distribution and the likelihood function, the posterior probability can thus be calculated via Eq. 5.1. However, to obtain the full probability distribution, the posterior probability should be known for any set of parameters  $\mathbf{x}$  in the parameter space. Since an analytic treatment is not applicable in this specific case, numerical methods need to be implemented. For this reason, first machine learning techniques are used to perform a regression on FluiduM results. Afterward, to infer the parameters' probability distribution, the numerical Markov-chain Monte Carlo method is employed.

## 5.2 Machine learning techniques

In recent years, machine learning (ML) methods have emerged as powerful tools in many research areas. ML algorithms can handle multidimensional datasets and solve complex non-linear problems: for this reason, they increasingly represent a fundamental technique for particle physics as well. In the heavy-ion collisions sector for example, impact parameter determination via neural networks dates back to 1990 [94], and ML has been recently used to identify the QCD phase transition [95] as well as to determine the temperature in the collision [96].

Machine learning algorithms can be categorized into two different macro categories: *supervised* and *unsupervised* learning. In supervised learning, labeled datasets are used to train algorithms to predict outcomes. Thus, after the training, a function that maps new data on expected output values is built. An optimal scenario will allow for the algorithm to correctly determine output values for unseen instances. On the other hand, unsupervised method algorithms learn from unlabeled data, trying to find any similarities, differences, patterns, and structure in the data. For the present analysis, we employ supervised learning, and in particular neural network algorithms, which are introduced in the next section.

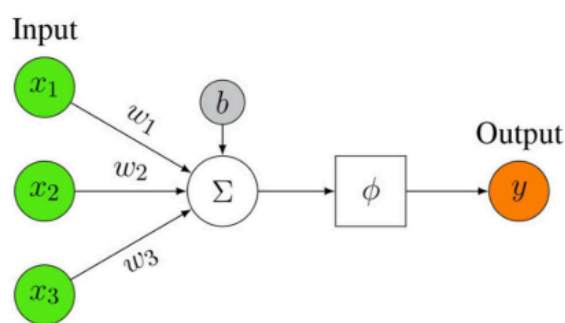


**Figure 5.1:** Representation of an artificial neuron model, where the different input vectors  $\mathbf{x}_i$  are multiplied for the respective weights  $\mathbf{w}_i$ , summed up to a bias  $b$  and used as argument of the activation function  $\phi$ . Figure taken from [97].

### 5.2.1 Neural Networks

Artificial neural networks (ANNs), usually abbreviated as neural networks (NNs), are a class of machine learning supervised algorithms developed in the 1980s. Like many other artificial intelligence algorithms, NNs were motivated to address the different aspects of learning, such as the induction and prediction processes. Most ANN algorithms have two common features. First, they are composed of a network of simple processing units, also referred to as *artificial neurons* or *nodes*, that are mutually connected: this feature makes an ANN model similar to a human brain. Second, a NN model typically does not make any prior assumptions about data distribution before learning. This greatly promotes the usability of neural networks in various applications.

Each artificial neuron takes as input a vector  $\mathbf{x}$  multiplied by a weight  $\mathbf{w}^T$  and added to a scalar bias  $b$ . The sum of these terms,  $z = \mathbf{w}^T \mathbf{x} + b$  forms the argument of an activation function,  $\phi$ , resulting in the output of the neuron model  $\mathbf{y}$  [97],

$$\mathbf{y} = \phi(z) = \phi(\mathbf{w}^T \mathbf{x} + b) \quad (5.7)$$

The activation function  $\phi$  can in principle be any function that satisfies a  $\mathbb{R} \rightarrow \mathbb{R}$  mapping and is piece-wise differentiable: its explicit form depends on the specific applications. The Rectified Linear Unit function (ReLU) [98] currently represents one of the most popular activation functions used in neural networks. In Fig. 5.1 a simple drawing of an artificial neuron is represented.

In order to build networks, the neurons need to be connected, and thus the outputs of some neurons are used as inputs to other ones. The simplest connection is represented

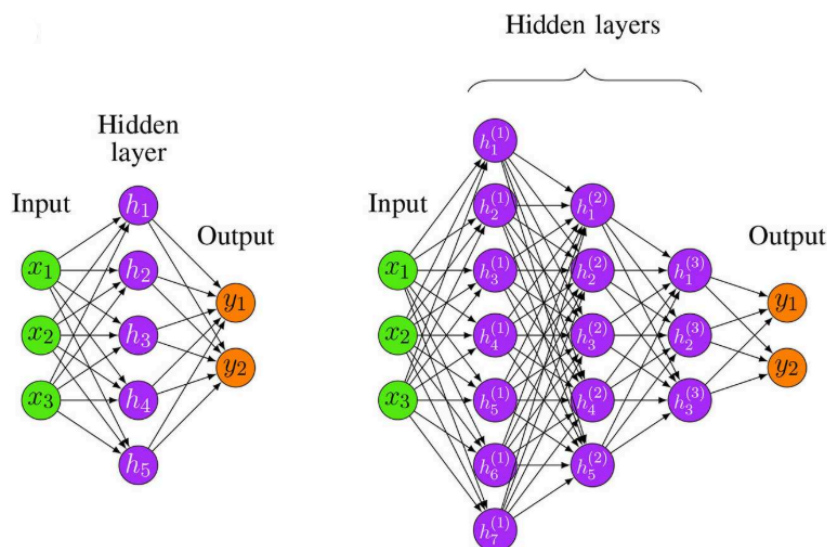


**Figure 5.2:** Schematic representation of a shallow FFNN (left panel), and of a deep FFNN with three hidden layers (right panel). Figure taken from [97].

by a feed-forward neural network (FFNN) in which neurons are only connected in the forward direction, and no loops are allowed. The information signals travel from the first layer, called the *input* layer to the final layer (the *output* layer), possibly passing through multiple intermediate layers, known as *hidden* layers. A network is typically called a *deep neural network* if it has at least two hidden layers, as depicted in Fig. 5.2. The number of hidden layers and of nodes per layer have a large impact on the performance of a NN, and hence their choice is of fundamental importance.

### 5.2.2 Loss function

In the supervised learning approach, it is common to define a *loss function*, which typically is expressed as the difference between estimated and true values. The loss function is a measurement of how good the machine learning model is to predict the expected outcome and can be used for parameter estimation. One of the most common loss functions for NNs algorithms is the mean squared error function (MSE). Considered  $n$  training samples, with input value  $x_i$  and target value  $f_i$ , the MSE is defined as,

$$F(\mathbf{w}) = \frac{1}{n} \sum_{i=1}^n F(\mathbf{w}) = \frac{1}{n} \sum_{i=1}^n (y(x_i, \mathbf{w}) - f_i), \quad (5.8)$$

where  $y(x_i, \mathbf{w})$  represents the prediction of the neural network for input value  $x_i$  and weight  $\mathbf{w}$ . The minimization of the loss function with respect to the weight parameters is usually not solvable analytically, and can be addressed using iterative approaches, such as the *gradient descent* method. Given a starting value  $\mathbf{w}_0$ , this algorithm gives an approximation of the minimum of the function  $F(\mathbf{w})$  after the  $n$  interactions [99],

$$\mathbf{w}_{n+1} = \mathbf{w}_n - \eta \nabla F(\mathbf{w}_n), \quad (5.9)$$

where  $\eta$  is known as the *learning rate*. The choice of  $\eta$  is fundamental to reducing the number of iterations needed to reach the approximate solution. The calculation of the gradient of  $F(\mathbf{w})$  can be computationally expensive, especially for a large dataset. For this reason, usually, only a random subset (*mini-batch*) is used to approximate the true gradient of  $F(\mathbf{w})$ : the result obtained by this method still allows for a good representation of the gradient of the full dataset.

### 5.2.3 Uncertainty quantification

The neural network output consists only of point predictions and does not provide any error estimation. In the majority of research analyses, however, uncertainties play a fundamental role: for this reason, several methods to account for error estimation in neural networks have been developed through the years. In the following, we will focus mainly on the ensemble method, since it represents the error estimation procedure used in the current analysis. An overview of other techniques, such as deterministic, bayesian, and Test-Time Data Augmentation methods can be found in [100].

The main idea of building an NN ensemble is that by combining multiple models, the errors of a single prediction will likely be compensated by other predictions, and, as a result, the overall performance of the ensemble would be better than that of a single prediction. The combination of the single predictions can be performed in several ways, among which the most common is the arithmetic average. Besides improving accuracy, building an ensemble of neural networks allows for defining a model's uncertainty, which is usually defined as the standard deviation of the predictions. Thus, the ensemble provides a valid estimation of the model uncertainty.

One of the most important aspects of the NN ensemble is the maximization of the variety among the members. This can be achieved by knowing that, due to the non-linearity of the network, different weight initializations can lead to different training results. Moreover, since the training is realized on mini-batches, the order of the training

data points can also affect the final result. For this reason, the increase in variety can be achieved by both random weight initialization and data shuffle.

### 5.3 Markov-chain Monte Carlo

Markov-chain Monte Carlo (MCMC) is a class of algorithms used for sampling probability distributions. In the case of Bayesian inference MCMC methods are typically used to draw samples from the posterior distribution  $P(\mathbf{Y}|\mathbf{x})$ .

Here, an initial candidate  $\mathbf{x}_0$  is first randomly chosen from the parameter space. Then a new proposal  $\mathbf{x}'$  is sampled from a given distribution called the *proposal distribution*. Usually, the proposal distribution is chosen to be sufficiently simple so that it is straightforward to draw samples from it, as the case of normal distributions. After the sampling, an algorithm is used to determine if the proposed sample  $\mathbf{x}'$  can be rejected or accepted. One of the most popular methods is the Metropolis-Hastings algorithm, where the acceptance probability  $r(\mathbf{x}', \mathbf{x}_0)$  is expressed as [101],

$$r(\mathbf{x}', \mathbf{x}_0) = \min \left( 1, \frac{P(\mathbf{Y}|\mathbf{x}') Q(\mathbf{x}_0; \mathbf{x}')}{P(\mathbf{Y}|\mathbf{x}_0) Q(\mathbf{x}'; \mathbf{x}_0)} \right). \quad (5.10)$$

Here  $Q(\mathbf{x}_0; \mathbf{x}')$ , known as *transition distribution* is usually parametrized by a multivariate Gaussian distribution centered in  $\mathbf{x}_0$ . To determine if  $\mathbf{x}'$  is accepted, a random number  $u$  is sampled from a uniform distribution: if  $r(\mathbf{x}', \mathbf{x}_0) > u$  the new proposal is accepted and  $\mathbf{x}_1 \equiv \mathbf{x}'$ , otherwise it gets rejected and  $\mathbf{x}_1 \equiv \mathbf{x}_0$ . It is important to notice that the initial samples are often discarded because the chain may start from a low probability area of the parameter space and hence may not represent the target distribution well. The number of samples discarded is usually referred to as *burn-in* samples.

Thus, Markov-chain represents a sequence of samples, where each sample is dependent on the previous one, as schematically depicted in Fig. 5.3. By this procedure, a random walk based on the posterior probability is performed: if the number of samples drawn (known as *workers*) is sufficiently high, the distribution of each parameter  $x_i$  will converge to a stationary distribution, where the mean represents the best estimate of  $x_i$ . Moreover, considering the width of the probability distribution in a given interval, the uncertainty related to  $x_i$  can also be estimated.

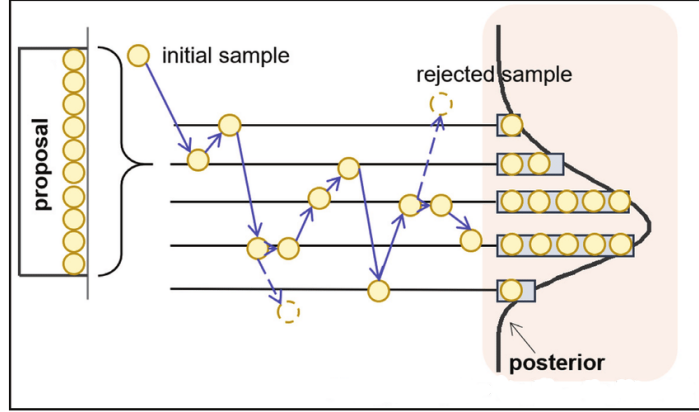


**Figure 5.3:** Schematic representation of Markov-chain Monte Carlo method sampling using random walk. Figure taken from [102].

## 5.4 Analysis implementation

### 5.4.1 Parameters set

Now that every analysis tool has been introduced, it is possible to give an overview of the workflow of the present work. First of all, the parameter set  $\mathbf{x}$  needs to be chosen. For the present work, six different parameters are used, of which five are related to the hydrodynamic evolution of the QGP, whereas one is related to heavy-quark dynamics. The parameters related to the fireball initial conditions, Norm and  $\tau_0$ , were already introduced in Sec. 4.2.1. Regarding the viscosity contribution, as mentioned in Sec. 2.2.2 the shear stress tensor and the bulk pressure are tuned by the relative coefficients  $\eta$  and  $\zeta$ . In the present work, the bulk viscosity coefficient over entropy is considered temperature-dependent and takes the Lorentzian form,

$$\frac{\zeta}{s}(T) = \frac{(\zeta/s)_{\max}}{1 + \left(\frac{T - T_{\text{peak}}}{T_{\text{width}}}\right)^2}, \quad (5.11)$$

where the peak  $T_{\text{peak}} = 175$  MeV and width temperature  $T_{\text{width}} = 24$  MeV are fixed from [103]. The value of  $(\zeta/s)_{\max}$  is taken as a free parameter for the Bayesian analysis. On the other hand, we consider here  $\eta/s$  independent of the system temperature. Following [104], the ratio between the diffusion coefficients and the respective relaxation

Norm	$\eta/s$	$(\zeta/s)_{\max}$	$\tau_0$ [fm]	$T_{\text{fo}}$ [MeV]	$D_s T$
5 – 80	0.08 – 1	$10^{-4}$ – 0.3	0.1 – 2	110 – 150	0 – 0.50

**Table 5.1:** Parameter ranges used in the current analysis.

times are assumed to be constant,

$$\frac{\tau_{\text{bulk}}}{\zeta/(\epsilon + p)} = \frac{1}{15 \left(\frac{1}{3} - c_s^2\right)^2} + \frac{a_{\text{offset}}}{\zeta/(\epsilon + p)}, \quad (5.12)$$

$$\frac{\tau_{\text{shear}}}{\eta/(\epsilon + p)} = 5, \quad (5.13)$$

where  $\epsilon$  represents the energy density,  $p$  the pressure,  $c_s$  the speed of sound, and  $a_{\text{offset}} = 0.1$  fm is a small offset introduced to ensure a casual radial expansion [50].

Strongly interacting field theories predict the existence of a lower bound for the shear viscosity to entropy ratio:  $\eta/s \geq \frac{1}{4\pi} \approx 0.08$  [105]. This value is conjectured to be universally valid for any fluid and will also be used in the present analysis as the lower constraint of  $\eta/s$ .

Since in this analysis, kinetic and chemical freeze-outs are assumed to occur at the same temperature, a single temperature parameter  $T_{\text{fo}}$  is needed.

The introduced parameters are related to the hydrodynamic evolution of the QGP, and in the following, we will commonly refer to them as *hydro model parameters*.

The last parameter, the HQ spatial diffusion coefficient multiplied by the temperature  $D_s T$  is related to heavy-quark dynamics, and its bounds are taken from [84, 85].

As mentioned before, the parameter ranges need to be chosen carefully, since every value outside these constraints is excluded. In Table 5.1 an overview of the ranges is presented, mainly inspired by [79]. It is important to underline that the lower range of the thermalization time is set to 0.1 fm due to simulation instabilities: as a matter of fact it was observed in [106] that FluiduM becomes unstable for  $\tau_0 < 0.1$  fm. Once the parameters' ranges are set, it is possible to build a Latin hypercube, that is a  $n$ -dimensional grid in which the parameters are sampled semi-randomly and uniformly within their ranges. In the current analysis, the number of sampled parameters is set to  $2 \cdot 10^4$ . All the parameter configurations are independent of each other and can be run in parallel: for this reason, it is possible to simultaneously run  $10^3$  tasks with 20 configurations each on a computing cluster, the Cluster Computing Infrastructure at GSI [107]. In the present work, considerable effort was dedicated to the optimization of the FluiduM package. FluiduM was originally written in Wolfram Language: however, since

this language is not open-source, the number of tasks that can be run in parallel is highly dependent on the number of licenses available. For this reason in the present analysis, a different version of FluiduM written in Julia was optimized and used. Julia is an open-source high-level programming language especially well suited for parallel computation [108]. With this new version of FluiduM, up to  $\sim 2 \cdot 10^2$  tasks can be simultaneously run on the cluster. Since each task takes on average three minutes, the entire simulation can be performed in 30 minutes: this performance represents a considerable improvement with respect to the previous version, with a running time of the order of three hours. In order to gain an initial understanding of the accuracy of the FluiduM simulation, it is possible to study the parameter configuration which minimizes the  $\chi^2$ , defined as,

$$\chi^2 = \sum_{i=1}^N \frac{y_{\text{Fluidum},i}(x) - y_{e,i}}{\sigma_{e,i}}, \quad (5.14)$$

where  $y_{e,i}$  is the experimental value of the transverse momentum spectrum of a particle species in the  $i$ -th  $p_T$  bin,  $y_{\text{Fluidum},i}$  is the corresponding FluiduM output for the parameter configuration  $x$ , and  $\sigma_{e,i} = \sqrt{\sigma_{\text{stat}}^2 + \sigma_{\text{sys}}^2}$  is the square-root of the sum of squares of the systematic and the statistical uncertainties of the experimental data.

The minimization of the  $\chi^2$  was used in [59] (one of the predecessors of this work) to find the optimal parameter configuration. However, this procedure had several limitations: for example, in the uncertainty quantification, the correlations between the parameters were not considered. To overcome these limitations, following [79], the optimal parameter configuration in this work will be inferred using Bayesian inference. We remark here that the emulator and the Markov-chain Monte Carlo routines used for the Bayesian analysis are almost integrally taken from [79].

### 5.4.2 Neural networks in the present analysis

In order to build a continuous posterior distribution as introduced in Sec. 5.1.2, it is necessary to employ an *emulator* which is able to mimic the behavior of FluiduM simulation. For each parameter configuration  $\mathbf{x}$  used as input, a model result  $\mathbf{y}$  is obtained as output: thus, the training samples of the emulator consist of the input-output pairs  $\{\mathbf{x}_i, \mathbf{y}_i\}$ . As a result, after the training a continuous regression in  $\{\mathbf{x}_i, \mathbf{y}_i\}$  space will be obtained. Neural networks, if constructed large enough, are well suited for regression tasks, and are used as emulators in this work.

Before the training, the data obtained from FluiduM is divided into three different cate-

gories: the training set accounting for 83.3% of the data, the validation, and the test set of 8.3% each. The validation and test set are used to perform a grid search and optimize the model's hyperparameters. In the case of NN, a hyperparameter can be defined as any parameter that cannot be optimized through gradient descent: thus, hyperparameters include the number of hidden layers, the number of nodes per layer, the learning rate, and the activation function, defined in Sec. 5.2. In simple terms, the grid search consists of trying to find the minimal loss function curve for different NN configurations: with this procedure, it was found that the optimal configuration in the present analysis consists of a shallow neural network with three hidden layers with  $\sim 900$  nodes, a learning rate of around 0.01, and a ReLU activation function. For more details on the grid search, see [106].

After the optimization of the hyperparameters, the NN can be trained. To ensure that every parameter has the same weight on the network, the input and output data of the training set are first normalized to  $[-1, +1]$  range. Moreover, to quantify the performance of the trained NN, FluiduM output can be compared to the validation output, as shown in Sec. 6.1.2.

In order to build a NN ensemble,  $M = 100$  different neural networks are trained, each with random initialization and data shuffling. The mean of the ensemble is then constructed by averaging the single NN models  $y_i(\mathbf{x})$ ,

$$y_{\text{emu}}(\mathbf{x}) = \frac{1}{M} \sum_{i=1}^M y_i(\mathbf{x}) \quad (5.15)$$

To compute the model uncertainty, it is important to take into account the correlation among the different neural networks of the ensemble: this correlation introduces a correction factor  $c$  to the standard deviation of the neural network predictions [79],

$$\sigma_{\text{emu}}(\mathbf{x}) = c \cdot \sqrt{\frac{1}{M} \sum_{i=1}^M (y_i(\mathbf{x}) - y_{\text{emu}}(\mathbf{x}))^2} = c \cdot \hat{\sigma}_{\text{emu}}(\mathbf{x}). \quad (5.16)$$

Knowing the output of FluiduM  $y(\mathbf{x})_{\text{FluiduM}}$  and of the emulator  $y_{\text{emu}}(\mathbf{x})$ , the value of  $c$  can be determined by fitting a Student-distribution to  $[y_{\text{FluiduM}}(\mathbf{x}) - y_{\text{emu}}(\mathbf{x})] / \hat{\sigma}_{\text{emu}}(\mathbf{x})$  [79]. In the present analysis,  $c \approx 0.5$ .

With the ensemble mean and the model uncertainty, it is now possible to calculate the posterior probability distributions for each parameter using the Markov-chain Monte Carlo method.

### 5.4.3 MCMC in the present analysis

In order to run the Markov-chain Monte Carlo, the Python library emcee is employed [109], where the logarithmic of the posterior probability is taken as input. From the definition of the posterior and of the likelihood in Eq. 5.2 and 5.6 respectively, the logarithm of the posterior probability can be calculated as,

$$\log(P(\mathbf{x}|\mathbf{Y})) \propto \begin{cases} -\frac{1}{2} [\mathbf{y}_{\text{emu}}(\mathbf{x}) - \mathbf{y}_e]^T \Sigma^{-1} [\mathbf{y}_{\text{emu}}(\mathbf{x}) - \mathbf{y}_e] & \text{if } x_i^{\min} \leq x_i \leq x_i^{\max} \forall i \\ -\infty & \text{otherwise,} \end{cases} \quad (5.17)$$

where  $\mathbf{y}_e$  represents the vector of experimental  $p_T$  spectra,  $\mathbf{y}_{\text{emu}}(\mathbf{x})$  is the vector of emulator model output corresponding to input  $\mathbf{x}$ , and  $\Sigma = \Sigma_{\text{emu}} + \Sigma_e$  is the covariance matrix. The experimental covariance matrix can be constructed by taking into account experimental statistical  $\sigma_{\text{stat}}$  and systematic uncertainties  $\sigma_{\text{syst}}$ . Since no information about the correlations between the experimental uncertainties exists,  $\Sigma_e$  is constructed as a diagonal matrix with entries given by  $\sigma = \sqrt{\sigma_{\text{stat}}^2 + \sigma_{\text{syst}}^2}$ .

The second covariance matrix  $\Sigma_{\text{emu}}$  represents the ensemble covariance and can be computed as,

$$\Sigma_{\text{emu}}^{j,k} = c \cdot \frac{1}{M-1} \sum_{i=1}^M (y_i^j(\mathbf{x}) - y_{\text{emu}}^j(\mathbf{x}))(y_i^k(\mathbf{x}) - y_{\text{emu}}^k(\mathbf{x})), \quad (5.18)$$

where  $y^j$  is the  $j$ th-spectra output value and  $y_{\text{emu}}^j$  its mean ensemble prediction. Notice that the covariance matrix has to be scaled by the correction factor  $c$ .

Using Eq. 5.17 the logarithm of the posterior probability can now be obtained. However,  $P(\mathbf{x}|\mathbf{Y})$  is a  $n$ -dimensional vector: thus, the posterior distribution of a single parameter  $x_i$ , known as the *marginal posterior distribution*, can be calculated integrating out all the remaining parameters. Thus, for example for the parameter  $x_1$ ,

$$P(x_1|\mathbf{Y}) = \int dx_2 \dots dx_n P(\mathbf{x}|\mathbf{Y}). \quad (5.19)$$

The next sections will focus on the results computed by employing the analysis procedure described so far.

# 6 Results and discussion

Heavy quarks represent only a small percentage of the particles of the QGP: thus, the properties of the QCD medium are better inferred by studying light-quark dynamics. In the present analysis, two separate fits on light and on charmed hadrons are performed. The study on light-hadrons  $p_T$  spectra allows us to estimate the hydro model parameters through the Markov-chain Monte Carlo procedure. After fixing the values of the hydro model parameters, the Bayesian inference is applied to charmed-hadrons  $p_T$  spectra, in order to estimate the value of  $D_s T$ . However, via this strategy, several hydro model parameters and  $D_s T$  are not well constrained. For this reason, a simultaneous fit of light and charmed hadrons is later investigated.

## 6.1 Light hadrons

### 6.1.1 FluiduM results

As already remarked in the previous sections, the first five parameters of Table 5.1, are related to the hydrodynamic evolution of the QGP. Following the work in [79], it is possible to estimate the values of these hydro model parameters by studying the invariant yields of light hadrons (i.e. pions, kaons, and protons) produced at freeze-out.

The experimental data of light hadrons are taken from the PHENIX collaboration [81]. At RHIC top energies the baryon chemical potential is  $\mu_B \sim 20$  MeV [90]. Thus, while the antiprotons are all created in the heavy-ion collisions, some of the observed protons at midrapidity may be remnants of the original colliding ions. For this reason, the experimental yields of antiprotons, and, for consistency, of anti-mesons  $K^-$  and  $\pi^-$  are considered here.

Fig. 6.1 shows the comparison between the experimental data and our model for  $2 \cdot 10^4$  configurations. Here, the configuration that minimizes the  $\chi^2$  between the model and the experimental data is highlighted as an orange line. FluiduM correctly describes the experimental yield of pions and of kaons. As for antiprotons, however, the model results seem to overestimate the experimental data for  $p_T < 1$  GeV. This effect can be due to

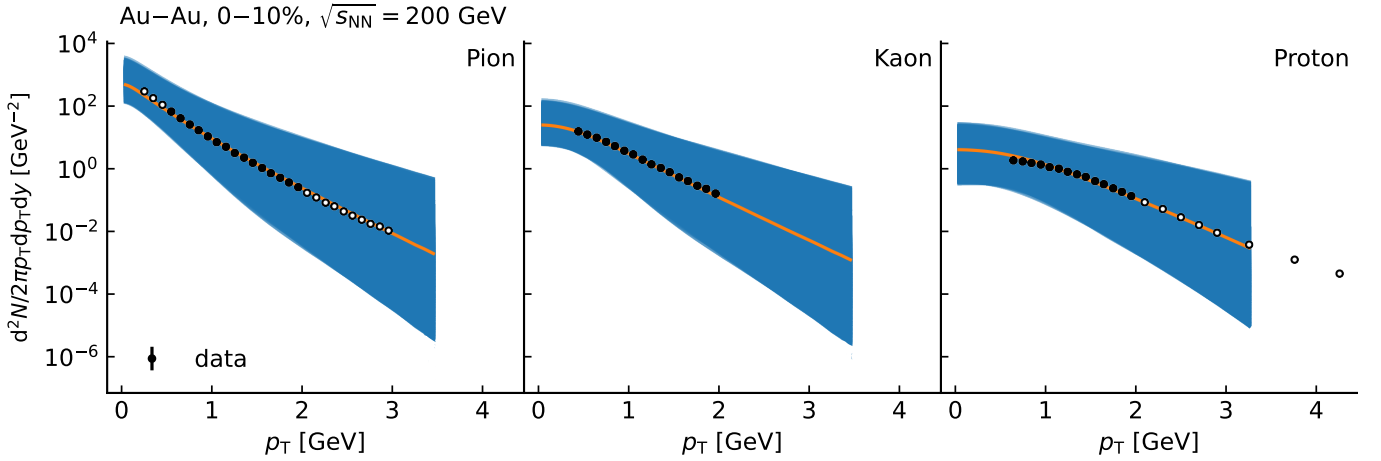


**Figure 6.1:** Comparison between  $n = 2 \cdot 10^4$  transverse momentum spectra generated by FluidM and experimental data of Au – Au collisions at  $\sqrt{s_{NN}} = 200$  GeV for the 0–10 % centrality class, from the PHENIX collaboration [81]. The solid markers show the experimental data that will be used in the MCMC procedure, while the open ones represent the full experimental dataset. The configuration that minimizes the  $\chi^2$  is drawn as an orange line.

the absence of a partial chemical equilibrium phase in the present model. The hadronic phase builds additional radial flow, mostly due to the presence of elastic interactions [29]. Since heavier particles are more affected by the developing radial flows, a depletion at low transverse momentum for protons is expected. Moreover, this effect is not observed in [79], where the partial chemical equilibrium phase was implemented.

Since kaons and pions experimental  $p_T$  spectra are well captured, the present model can be used nonetheless to train the neural network.

### 6.1.2 Neural network validation

Using the FluidM output, an ensemble of 100 NN is built and trained. In order to quantify the performance of the trained neural networks, the FluidM output is compared to the output of the NN. Fig. 6.2 shows the correlation between the  $p_T$  spectra estimated by FluidM and the ones simulated by the ensemble of 100 NN, considering the validation set only. Each point represents a  $p_T$  spectrum value in one experimental  $p_T$  bin for either pions, kaons, or protons in the 0 – 10% centrality class: since the points mostly lie on the bisector, we verify that the NN predictions are strongly correlated to the model predictions, or in other words, the emulator accurately reproduces the FluidM output.

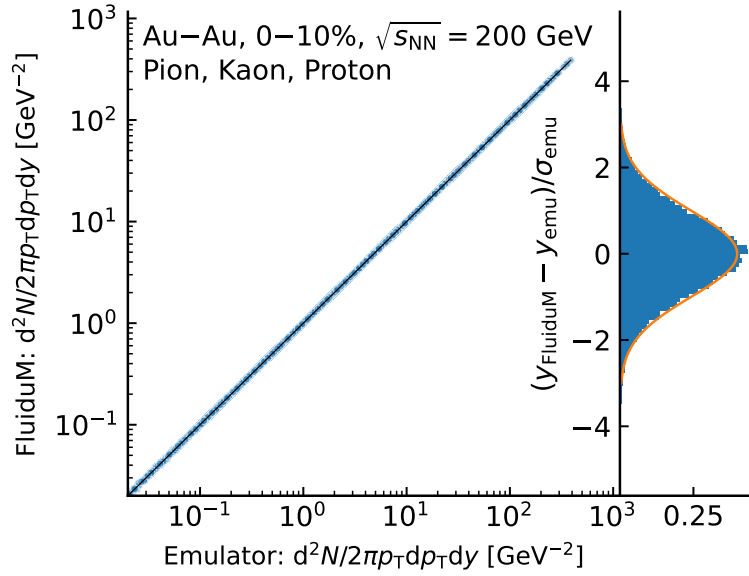


**Figure 6.2:** Correlation between the  $p_T$  spectra values estimated by FluidM and the  $p_T$  spectra simulated by the ensemble of 100 NN, for pions, kaons, and protons in the 0 – 10% centrality class. As a comparison, the bisector is drawn (black line). On the right, the residual distribution is shown, and compared to a standard normal distribution (orange line).

In order to study the accuracy of the NN ensemble, it is also possible to calculate the distribution of the residuals between the emulator output and FluidM, scaled by the neural networks ensemble uncertainty, as depicted in the right side of Fig. 6.2. The residual distribution is centered at zero and is compatible with a Gaussian distribution with zero mean and unitary variance.

Moreover, the prediction error, measured in units of the experimental data uncertainty is of the order of  $(y_{\text{FluiduM}} - y_{\text{emu}}) / \sigma_{\text{exp}} \sim 10^{-3}$ : this level of accuracy is sufficient for the purposes of this study, and allows us to use the NN output in the next steps of the present analysis.

### 6.1.3 MCMC procedure

The  $p_T$  spectra generated by the emulator can now be used to apply the Markov-chain Monte Carlo procedure. In the present work, the vector  $\mathbf{y}_e$  is built considering the experimental data in the low transverse-momentum region, up to  $p_T \leq 2$  GeV. Moreover, in the case of pions a limit of  $p_T > 0.5$  GeV is set. This constraint, also used in [79], is necessary to take into account the observed enhancement of pions at low  $p_T$ , which is

Parameter	Value
Norm	$21.8_{-3.2}^{+2.1}$
$\eta/s$	$0.52_{-0.22}^{+0.29}$
$(\zeta/s)_{\max}$	unconstr.
$\tau_0$ [fm]	$0.70_{-0.39}^{+0.42}$
$T_{\text{fo}}$ [GeV]	$0.135_{-0.001}^{+0.001}$

**Table 6.1:** Posterior parameter estimates. The reported values correspond to the median values and 68% confidence intervals.

believed to have non-hydrodynamic origins [110].

In Fig. 6.3 the distribution of the marginal posteriors is shown for the hydro model parameters. In the diagonal panels, the marginal distribution of each parameter is shown, whereas the off-diagonal panels depict the correlations among pairs of parameters. A summary of the best-estimated values of the hydro model parameters is reported in Table 6.1.

The MCMC procedure manages to constrain the value of the normalization constant Norm and of the freeze-out temperature  $T_{\text{fo}}$ , which are distributed as a Gaussian-like shape around their most probable value. The value of the freeze-out temperature  $T_{\text{fo}} = 0.135_{-0.001}^{+0.001}$  GeV is within the chemical freeze-out temperature determined by statistical models,  $T_{\text{chem}} \approx 0.170$  GeV [111, 112], and the kinetic freeze-out temperature  $T_{\text{kin}} \approx 0.120$  GeV extracted using the blast-wave model fit to experimental data [113]. The normalization constant is a system-dependent quantity: in accordance with the expectations, its value  $\text{Norm} = 21.8_{-3.2}^{+2.1}$  is lower than the one predicted at LHC energies, where  $\text{Norm} = 36.0_{-3.6}^{+3.1}$  [79].

The distribution of  $\tau_0$  results too large to draw any conclusion on its best-estimated value: as a matter of fact, since  $\tau_0 = 0.70_{-0.39}^{+0.42}$  fm, its relative error is more than 50%. Similarly to what is observed in [79], the transport coefficients  $\eta/s$  and  $(\zeta/s)_{\max}$  are not well constrained by the current analysis. On one hand, the shear viscosity over entropy ratio seems to favor values beyond the upper bound of the allowed interval. The same behavior is observed when trying to increase the upper range up to  $\eta/s = 3$ , and it is thus not attributable to the value of the bound itself. The bulk viscosity over entropy ratio, on the other hand, hits the lower bound of its prior interval: in this case, even if theoretically possible, extending the lower range of  $(\zeta/s)_{\max}$  causes numerical problems in the FluiduM simulation, and it is thus not feasible at the moment. For this reason, we

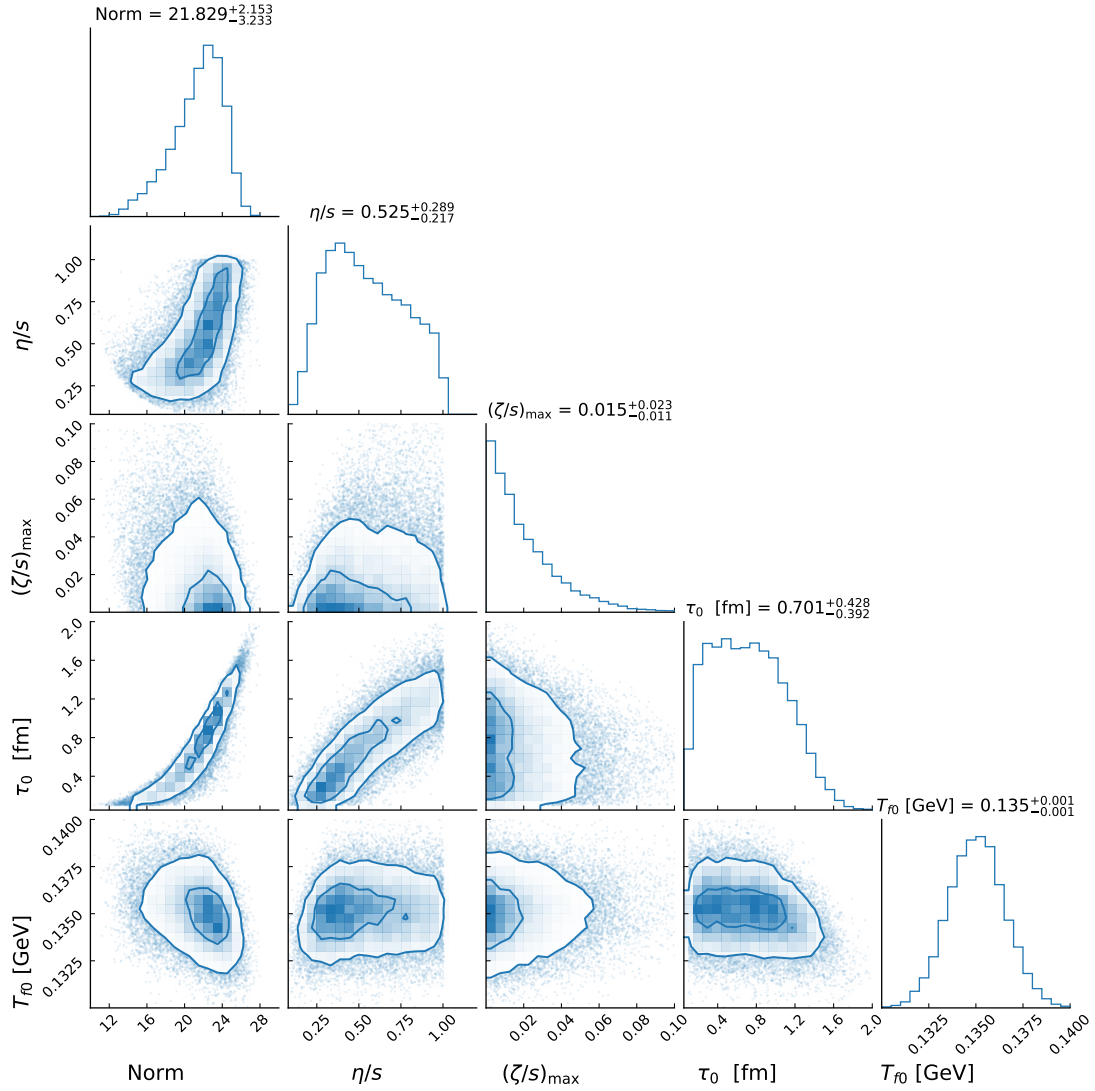


**Figure 6.3:** Marginal distributions of the hydro model parameters obtained employing Bayesian inference. In the diagonal panels, the marginal distribution of each parameter is shown, whereas the off-diagonal panels depict the correlations among pairs of parameters. The two contours represent  $1\sigma$  and  $2\sigma$  confidence level.

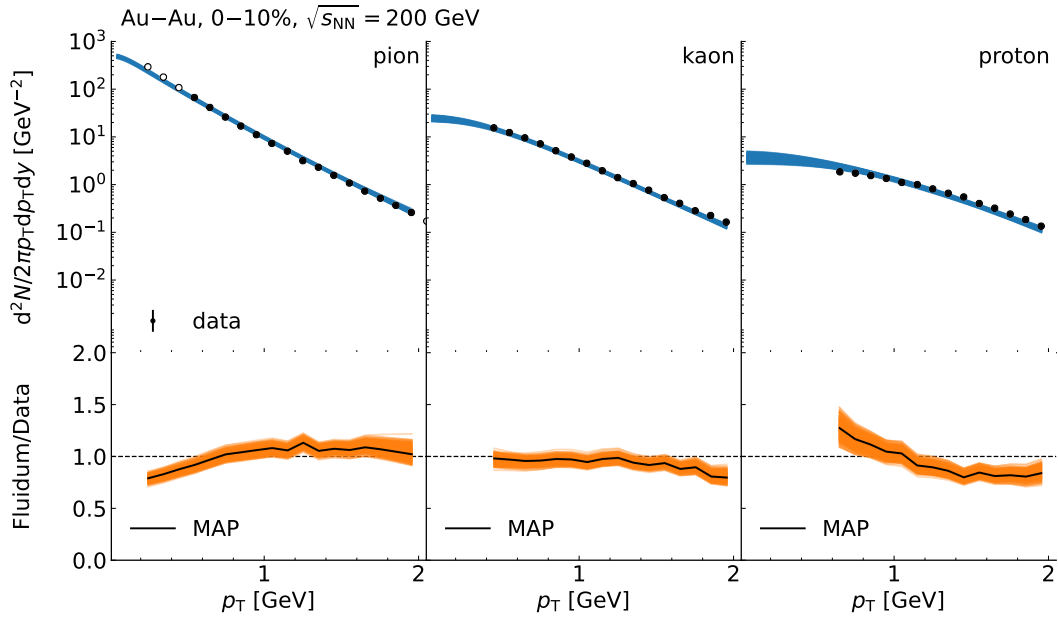


**Figure 6.4:** Top panels: comparison between  $n = 400$  transverse momentum spectra generated by FluiduM from the marginal distributions and experimental data of Au – Au collisions at  $\sqrt{s_{NN}} = 200$  GeV for the 0–10 % centrality class, from the PHENIX collaboration [81]. The solid markers show the experimental data used in MCMC the procedure, while the open ones represent the full experimental dataset. Bottom panels: ratio between the FluiduM prediction and experimental data.

consider  $(\zeta/s)_{\max}$  unconstrained, as reported in Table 6.1. The value of  $(\zeta/s)_{\max}$  used as input for the charmed-hadrons study will be the one automatically estimated by the MCMC simulation: however, we remark here that this value does not represent a best estimate, given the current shape of the marginal distribution.

In conclusion, several hydro parameters are not well constrained by the MCMC procedure. However, it is important to underline that this work represents a preliminary study of Bayesian analysis applied to RHIC top energies. Systematically varying the ranges of the hydro parameters and employing more centrality classes will presumably allow us to better estimate of the hydro model parameters. Moreover, the difficulty of constraining the value of the  $\eta/s$  and of  $(\zeta/s)_{\max}$  can be attributed to the limited sensitivity of the  $p_T$  spectrum to the transport coefficients. In order to address this issue, it will be possible in the future to employ additional observables, such as the anisotropic flow coefficients  $v_n$ . In order to study the posterior  $p_T$  spectra, it is possible to sample  $n = 400$  random parameter configurations from the marginal distributions and use them as new input for FluiduM simulation. The top panel of Fig. 6.4 shows that the FluiduM predictions

sampled from the marginal distributions are significantly more constrained than the original prior  $p_T$  spectra. Moreover, the ratio between Fluid $u$ M and the experimental data is shown in the bottom panel: here, the deviation between the model results and the data is between 5% – 10%, except for low- $p_T$  protons, where a deviation of  $\sim 30\%$  is observed. In this case, this result is attributable to the absence of a chemical equilibrium phase in the current model. The Maximum A Posteriori (MAP) estimate, which is the configuration that maximizes the posterior probability, is shown as a black line. The MAP can be considered as the optimal posterior configuration, and in the present case,  $\tilde{\chi}_{\text{MAP}}^2 \sim 0.5$ . These results prove that, even if several hydro model parameters are not currently constrained, the present model captures well the experimental  $p_T$  spectra.

## 6.2 Charmed hadrons

The study on the light-flavor hadrons served as a starting point for the charmed-hadrons analysis. Even if several hydro model parameters are not well constrained, the level of accuracy reached can be considered, as for now, sufficient for the main purpose of our work, which is the study of heavy-flavor hadrons and of  $D_s T$ . Therefore, the charmed hadrons  $p_T$  spectra can be generated by using the median values of the hydro model parameters reported in Table 6.1. In Fig. 6.5 the Fluid $u$ M results varying the value of  $D_s T$  from 0 to 0.5 are shown. Since the only available experimental data of  $J/\psi$  are in the centrality class 0 – 20%, we will limit our study to  $D$  mesons in the centrality class 0 – 10%. The prior bands of  $D^0$  and  $D_s^+$  are already very constrained around the experimental data, and they fail to correctly describe the  $D^0$  experimental data for  $p_T > 3$  GeV. This result arises because the hydro model parameters are fixed to their median values, and we do not consider any error associated with them. In order to account for the uncertainty related to every hydro model parameter, it would be necessary to perform an error propagation to the charmed hadron momentum spectra. Employing prior distributions that are so constrained around the experimental data could pose several questions on the applicability of the present procedure. However, as already stressed, this work represents a preliminary study, and we aim to test the Bayesian procedure on charmed hadrons. Therefore, as for now, we can employ the current model results to train the NN.

After building the emulator using an ensemble of 100 neural networks, the Markov-chain Monte Carlo procedure is applied. In this case, we limit to  $p_T < 4$  GeV, where the hydrodynamic description of heavy quarks is assumed to be valid. Fig. 6.6 depicts the marginal distribution of  $D_s T$  obtained from the MCMC analysis. From the shape of the

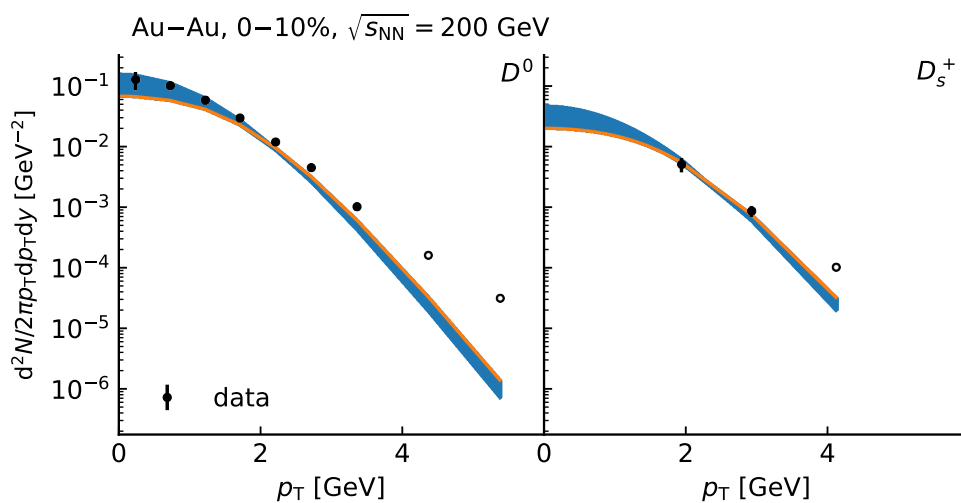


**Figure 6.5:**  $n = 2 \cdot 10^4$  charmed hadrons  $p_T$  spectra generated by Fluid $u$ M fixing the hydro parameters according to the procedure presented in Sec. 6.1, and experimental data of Au – Au collisions at  $\sqrt{s_{NN}} = 200$  GeV for the 0–10 % centrality class, from the STAR collaboration [87, 88]. The solid markers show the experimental data that will be used in the MCMC procedure, while the open ones represent the full experimental dataset. The configuration that minimizes the  $\chi^2$  is drawn as an orange line.

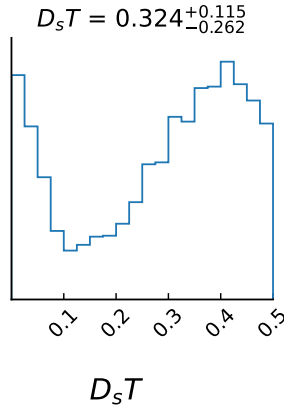


**Figure 6.6:** Posterior distribution of  $D_s T$  obtained using the median values of the hydro model parameters.

distribution, it is clear that the current procedure is not able to constrain the value of the charm spatial diffusion coefficient multiplied by the temperature. As a matter of fact, the  $D_s T$  marginal distribution is characterized by two peaks, which respectively hit the upper and the lower bound of the prior interval considered. It is not convenient in the present work to increase the searching region of  $D_s T$ . As already stressed in Sec. 4.3.1 large values of the HQ spatial diffusion coefficient entail large corrections  $\delta f^{\text{diffusion}}$ . Thus, by using  $D_s T > 0.5$ , we would produce  $p_T$  spectra which need large out-of-equilibrium corrections. Since these corrections are neglected here, the current framework cannot correctly describe the spectra corresponding to large  $D_s T$  values. Thus, we will limit our analysis to  $0 < D_s T < 0.5$ , which still represents a reasonable range according to IQCD predictions [85].

The invariant spectra of charmed hadrons obtained by sampling the marginal distribution of  $D_s T$  are shown in Fig. 6.7. Since the value of  $D_s T$  is not well constrained in the present analysis, the width of the total posterior band does not differ much from the one of the prior  $p_T$  spectra in Fig. 6.5. Thus, as expected, the present procedure does not allow us to provide a more precise description of the momentum spectra of charmed hadrons.

It is important to remark that here we employed the median values of the hydro model parameters, even if several parameters are not well constrained by the analysis on light hadrons. Moreover, as already stressed, it would be necessary to propagate the uncertainties of the hydro model parameters to the estimate of  $D_s T$ . These issues will be addressed in the near future, while for now, it is possible to test a different fit procedure,

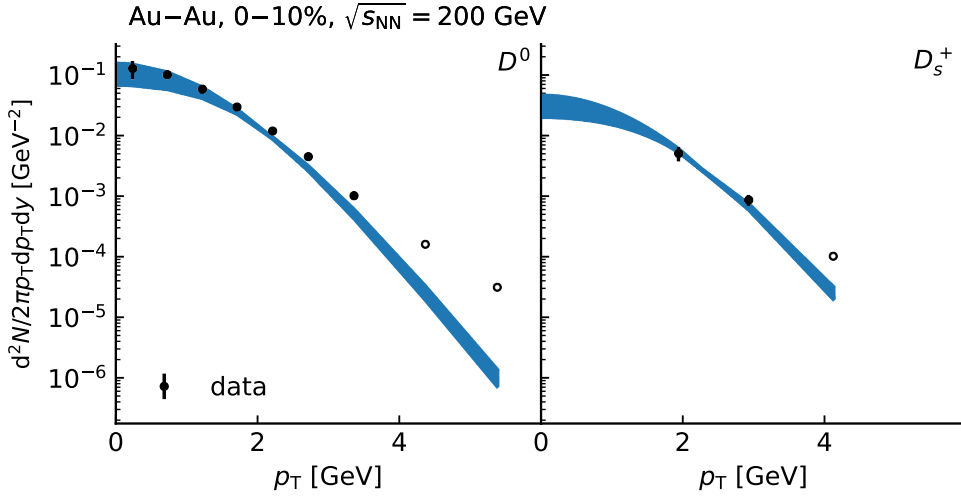


**Figure 6.7:**  $n = 400$  charmed hadrons  $p_T$  spectra generated sampling from  $D_s T$  marginal distributions. The experimental data of Au – Au collisions at  $\sqrt{s_{\text{NN}}} = 200$  GeV in the 0–10 % centrality class are taken from the STAR collaboration [87, 88]. The solid markers show the experimental data used in MCMC the procedure, while the open ones represent the full experimental dataset.

presented in the next section.

### 6.3 Global fit

An alternative approach is to apply the Bayesian inference considering both the light and charmed hadrons simultaneously. Therefore, the hydro model parameters and  $D_s T$  will be estimated at the same time. Since the value of the HQ spatial diffusion coefficient does not influence the dynamics of light hadrons, their prior  $p_T$  spectra do not differ from the ones shown in Fig. 6.1. In Fig. 6.8 the invariant yields of charmed hadrons are reported. Compared to the prior spectra shown in Sec. 6.2, the current invariant yields span over a broader range, since all the model parameters are varied at the same time. This result represents a good indication that the prior distributions span a large range of  $p_T$  spectra, and can be used to apply Bayesian inference. Thus, the light and the charmed-hadrons momentum spectra are used together to train the neural networks. Since in this case the FluiduM simulation depends on six parameters and five particle species are studied, a new grid search is performed. Here the configuration that minimizes the loss function consists of neural networks with three hidden layers and  $\sim 1000$

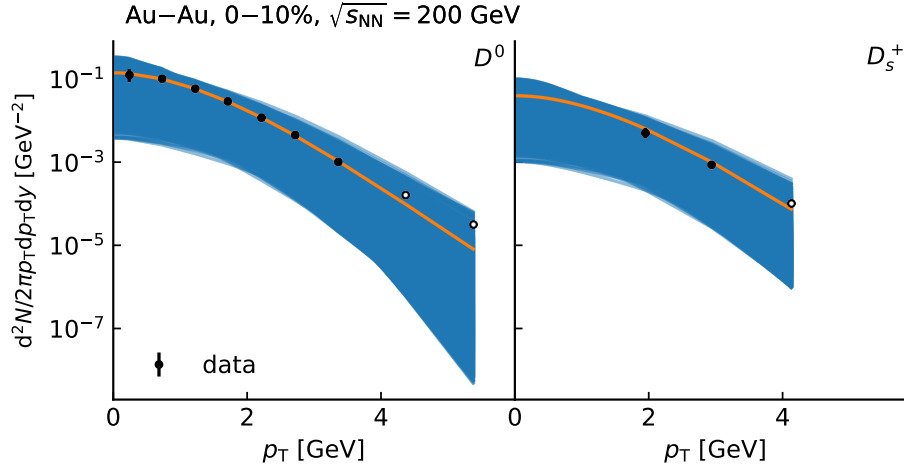


**Figure 6.8:**  $n = 2 \cdot 10^4$  charmed hadrons  $p_T$  spectra generated by Fluid $u$ M varying all the model parameters and experimental data of Au–Au collisions at  $\sqrt{s_{\text{NN}}} = 200$  GeV for the 0–10 % centrality class from the STAR collaboration [87, 88]. The solid markers show the experimental data that will be used in the MCMC procedure, while the open ones represent the full experimental dataset. The configuration that minimizes the  $\chi^2$  is drawn as an orange line.

nodes per layer. Moreover, the NN validation does not qualitatively differ from the results shown in Sec. 6.1.2.

After emulating the Fluid $u$ M output, the MCMC procedure is applied. In Fig. 6.9 the marginal distributions of the model parameters are shown. As already mentioned, the hydro model parameters should mostly depend on the light-quark dynamics, since they represent the majority of the particles of the QGP. However, the simultaneous fit of light and charmed hadrons affects the marginal distribution of several hydro model parameters. The thermalization time seems now to be better constrained: since  $\tau_0 = 1.04_{-0.26}^{+0.24}$  fm its relative error is more than halved with respect to fitting light hadrons only. On the other hand, the distribution of the shear viscosity over the entropy ratio differs from the one shown in Fig. 6.3. In the present case, the distribution hits the upper bound of its range and hence we consider  $\eta/s$  unconstrained.

In order to understand if and to what extent the charmed hadrons  $p_T$  spectra really influence the estimation of the hydro model parameters, and if the current procedure is preferable over the separate fit of light and charmed hadrons, further investigations will be needed in the future.

The marginal distribution of  $D_s T$  hits the upper bound of its range. The tendency of

$D_s T$  to favor high values can be traced back to the absence of  $\delta f^{\text{diffusion}}$ . The charm multiplicity has a non-physical dependence on  $D_s T$ , and large values of  $D_s T$  translate into large multiplicities. Since the majority of prior distributions shown in Fig. 6.8 are below the experimental data, the configurations with higher multiplicity (and hence higher  $D_s T$ ) tend to be preferred by the MCMC simulation. By simultaneously fitting light and heavy hadrons, it is not necessary to propagate the uncertainty of the hydro parameters to the error of  $D_s T$ . Moreover, the global fit procedure will allow us to study in the future if the hydro model parameters influence the value of  $D_s T$ , employing the pair correlations given by the MCMC procedure.

The posterior momentum spectra of charmed hadrons (Fig. 6.10) describe the experimental data at  $p_T < 4$  GeV. Even if these posteriors do not seem more constrained than the posteriors of Sec. 6.2, it is necessary to remark that here all the model parameters are varied, and the initial prior distributions were very spread around the experimental data.

This work represents the first application of the Bayesian approach to the study of heavy quarks. Therefore, even if the results shown here are only preliminary, they serve as a fundamental proof of concept for applying Bayesian analysis to charmed hadrons, in order to put constraints on the value of  $D_s T$ . Systematic studies in the future will allow us to provide valuable insights into the properties of heavy quarks in the QGP.

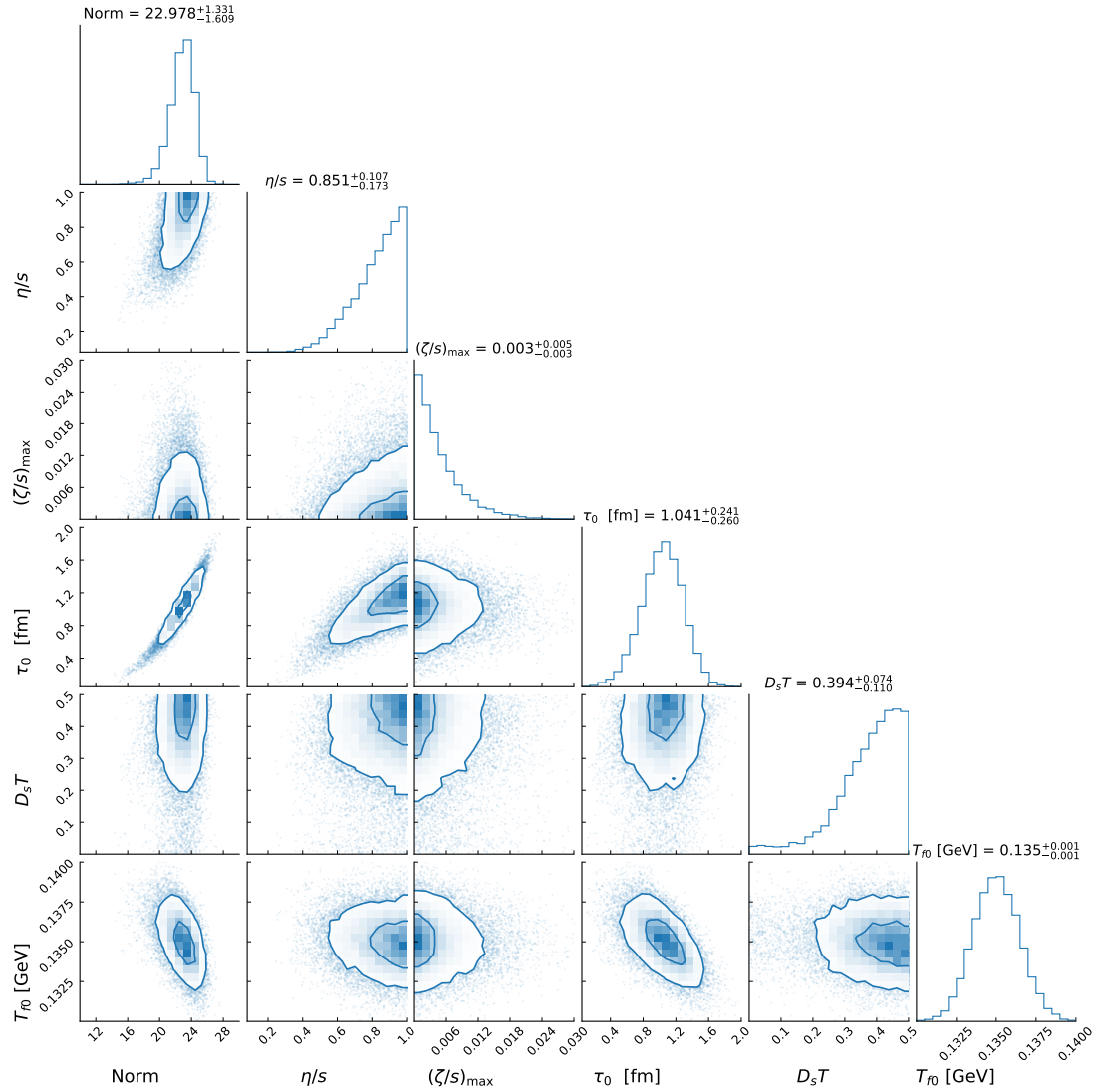


**Figure 6.9:** Marginal distribution of all parameters, obtained employing Bayesian inference. In the diagonal panels, the marginal distributions of each model parameter are shown, whereas the off-diagonal panels depict the correlations among pairs of model parameters.

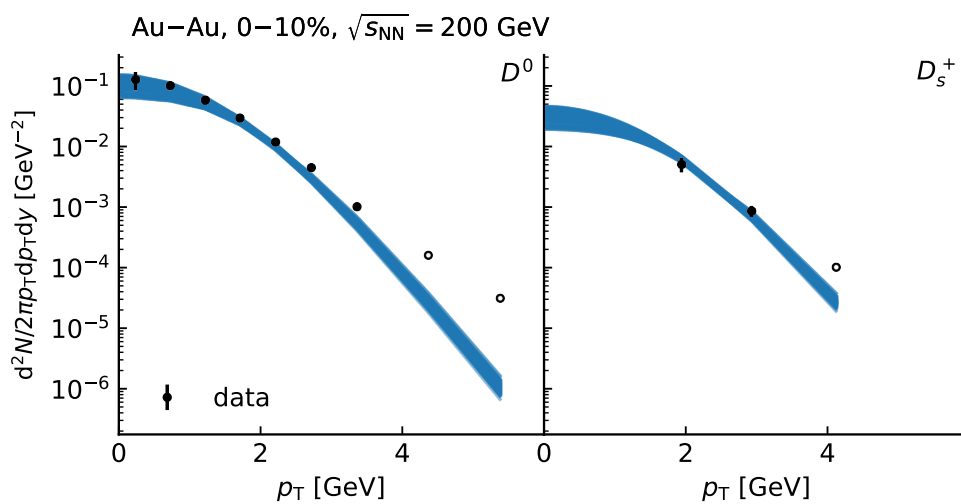


**Figure 6.10:**  $n = 400$  charmed hadrons  $p_T$  spectra spectra generated sampling from all model marginal distributions. The experimental data of Au – Au collisions at  $\sqrt{s_{NN}} = 200$  GeV in the 0–10 % centrality class are taken from the STAR collaboration [87, 88]. The solid markers show the experimental data used in MCMC the procedure, while the open ones represent the full experimental dataset.

## 7 Conclusions and outlook

In this thesis, the applicability of a fluid-dynamic approach to heavy-quark dynamics at RHIC energies of  $\sqrt{s_{\text{NN}}} = 200$  GeV was explored, and a Bayesian analysis to estimate the heavy-quark spatial diffusion coefficient multiplied by the temperature  $D_s T$  was applied. Heavy quarks represent essential probes to study the QGP, since they are mainly produced in the initial hard scattering, and experience the entire evolution of the fireball. Due to their large mass, HQ propagation within the QGP is canonically treated using a Brownian-like motion. However, motivated by studies on the charmed-hadron elliptic flow [72], a fluid-dynamic approach to describe heavy quarks in the QGP was developed in [69]. This approach is valid under the assumption that low- $p_{\text{T}}$  heavy quarks interact enough with the QGP, and approach local thermal equilibrium within the lifetime of the QGP, as verified for LHC energies [75]. The thermalization process is highly dependent on the collision energy: thus a natural question is if HQ can still be described via fluid-dynamic equations even at lower-temperature QGP states, as the ones produced at RHIC in Au – Au collisions at  $\sqrt{s_{\text{NN}}} = 200$  GeV.

After modeling the initial QGP state, it was estimated that  $\sim 1.5$  charm quark pairs are produced at RHIC per event per unit of rapidity. This value is in full agreement with the predictions of statistical models [78]. To estimate whether it is possible for the charm quarks to be described by fluid dynamics within an expanding medium, the relaxation time  $\tau_n$  of charm was compared with the expansion time  $\tau_{\text{exp}}$  of the fluid, using the simplified model of a Bjorken expansion. For most of the values of the heavy-quark spatial diffusion coefficient multiplied by the temperature  $D_s T$ , it was found that  $\tau_n \ll \tau_{\text{exp}}$ , supporting a fast-thermalization picture also at RHIC top energies. The applicability of the fluid-dynamics approach was further explored by studying charmed-hadron invariant yields. Our model captures well the experimental data of  $D^0$ ,  $D_s^+$  and  $J/\psi$  mesons in the low-transverse momentum region,  $p_{\text{T}} < 4$  GeV, measured by the STAR collaboration. These results motivated us to apply a Bayesian parameter estimation on charmed hadrons, to estimate the value of the HQ spatial diffusion coefficient multiplied by the temperature  $D_s T$ . The framework used closely follows the one developed in [79], and employs

neural networks as emulator and Markov-chain Monte Carlo simulations. In order to fix the coefficients related to the QGP hydrodynamic, a fit on light-hadrons  $p_T$  spectra was first performed. However, the current procedure is not able to constrain well the values of several hydro model parameters, such as the initial thermalization time and the transport coefficients. Since the present analysis represents a preliminary study of the Bayesian approach applied at RHIC energies, the accuracy reached here was considered sufficient for this test phase.

The hydro parameters' median values were used as input for the charmed-hadron studies. Applying the MCMC procedure to their  $p_T$  spectra it was found that the current analysis is not able to set any constraint on the value of  $D_s T$ . Moreover, applying two separate fits for light and heavy hadrons raises several questions, such as the propagation of hydro model parameter errors to the estimate of  $D_s T$ .

As an alternative approach, a fit of light and heavy hadrons was simultaneously performed. In this case, the thermalization time is well constrained, and the errors associated with the hydro model parameters are in general smaller. In the future, we will need to investigate whether charmed hadrons spectra influence the estimation of the hydro model parameters. Moreover, it was observed that the  $D_s T$  marginalized distribution tends to favor values close to the upper bound of its prior distribution: this behavior can be traced back to the absence of  $\delta f^{\text{diffusion}}$  corrections at the freeze-out.

This work represents the first study on the Bayesian analysis applied to the HQ dynamics. Even if the value of  $D_s T$  was not constrained here, the results shown are very promising and motivate us to further investigations.

## 7.1 Outlook

In the next studies, it will be possible to focus on a robust estimation of the value of the HQ spatial diffusion coefficient multiplied by the temperature. As already stressed, in the present work we neglect the charm out-of-equilibrium corrections at the freeze-out. However, assuming  $\delta f^{\text{diffusion}} = 0$  entails a non-physical dependence of the charm multiplicity on the value of HQ spatial diffusion coefficient: this reduces the ranges of  $D_s T$  that can be probed, and can introduce a bias on the value of  $D_s T$  extracted from the Bayesian procedure. The computation of the out-of-equilibrium corrections results therefore of priority importance, and to address the problem a maximum-entropy approach [114] is currently under study.

Moreover, as for the case of  $\eta/s$  and  $(\zeta/s)_{\text{max}}$ , it is possible that the  $p_T$  spectrum is

not sensitive enough to  $D_s T$ . Therefore, the anisotropic flow coefficients, which are more sensitive to the medium properties, may play a fundamental role in the future in inferring the value of  $D_s T$ . The study on the anisotropic coefficients will also allow more precise results on the transport coefficients at RHIC top energies.

In the present analysis, due to the experimental data availability, the fit on charmed hadrons included only two particle species in a single centrality class 0 – 10%: the difficulty of constrain  $D_s T$  value could also be due to the limited amount of experimental data employed. Within the Fluid $u$ M framework, it is straightforward to extend this work to the LHC: here the larger amount of available experimental data could allow us for a better estimate of  $D_s T$ .

Moreover, we assumed here that the value of  $D_s T$  remains constant throughout the evolution of the fireball. However, recent lQCD studies [85] show a dependence of  $D_s T$  on the medium temperature. A first approach to address this point could be to consider a linear dependence of  $D_s T$  with the temperature, in order to mimic the trend observed by lQCD calculations.

In the future, it will be possible to investigate whether the fluid-dynamic approach to HQ still holds for lower collision energies, down to  $\mathcal{O}(10 \text{ GeV})$ . Under these experimental conditions, since  $\mu_B \gg 0$ , a conserved baryon current needs to be added and evolved within the Fluid $u$ M framework.

Finally, our study can in principle be extended to the bottom quarks sector as well. Due to their larger mass, bottom quarks need more time to thermalize with the QGP, and a fluid-dynamic description results even more complicated than for charm quarks. In [69] it was shown that  $b$  quark might thermalize in the late stages of the fireball evolution, possibly opening up a new way to investigate heavy-quark dynamics in the QGP.

## Acknowledgments

This entire thesis work would have never been possible without the help and support of many people. First of all, I want to thank my guardian angel, Federica Capellino, who introduced me to the magic world of heavy quarks. You were always ready to answer my stupid questions (even from China!), review my presentations, and call me for every doubt I had. With your energy, passion, and kindness you are a constant inspiration for me.

Thanks to prof. Silvia Masciocchi, who gave me the opportunity to work on this fantastic topic (now and even in the future), and always believed in me. Thanks to Eduardo Grossi, the Julia master, who spent Friday evenings just to explain to me what broadcasting is, always with his kindness and patience. Thanks to Andrea Dubla, for all the things you taught me, your suggestions, and the patience you had to always help me. Thanks to Rafet Kavak, who shared with me the adventure of doing phenomenology, and especially shared with me all the magic tricks of the clusters he knows. I wish you all the best in America. We will miss you. Thanks to Andreas Kirchner who was always ready to answer my questions, and reviewed the German of the abstract.

I cannot forget to thank all the people I shared the office with during this year. You made me feel comfortable from the first day I arrived to the last. Thanks for the lunch we spent together, the card games we played, the Eurovisions, and the retreats. You are much more than just office colleagues. So thanks to Alica, Anouk, Bent, Chris, Fabian, Frosso, Johannes, Maurice, Mika, Phil, Philip, Rafet (again!), Simon, Sarah, and Tim. Thanks to my friends Nikhil and Anant, for the Indian movies we watched, the frozen pizzas with secret cooking strategy, and the (bad) billiard games we played. You tried your best to teach me how to play, and you miserably failed. Thanks to the "lil men" people, with whom I shared hikes in random places and beers. You made Heidelberg feel more like home. Thanks to my roommate Polina, for the pancakes we made, the dinners with "just sandwich", and the laughs at night even when "the English translation office was closed". I hope we will be able to share the apartment again in the future. Thanks to the people of the gardening group: I didn't learn almost anything about gardening, but you always helped me to learn some German (and some French, some Ukrainian, some Parsi...).

Thanks to my family who supported me during these two years in Germany. Especially thanks to my sister, who takes care of me as if I am 10 (but in reality I need it). Thanks to my best friends Ruby and Matt, who were ready to call me whenever I needed them

(well, at least Ruby was), and developed the soft skill to *su(o)opportarmi sempre*. Vi voglio bene. Thanks to la terapia di trio, Elisa and Elisabetta, for the hours (they felt like weeks) spent deciding where to go to have dinner (colpa di Elisabetta!), and the nights spent watching *c'è posta per te* (they felt like years).

Thanks to Lia, who became a sister more than a friend to me, with her infinite wisdom and care. Thanks to my university colleagues, the people dell'aula F, for being ready to have dinner and "svuotare le cucine dell'all you can eat" whenever I come back to Italy. Thanks to my friends of Adotta uno Scipione: we all live in different places and we meet three times per year now that we study at the university, but it always feels like we just finished high school when we meet for New Year's Eve and we bully *masci* again. Grazie ragazzi. Thanks to the fantastic people I met at Desy, and for the summer we spent together. Especially thanks to Giulia, for the evenings spent reading Greg together, even if "das Leben ist kein Ponyhof".

And last but not least thanks to Simone, who stood by my side from the first day I started my master's to the very last one. Without knowing anything of Julia and of heavy flavor physics (after all, you are **just** an astrophysicist) you spent hours trying to debug codes with me and discuss about physics. You are the person I am growing up with, you are MY person, and we both know that you deserve this master more than me. As once you told me, *ti posso solo dire minä rakastan sinua*.

# Bibliography

- [1] A. Zannoni. *On the Quantization of the Monoatomic Ideal Gas*. 1999. arXiv: cond-mat/9912229 [cond-mat.stat-mech].
- [2] S. Bose. “Plancks Gesetz und Lichtquantenhypothese”. In: *Zeitschrift für Physik* 26.1 (July 1924), pp. 178–181. DOI: 10.1007/BF01327326.
- [3] P.W. Higgs. “Broken symmetries, massless particles and gauge fields”. In: *Physics Letters* 12.2 (Sept. 1964), pp. 132–133. DOI: 10.1016/0031-9163(64)91136-9.
- [4] F. Englert and R. Brout. “Broken Symmetry and the Mass of Gauge Vector Mesons”. In: *Phys. Rev. Lett.* 13.9 (Aug. 1964), pp. 321–323. DOI: 10.1103/PhysRevLett.13.321.
- [5] S. Mertens. “Direct Neutrino Mass Experiments”. In: *Journal of Physics: Conference Series* 718 (May 2016), p. 022013. DOI: 10.1088/1742-6596/718/2/022013.
- [6] V. Trimble. “Existence and Nature of Dark Matter in the Universe”. In: *Annual Review of Astronomy and Astrophysics* 25.1 (Sept. 1987), pp. 425–472. DOI: 10.1146/annurev.aa.25.090187.002233.
- [7] M. Gell-Mann. “Symmetries of Baryons and Mesons”. In: *Phys. Rev.* 125.3 (Feb. 1962). Ed. by American Physical Society, pp. 1067–1084. DOI: 10.1103/PhysRev.125.1067.
- [8] W. Hollik. *Quantum field theory and the Standard Model*. 2010. arXiv: 1012.3883 [hep-ph].
- [9] M. Thomson. *Modern Particle Physics*. Cambridge University Press, 2013.
- [10] H. D. Politzer. “Reliable Perturbative Results for Strong Interactions?” In: *Phys. Rev. Lett.* 30.26 (June 1973). Ed. by J. C. Taylor, pp. 1346–1349. DOI: 10.1103/PhysRevLett.30.1346.
- [11] D. J. Gross and F. Wilczek. “Ultraviolet Behavior of Nonabelian Gauge Theories”. In: *Phys. Rev. Lett.* 30.26 (June 1973). Ed. by J. C. Taylor, pp. 343–346. DOI: 10.1103/PhysRevLett.30.1343.

- [12] P. A. M. Dirac. “Discussion of the infinite distribution of electrons in the theory of the positron”. In: *Mathematical Proceedings of the Cambridge Philosophical Society* 30.2 (Apr. 1934), pp. 150–163. DOI: 10.1017/S030500410001656X.
- [13] D. J. Gross. “Twenty five years of asymptotic freedom”. In: *Nucl. Phys. B Proc. Suppl.* 74.1 (July 1999), pp. 426–446. DOI: 10.1016/S0920-5632(99)00208-X.
- [14] A. Deur et al. “The QCD running coupling”. In: *Progress in Particle and Nuclear Physics* 90 (Sept. 2016), pp. 1–74. DOI: 10.1016/j.ppnp.2016.04.003.
- [15] S Bethke. “Determination of the QCD coupling  $\alpha_s$ ”. In: *Journal of Physics G: Nuclear and Particle Physics* 26.7 (July 2000), R27. DOI: 10.1088/0954-3899/26/7/201.
- [16] K. G. Wilson. “Confinement of quarks”. In: *Phys. Rev. D* 10.8 (Oct. 1974), pp. 2445–2459. DOI: 10.1103/PhysRevD.10.2445.
- [17] M. Tanabashi et al. “Review of Particle Physics”. In: *Phys. Rev. D* 98.3 (Aug. 2018), p. 030001. DOI: 10.1103/PhysRevD.98.030001.
- [18] E. Eichten et al. “Spectrum of Charmed Quark-Antiquark Bound State”. In: *Phys. Rev. Lett.* 34.6 (June 1975). Ed. by American Physical Society, pp. 369–372. DOI: 10.1103/PhysRevLett.34.369.
- [19] W.A. Zajc. “The Fluid Nature of Quark-Gluon Plasma”. In: *Nuclear Physics A* 805.1–4 (June 2008), pp. 283c–294c. DOI: 10.1016/j.nuclphysa.2008.02.285.
- [20] D. Boyanovsky, H. J. de Vega, and D. J. Schwarz. “Phase transitions in the early and the present universe”. In: *Ann. Rev. Nucl. Part. Sci.* 56.3 (Nov. 2006), pp. 441–500. DOI: 10.1146/annurev.nucl.56.080805.140539.
- [21] K. Fukushima and T. Hatsuda. “The phase diagram of dense QCD”. In: *Reports on Progress in Physics* 74.1 (Dec. 2010), p. 014001. DOI: 10.1088/0034-4885/74/1/014001.
- [22] C. Ratti. “Lattice QCD and heavy ion collisions: a review of recent progress”. In: *Reports on Progress in Physics* 81.8 (July 2018), p. 084301. DOI: 10.1088/1361-6633/aabb9.
- [23] P. Steinbrecher. “The QCD crossover at zero and non-zero baryon densities from Lattice QCD”. In: *Nuclear Physics A* 982 (Feb. 2019), pp. 847–850. DOI: 10.1016/j.nuclphysa.2018.08.025.

- [24] P. Braun-Munzinger and B. Dönigus. “Loosely-bound objects produced in nuclear collisions at the LHC”. In: *Nuclear Physics A* 987 (Feb. 2019), pp. 144–201. DOI: 10.1016/j.nuclphysa.2019.02.006.
- [25] J.N. Guenther. “Overview of the QCD phase diagram”. In: *Eur. Phys. J. A* 57.136 (Apr. 2021). DOI: 10.1140/epja/s10050-021-00354-6.
- [26] D. H. Rischke. “The quark–gluon plasma in equilibrium”. In: *Progress in Particle and Nuclear Physics* 52.1 (Mar. 2004), pp. 197–296. DOI: 10.1016/j.pnpnp.2003.09.002.
- [27] T. Nonaka. “Conserved Charge Fluctuations from RHIC BES and FXT”. In: *Universe* 10.1 (Jan. 2024). DOI: 10.3390/universe10010049.
- [28] K. Aamodt et al. “Two-pion Bose–Einstein correlations in central Pb–Pb collisions at  $\sqrt{s_{NN}} = 2.76$  TeV”. In: *Physics Letters B* 696.4 (Dec. 2011), pp. 328–337. DOI: 10.1016/j.physletb.2010.12.053.
- [29] B. Abelev et al. “Pion, Kaon, and Proton Production in Central Pb-Pb Collisions at  $\sqrt{s_{NN}} = 2.76$  TeV”. In: *Phys. Rev. Lett.* 109.25 (Dec. 2012), p. 252301. DOI: 10.1103/PhysRevLett.109.252301.
- [30] S. Floerchinger. “A very brief Introduction to Heavy Ion Physics”. In: *Proceedings of the 2015 European School of High-Energy Physics*. Ed. by M. Mulders and G. Zanderigh. 4. 2017, p. 141. DOI: 10.23730/CYRSP-2017-004.141.
- [31] R. Stock. “ROY GLAUBER: In Memoriam the Glauber Model in High Energy Nucleus-Nucleus Collisions”. In: *The XVIII International Conference on Strangeness in Quark Matter (SQM 2019)*. Ed. by D. Elia et al. Springer International Publishing, Oct. 2020, pp. 3–12. DOI: 10.1007/978-3-030-53448-6\_1.
- [32] K. H. Ackermann et al. “Elliptic Flow in Au+Au Collisions at  $\sqrt{s_{NN}} = 130$  GeV”. In: *Phys. Rev. Lett.* 86.3 (Jan. 2001), pp. 402–407. DOI: 10.1103/PhysRevLett.86.402.
- [33] ALICE Collaboration. *The ALICE experiment – A journey through QCD*. Nov. 2022. arXiv: 2211.04384 [nucl-ex].
- [34] R. Snellings. “Collective expansion at the LHC: selected ALICE anisotropic flow measurements”. In: *Journal of Physics G: Nuclear and Particle Physics* 41.12 (Nov. 2014), p. 124007. DOI: 10.1088/0954-3899/41/12/124007.

- [35] M. L. Miller et al. “Glauber Modeling in High-Energy Nuclear Collisions”. In: *Annual Review of Nuclear and Particle Science* 57.1 (May 2007), pp. 205–243. DOI: 10.1146/annurev.nucl.57.090506.123020.
- [36] R. J. Glauber. “Lectures on Theoretical Physics”. In: *Interscience* 1 (1959). Ed. by W. E. Brittin and L. C. Dunham, p. 315. DOI: 10.1016/j.nuclphysa.2017.05.072.
- [37] R. D. Woods and D. S. Saxon. “Diffuse Surface Optical Model for Nucleon-Nuclei Scattering”. In: *Phys. Rev.* 95 (July 1954), pp. 577–578. DOI: 10.1103/PhysRev.95.577.
- [38] J. S. Moreland, J. E. Bernhard, and S. A. Bass. “Alternative ansatz to wounded nucleon and binary collision scaling in high-energy nuclear collisions”. In: *Phys. Rev. C* 92.1 (July 2015), p. 011901. DOI: 10.1103/PhysRevC.92.011901.
- [39] P. Bożek and W. Broniowski. “Collective dynamics in high-energy proton-nucleus collisions”. In: *Physical Review C* 88.1 (July 2013). DOI: 10.1103/physrevc.88.014903.
- [40] D. d’Enterria et al. “Estimates of hadron azimuthal anisotropy from multiparton interactions in proton–proton collisions at  $\sqrt{s} = 14$  TeV”. In: *The European Physical Journal C* 66.1–2 (Jan. 2010), pp. 173–185. DOI: 10.1140/epjc/s10052-009-1232-7.
- [41] Y. Pandit. “Azimuthal Anisotropy in U+U Collisions at  $\sqrt{s_{NN}} = 193$  GeV with STAR Detector at RHIC”. In: *Journal of Physics: Conference Series* 458.1 (Aug. 2013), p. 012003. DOI: 10.1088/1742-6596/458/1/012003.
- [42] H. Song and U. Heinz. “Multiplicity scaling in ideal and viscous hydrodynamics”. In: *Physical Review C* 78.2 (Aug. 2008). DOI: 10.1103/physrevc.78.024902.
- [43] L. D. Landau and E. M. Lifshitz. *Fluid mechanics, by L.D. Landau and E.M. Lifshitz; translated from the Russian by J.B. Sykes and W.H. Reid*. Pergamon Press, 1959.
- [44] P. K. Kovtun, D. T. Son, and A. O. Starinets. “Viscosity in Strongly Interacting Quantum Field Theories from Black Hole Physics”. In: *Physical Review Letters* 94.11 (Mar. 2005). DOI: 10.1103/physrevlett.94.111601.
- [45] C. Eckart. “The Thermodynamics of Irreversible Processes. III. Relativistic Theory of the Simple Fluid”. In: *Phys. Rev.* 58 (Nov. 1940), pp. 919–924. DOI: 10.1103/PhysRev.58.919.

- [46] W. A. Hiscock and L. Lindblom. “Generic instabilities in first-order dissipative relativistic fluid theories”. In: *Phys. Rev. D* 31.4 (Feb. 1985), pp. 725–733. DOI: 10.1103/PhysRevD.31.725.
- [47] W. Israel and J.M. Stewart. “Transient relativistic thermodynamics and kinetic theory”. In: *Annals of Physics* 118.2 (Apr. 1979), pp. 341–372. DOI: 10.1016/0003-4916(79)90130-1.
- [48] I. Müller. “Zum Paradoxon der Wärmeleitungstheorie”. In: *Zeitschrift für Physik* 198.4 (Aug. 1967), pp. 329–344. DOI: 10.1007/BF01326412.
- [49] S. Floerchinger, E. Grossi, and J. Lion. “Fluid dynamics of heavy ion collisions with mode expansion”. In: *Physical Review C* 1 (July 2019). DOI: 10.1103/physrevc.100.014905.
- [50] S. Floerchinger and E. Grossi. “Causality of fluid dynamics for high-energy nuclear collisions”. In: *Journal of High Energy Physics* 186 (Aug. 2018). DOI: 10.1007/JHEP08(2018)186.
- [51] A. Bazavov et al. “Equation of state in (2+1)-flavor QCD”. In: *Physical Review D* 90.9 (Nov. 2014). DOI: 10.1103/physrevd.90.094503.
- [52] P. Alba et al. “Effect of the QCD equation of state and strange hadronic resonances on multiparticle correlations in heavy ion collisions”. In: *Physical Review C* 98.3 (Nov. 2018). DOI: 10.1103/physrevc.98.034909.
- [53] P. Garg et al. “Conserved number fluctuations in a hadron resonance gas model”. In: *Physics Letters B* 726.4 (Nov. 2013), pp. 691–696. DOI: 10.1016/j.physletb.2013.09.019.
- [54] A Andronic et al. “Statistical hadronization of charm in heavy-ion collisions at SPS, RHIC and LHC”. In: *Physics Letters B* 571.1–2 (Oct. 2003), pp. 36–44. DOI: 10.1016/j.physletb.2003.07.066.
- [55] J. Noronha-Hostler, J. Noronha, and C. Greiner. “Transport Coefficients of Hadronic Matter Near  $T_c$ ”. In: *Physical Review Letters* 103.17 (Oct. 2009). DOI: 10.1103/physrevlett.103.172302.
- [56] F. Cooper and G. Frye. “Single-particle distribution in the hydrodynamic and statistical thermodynamic models of multiparticle production”. In: *Phys. Rev. D* 10 (July 1974), pp. 186–189. DOI: 10.1103/PhysRevD.10.186.

- [57] D. Teaney. “Effect of shear viscosity on spectra, elliptic flow, and Hanbury Brown–Twiss radii”. In: *Phys. Rev. C* 68.3 (Sept. 2003), p. 034913. DOI: 10.1103/PhysRevC.68.034913.
- [58] J.-F. Paquet et al. “Production of photons in relativistic heavy-ion collisions”. In: *Phys. Rev. C* 93.4 (Apr. 2016), p. 044906. DOI: 10.1103/PhysRevC.93.044906.
- [59] D. Devetak et al. “Global fluid fits to identified particle transverse momentum spectra from heavy-ion collisions at the Large Hadron Collider”. In: *Journal of High Energy Physics* 2020.6 (June 2020). DOI: 10.1007/jhep06(2020)044.
- [60] A. Mazeliauskas et al. “Fast resonance decays in nuclear collisions”. In: *The European Physical Journal C* 79.3 (Mar. 2019). DOI: 10.1140/epjc/s10052-019-6791-7.
- [61] G. Torrieri et al. “SHARE: Statistical hadronization with resonances”. In: *Computer Physics Communications* 167.3 (May 2005), pp. 229–251. DOI: 10.1016/j.cpc.2005.01.004.
- [62] N. S. Amelin et al. “Fast hadron freeze-out generator”. In: *Physical Review C* 74.6 (Dec. 2006). DOI: 10.1103/PhysRevC.74.064901.
- [63] J. Sollfrank, P. Koch, and U. Heinz. “The influence of resonance decays on the  $p_T$  spectra from heavy-ion collisions”. In: *Physics Letters B* 252.2 (Dec. 1990), pp. 256–264. DOI: 10.1016/0370-2693(90)90870-C.
- [64] P. Braun-Munzinger. “Quarkonium production in ultra-relativistic nuclear collisions: suppression versus enhancement”. In: *Journal of Physics G: Nuclear and Particle Physics* 34.8 (July 2007), S471. DOI: 10.1088/0954-3899/34/8/S36.
- [65] D. Bödeker and M. Laine. “Heavy quark chemical equilibration rate as a transport coefficient”. In: *Journal of High Energy Physics* 2012.7 (July 2012). DOI: 10.1007/jhep07(2012)130.
- [66] S.P. Parker. *McGraw-Hill Encyclopedia of Physics*. McGraw-Hill, 1993.
- [67] B. Svetitsky. “Diffusion of charmed quarks in the quark-gluon plasma”. In: *Phys. Rev. D* 37.9 (May 1988), pp. 2484–2491. DOI: 10.1103/PhysRevD.37.2484.
- [68] M. Toda R. Kubo and N. Hashitsume. *Statistical Physics II*. Springer-Verlag, 1985. DOI: 10.1007/978-3-642-96701-6.

- [69] F. Capellino et al. “Fluid-dynamic approach to heavy-quark diffusion in the quark-gluon plasma”. In: *Phys. Rev. D* 106.3 (Aug. 2022), p. 034021. DOI: 10.1103/PhysRevD.106.034021.
- [70] N. G. van Kampen. *Stochastic Processes in Physics and Chemistry*. North Holland Publishing Company, Apr. 1983. DOI: 10.1002/bbpc.19830870424.
- [71] M. Cacciari, M. Greco, and P. Nason. “The  $p_T$  spectrum in heavy-flavour hadroproduction”. In: *Journal of High Energy Physics* 1998.05 (July 1998), p. 007. DOI: 10.1088/1126-6708/1998/05/007.
- [72] S. Acharya et al. “Transverse-momentum and event-shape dependence of D-meson flow harmonics in Pb–Pb collisions at ALICE”. In: *Physics Letters B* 813 (Feb. 2021), p. 136054. DOI: 10.1016/j.physletb.2020.136054.
- [73] R. Rapp and H. van Hees. *Heavy Quark Diffusion as a Probe of the Quark-Gluon Plasma*. 2008. arXiv: 0803.0901 [hep-ph].
- [74] G. S. Denicol et al. “Derivation of transient relativistic fluid dynamics from the Boltzmann equation”. In: *Physical Review D* 85.11 (June 2012). DOI: 10.1103/physrevd.85.114047.
- [75] F. Capellino et al. “Fluid dynamics of charm quarks in the quark-gluon plasma”. In: *Physical Review D* 108.11 (Dec. 2023). DOI: 10.1103/physrevd.108.116011.
- [76] L. Adamczyk et al. “Measurement of  $D^0$  Azimuthal Anisotropy at Midrapidity in Au+Au Collisions at  $\sqrt{s_{NN}} = 200$  GeV”. In: *Physical Review Letters* 118.21 (May 2017). DOI: 10.1103/physrevlett.118.212301.
- [77] L. Adamczyk et al. “Measurement of  $J/\psi$  Azimuthal Anisotropy in Au+Au Collisions at  $\sqrt{s_{NN}} = 200$  GeV”. In: *Physical Review Letters* 111.5 (Aug. 2013). DOI: 10.1103/physrevlett.111.052301.
- [78] A. Andronic et al. “Heavy quark(onium) at LHC: the statistical hadronization case”. In: *Journal of Physics G: Nuclear and Particle Physics* 37.9 (Aug. 2010), p. 094014. DOI: 10.1088/0954-3899/37/9/094014.
- [79] L. Vermunt et al. “Mapping properties of the quark gluon plasma in Pb-Pb and Xe-Xe collisions at energies available at the CERN Large Hadron Collider”. In: *Physical Review C* 108.6 (Dec. 2023). DOI: 10.1103/physrevc.108.064908.
- [80] A. Adare et al. “Transverse energy production and charged-particle multiplicity at midrapidity in various systems from  $\sqrt{s_{NN}} = 7.7$  to 200 GeV”. In: *Phys. Rev. C* 93.2 (Feb. 2016), p. 024901. DOI: 10.1103/PhysRevC.93.024901.

- [81] S. S. Adler et al. “Identified charged particle spectra and yields in Au+Au Collisions at  $\sqrt{s_{\text{NN}}} = 200$  GeV”. In: *Physical Review C* 69.3 (Mar. 2004). DOI: 10.1103/physrevc.69.034909.
- [82] M. Cacciari, S. Frixione, and P. Nason. “The  $p_{\text{T}}$  spectrum in heavy-flavour photoproduction”. In: *Journal of High Energy Physics* 2001.03 (Mar. 2001), pp. 006–006. DOI: 10.1088/1126-6708/2001/03/006.
- [83] J. D. Bjorken. “Highly relativistic nucleus-nucleus collisions: The central rapidity region”. In: *Phys. Rev. D* 27.1 (Jan. 1983), pp. 140–151. DOI: 10.1103/PhysRevD.27.140.
- [84] L. Altenkort et al. “Heavy quark momentum diffusion from the lattice using gradient flow”. In: *Physical Review D* 103.1 (Jan. 2021). DOI: 10.1103/physrevd.103.014511.
- [85] L. Altenkort et al. “Heavy Quark Diffusion from Flavor Lattice QCD with 320 MeV Pion Mass”. In: *Physical Review Letters* 130.23 (June 2023). DOI: 10.1103/physrevlett.130.231902.
- [86] S. Acharya et al. “Prompt  $D^0$ ,  $D^+$ , and  $D^{*+}$  production in Pb–Pb collisions at  $\sqrt{s_{\text{NN}}} = 5.02$  TeV”. In: *Journal of High Energy Physics* 2022.1 (Jan. 2022). DOI: 10.1007/jhep01(2022)174.
- [87] J. Adam et al. “Centrality and transverse momentum dependence of  $D^0$ -meson production at mid-rapidity in Au+Au collisions at  $\sqrt{s_{\text{NN}}} = 200$  GeV”. In: *Phys. Rev. C* 99.3 (2019), p. 034908. DOI: 10.1103/PhysRevC.99.034908.
- [88] J. Adam et al. “Observation of  $D_s^\pm/D^0$  enhancement in Au+Au collisions at  $\sqrt{s_{\text{NN}}} = 200$  GeV”. In: *Phys. Rev. Lett.* 127 (2021), p. 092301. DOI: 10.1103/PhysRevLett.127.092301.
- [89] L. Adamczyk et al. “Energy dependence of  $J/\psi$  production in Au+Au collisions at  $\sqrt{s_{\text{NN}}} = 39, 62.4$  and 200 GeV”. In: *Phys. Lett. B* 771 (2017), pp. 13–20. DOI: 10.1016/j.physletb.2017.04.078.
- [90] A. Andronic, P. Braun-Munzinger, and J. Stachel. “Hadron production in central nucleus–nucleus collisions at chemical freeze-out”. In: *Nuclear Physics A* 772.3–4 (June 2006), pp. 167–199. DOI: 10.1016/j.nuclphysa.2006.03.012.
- [91] A. Andronic et al. “The multiple-charm hierarchy in the statistical hadronization model”. In: *Journal of High Energy Physics* 2021.7 (July 2021). DOI: 10.1007/jhep07(2021)035.

- [92] M.I Gorenstein et al. “Statistical coalescence model with exact charm conservation”. In: *Physics Letters B* 509.3–4 (June 2001), pp. 277–282. DOI: 10.1016/S0370-2693(01)00516-0.
- [93] J. E. Bernhard. *Bayesian parameter estimation for relativistic heavy-ion collisions*. 2018. arXiv: 1804.06469 [nucl-th].
- [94] S. A. Bass et al. “Neural networks for impact parameter determination”. In: *Journal of Physics G: Nuclear and Particle Physics* 20.1 (Jan. 1994), p. L21. DOI: 10.1088/0954-3899/20/1/004.
- [95] L.G. Pang et al. “An equation-of-state-meter of quantum chromodynamics transition from deep learning”. In: *Nature Communication* 9.210 (Jan. 2018). DOI: 10.1038/s41467-017-02726-3.
- [96] Y. Song et al. “Determining the temperature in heavy-ion collisions with multiplicity distribution”. In: *Physics Letters B* 814 (2021), p. 136084. DOI: 10.1016/j.physletb.2021.136084.
- [97] F. Emmert-Streib et al. “An Introductory Review of Deep Learning for Prediction Models With Big Data”. In: *Frontiers in Artificial Intelligence* 3 (Feb. 2020), p. 4. DOI: 10.3389/frai.2020.00004.
- [98] V. Nair and G. Hinton. “Rectified Linear Units Improve Restricted Boltzmann Machines”. In: vol. 27. June 2010, pp. 807–814.
- [99] Boris Polyak. *Introduction to Optimization*. July 2020.
- [100] J. Gawlikowski et al. *A Survey of Uncertainty in Deep Neural Networks*. 2022. eprint: 2107.03342.
- [101] N. Metropolis et al. “Equation of State Calculations by Fast Computing Machines”. In: *Journal of Chemical Physics* 21.6 (1953), p. 1087. DOI: 10.1063/1.1699114.
- [102] T. Dong, D. An, and N. Kim. “Prognostics 102: Efficient Bayesian-Based Prognostics Algorithm in MATLAB”. In: Feb. 2019. DOI: 10.5772/intechopen.82781.
- [103] G. S. Denicol, S. Jeon, and C. Gale. “Transport coefficients of bulk viscous pressure in the 14-moment approximation”. In: *Phys. Rev. C* 90.2 (Aug. 2014), p. 024912. DOI: 10.1103/PhysRevC.90.024912.

- [104] J. E. Bernhard, J. S. Moreland, and S. A. Bass. “Bayesian estimation of the specific shear and bulk viscosity of quark-gluon plasma”. In: *Nature Physics* 15 (Nov. 2019), p. 024912. DOI: 10.1038/s41567-019-0611-8.
- [105] P. K. Kovtun, D. T. Son, and A. O. Starinets. “Viscosity in Strongly Interacting Quantum Field Theories from Black Hole Physics”. In: *Physical Review Letters* 94.11 (Mar. 2005). DOI: 10.1103/physrevlett.94.111601.
- [106] Y. Seemann. *Multidimensional parameter optimization in fluid dynamic simulations of heavy-ion collisions*. 2022.
- [107] K. Schwarz et al. “Grid Computing at GSI for ALICE and FAIR - present and future”. In: *Journal of Physics: Conference Series* 396.3 (Dec. 2012), p. 032097. DOI: 10.1088/1742-6596/396/3/032097.
- [108] J. Bezanson et al. *Julia: A Fast Dynamic Language for Technical Computing*. 2012. arXiv: 1209.5145 [cs.PL].
- [109] D. Foreman-Mackey et al. “emcee: The MCMC Hammer”. In: *Publications of the Astronomical Society of the Pacific* 125.925 (Mar. 2013), pp. 306–312. DOI: 10.1086/670067.
- [110] V. Begun and W. Florkowski. “Bose-Einstein condensation of pions in heavy-ion collisions at energies available at the CERN Large Hadron Collider”. In: *Physical Review C* 91.5 (May 2015). DOI: 10.1103/physrevc.91.054909.
- [111] P. Braun-Munzinger, K. Redlich, and J. Stachel. “Particle Production in Heavy-Ion Collision”. In: *Quark-Gluon Plasma 3*. WORLD SCIENTIFIC, Jan. 2004, pp. 491–599. DOI: 10.1142/9789812795533\_0008.
- [112] O. Barannikova. *Probing collision dynamics at RHIC*. 2004. arXiv: nucl-ex/0403014 [nucl-ex].
- [113] J. Chen et al. “Nonequilibrium kinetic freeze-out properties in relativistic heavy ion collisions from energies employed at the RHIC beam energy scan to those available at the LHC”. In: *Physical Review C* 104.3 (Sept. 2021). DOI: 10.1103/physrevc.104.034901.
- [114] C. Chattopadhyay, U. Heinz, and T. Schäfer. “Fluid dynamics from the Boltzmann equation using a maximum entropy distribution”. In: *Phys. Rev. C* 108 (Sept. 2023), p. 034907. DOI: 10.1103/PhysRevC.108.034907.